Frozen Gaussian Wavepacket to Perform and Correct Nonadiabatic Mixed Quantum- Classical Dynamics

Rafael Souza Mattos

NNT : 0000AIXM0000

THÈSE DE DOCTORAT

Soutenue à Aix-Marseille Université
le 24 octobre 2024 par

Rafael SOUZA MATTOS

Frozen Gaussian Wavepacket to Perform and Correct Nonadiabatic Mixed Quantum-Classical Dynamics

Discipline
Sciences chimiques

École doctorale
ED250 Sciences chimiques

Laboratoire/Partenaires de recherche
Institut de Chimie Radicalaire (UMR 7273)

Composition du jury

Daniel ESCUDERO KU Leuven	Rapporteur
Gerrit GROENHOF University of Jyväskylä	Rapporteur
Petr SLAVÍČEK University of Chemistry and Technology	Examinateur
Paola NAVA Aix-Marseille Université	Examinatrice
Loïc JOUBERT-DORIOL Université Gustave Eiffel	Examinateur
Denis JACQUEMIN Université de Nantes	Président du jury
Mario BARBATTI Aix-Marseille Université	Directeur de thèse

Affidavit

I, undersigned, Rafael SOUZA MATTOS, hereby declare that the work presented in this manuscript is my own work, carried out under the scientific supervision of Mario BARBATTI, in accordance with the principles of honesty, integrity and responsibility inherent to the research mission. The research work and the writing of this manuscript have been carried out in compliance with both the French national charter for Research Integrity and the Aix-Marseille University charter on the fight against plagiarism.

This work has not been submitted previously either in this country or in another country in the same or in a similar version to any other examination body.

Place Marseille, date 26 août 2024

List of publications and participation in conferences

1) Liste des publications et/ou brevet réalisées dans le cadre du projet de thèse :

    1. M. Pinheiro Jr, M. de O. Bispo, B. C. Garain, R. S. Mattos, M. T. do Casal, J. M. Toldo, S. Mukherjee, M. Barbatti, **ULaMDyn: Enhancing Excited-State Dynamics Analysis Through Streamlined Unsupervised Learning**, (2024). In preparation.
    2. S. Mukherjee, Y. Lassmann, R. S. Mattos, B. Demoulin, B. F. E. Curchod, M. Barbatti, **Assessing Nonadiabatic Dynamics Methods in Long Timescales**, (2024). In preparation.
    3. R. S. Mattos, S. Mukherjee, M. Barbatti, **Legion: a Platform for Mixed Quantum-Classical Nonadiabatic Dynamics**, (2024). In preparation.
    4. R. S. Mattos, S. Mukherjee, M. Barbatti, **Quantum Dynamics from Classical Trajectories**, J. Chem. Theory Comput. (accepted, 2024). DOI: 10.1021/acs.jctc.4c00783
    5. A. Tomaz, R. S. Mattos, M. Barbatti, **Gravitationally-induced Wave Function Collapse Time for Molecules**, Phys. Chem. Chem. Phys. **26**, 20785 (2024). DOI: 10.1039/D4CP02364A
    6. S. Mukherjee, R. S. Mattos, J. M. Toldo, H. Lischka, M. Barbatti, **Prediction Challenge: Simulating Rydberg photoexcited cyclobutanone with surface hopping dynamics based on different electronic structure methods**, J. Chem. Phys. **160**, 154306 (2024). DOI: 10.1063/5.0203636
    7. J. M. Toldo, R. S. Mattos, M. Pinheiro, Jr., S. Mukherjee, M. Barbatti, **Recommendations for Velocity Adjustment in Surface Hopping**, J. Chem. Theory Comput. **20**, 614 (2024). DOI: 10.1021/acs.jctc.3c01159

2) Participation aux conférences et écoles d'été au cours de la période de thèse :
    1. **Quantum Dynamics from Classical Trajectories**. R. S. Mattos, S. Mukherjee, M. Barbatti. LatinXChem. 14th – 15th October. (Virtual Conference, poster presentation)
    2. **Quantum Dynamics from Classical Trajectories**. R. S. Mattos, S. Mukherjee, M. Barbatti. 17th International Congress of Quantum Chemistry. 26th June – 1st July, 2023. Bratislava, Slovakia. (Conference, poster presentation)
    3. International summer School in electronic structure Theory: electron correlation in Physics and Chemistry (ISTPC). Aussois, France. 2022. (School)

Résumé

Les méthodes de dynamique nonadiabatique jouent un rôle crucial dans l'étude de la réaction des systèmes moléculaires lorsqu'ils sont excités par des photons et soumis à une nouvelle surface d'énergie potentielle électronique. La topographie de l'état excité peut être explorée pour proposer des réactions chimiques facilitées par la photoexcitation, étudier la stabilité moléculaire et les processus de récupération d'énergie, entre autres. À ce jour, de nombreuses nouvelles méthodes pour la dynamique nonadiabatique et les calculs de structure électronique qui y sont associés sont toujours en cours de développement afin d'améliorer la précision, de réduire les coûts de calcul et d'étendre le domaine d'application. Malgré leur succès, ces méthodes utilisent souvent des approximations qui peuvent conduire à des résultats erronés, parfois difficiles à détecter. Dans ce cas, on peut généralement se référer à des résultats expérimentaux pour valider le modèle utilisé pour représenter le système. Il est également possible d'effectuer plusieurs séries de dynamiques avec différentes méthodes pour détecter une tendance et des valeurs aberrantes, mais cela entraînerait des coûts de calcul élevés. Pour relever le défi de réaliser des simulations abordables et de haute qualité tout en gardant une trace de leurs imprécisions occasionnelles, nous avons développé un programme de recherche qui s'articule autour de deux thèmes principaux. Le premier a abouti à un programme informatique appelé Legion, une plateforme destinée à faciliter le développement de nouvelles méthodes pour la dynamique nonadiabatique et à modifier les méthodes existantes. Le programme est construit en Python afin que le code puisse être facilement étendu, et il est déjà interfacé avec plusieurs méthodes et logiciels de structure électronique couramment utilisés. Nous testons le programme avec des molécules réelles et l'utilisons pour compléter la discussion sur la dynamique du fulvène et sa dépendance vis-à-vis des conditions initiales. La deuxième branche de recherche a abouti à QDCT, une nouvelle stratégie de post-traitement des résultats des sauts de surface pour obtenir des résultats de la dynamique des paquets d'ondes, comme dans le cas du frayage multiple. Elle utilise des trajectoires classiques pour propager le paquet d'ondes nucléaires. La méthode est indifférente aux approximations ad hoc présentes dans le saut de surface et peut être utilisée pour évaluer les systèmes problématiques. La méthode est testée par rapport à des modèles analytiques et les approximations nécessaires pour travailler dans des systèmes multidimensionnels sont présentées. Legion et QDCT sont tous deux intégrés dans la plateforme Newton-X et sont disponibles gratuitement.

Mots clés: nonadiabatic dynamics, *ab initio* multiple spawning, trajectory surface hopping, computational chemistry

Abstract

Nonadiabatic dynamics methods play a crucial role in investigating the reaction of molecular systems to being excited by photons and submitted to a new electronic potential energy surface. The topography of the excited state can be explored to propose chemical reactions facilitated by photoexcitation, study the molecular stability, and energy harvesting processes, among other purposes. To this day, many new methods for nonadiabatic dynamics and the electronic structure calculations associated with them are still being developed to improve accuracy, reduce computational costs, and expand the application domain. Despite their success, those methods often use approximations that may lead to wrong results, which can be hard to detect. In those cases, one can usually refer to experimental results to validate the model used to represent the system. Alternatively, one can perform multiple sets of dynamics with different methods to detect a trend and outliers, but this would have extended computational costs. To address those challenges of performing affordable, high-quality simulations while still keeping track of their occasional inaccuracies, we developed a research program branched into two main topics. The first one resulted in a computer program named Legion, a platform to facilitate the development of new methods for nonadiabatic dynamics and modify existing ones. It is built in Python so that the code can be easily expanded, and it is already interfaced with multiple commonly used electronic structure methods and software. We test the program with real molecules and use it to complement the discussion of fulvene dynamics and its dependence on initial conditions. The second research branch resulted in QDCT, a novel strategy for post-processing surface hopping results to obtain wavepacket dynamics results, as in multiple spawning. It uses classical trajectories to propagate the nuclear wavepacket. The method is indifferent to ad hoc approximations present in surface hopping and can be used to assess problematic systems. The method is tested against analytical models, and approximations necessary to work in multi-dimensional systems are presented. Both Legion and QDCT are integrated into the Newton-X platform and are freely available.

Keywords: nonadiabatic dynamics, *ab initio* multiple spawning, trajectory surface hopping, computational chemistry

Acknowledgments

Thanks to the European Research Council for the financial resources, the Centre de Calcul Intensif d'Aix-Marseille for the computational resources, and the Light and Molecules group for the PhD opportunity.

To Professor Mario Barbatti, for the opportunity to work in the group and on this project. Mario is not only a very pleasant person to deal with, but his practical thinking and vast knowledge are also a reference for both research and writing. I am also deeply grateful for the participation of Saikat Mukherjee in my PhD. Your multiple insights were also fundamental for the development of this thesis. You always cared that we understood what we were doing, not only me but also the other students. I thank you both for your patience with my shortcomings; this work wouldn't be possible without you.

Coming to Marseille, I met fantastic people. Max and Diana have been there for me since my first day in the city. I treasure our friendship and questionable humor. Josene, who welcomed me to the city, you will be sorely missed both in our office and the Friday beer. Dario, you were here for only a year, but you are so extremely likable that it feels like I have known you for a long time. Baptiste, who is an example of professional conduct a skilful programmer. I also thank the members of the Light and Molecules group, for your company and participation in making it such a pleasant environment. Elizete, Silmar, Ritam, Bidhan with his pressing questions, Matheus, Juliana, Mariana, Eduarda, and Anderson.

I thank my friends I have been carrying for a long time. Mariana is a very accomplished researcher, but I admire you much beyond that. It is always a pleasure to have the chance to talk with you, even if we do this almost on a daily basis. It is no exaggeration to say that I would not be here without your guiding hand. Karol, who at first can look all serious but has a very easy laugh. I respect how much of a responsible person you are and how you always take care of your friends. Mayk, who has been putting up with me since the very first day at the university. It is rare to see someone who enjoys their work as much as you do. From the people I know, you pass the coolest vibes.

And I thank my friends I have been carrying for the longest time. Larissa and Marcelle, It's going to be fifteen years now. Half of our lives. We are probably as weird now as we were back then, but hopefully not much more. And that's probably the secret spice. We are each in a different country now, but the world is not big enough to separate us. Despite our frequent conversations, I long for the times we get to be in the same place to drink some coffee. I also welcome our "new" pal, Alex, who has quite literally saved our sorry dwarven asses multiple times.

I would like to thank my mother, Beatriz, the most consistent name in my list of acknowledgments over the years. Of all the people who helped me along the way, none of it would be possible without the first spark. You though me that the most important thing, the one that no one can take from you, is your knowledge.

Lastly and most importantly, I thank Larissa, my wife, who once again agreed to accompany me on this journey. We were not sure what we signed up for when we changed countries and decided to live alone, but we did it anyway. There is no one else I would have chosen to share a roof or a life with. You are always so caring and careful. You teach me to be more gentle and kind—within a limit, let's not exaggerate here. We are geographically distant now, and I miss working by your side, because you look so very cute when you are very focused in your activity. But you are always here with me. Yet again, we don't know what the future may hold, but I am more sure now than I was at the beginning of this journey that you will be there for me, and I will be there for you.

Table of Contents

Affidavit 2
List of publications and participation in conferences 3
Résumé 4
Abstract 5
Acknowledgments 6
Table of Contents 8
Table of Abbreviations 10
Introduction 11
1. Nonadiabatic dynamics 15
1.1. Nonadiabatic quantum dynamics 16
1.2. Nonadiabatic mixed quantum-classical dynamics 17
2. Background Theory 19
2.1. Surface Hopping 19
2.2. Multiple Spawning 21
2.2.1. Full Multiple Spawning 21
2.2.2. *Ab Initio* Multiple Spawning 22
2.2.3. BAT approximation 26
2.3. Time derivative coupling 26
2.3.1. Time-dependent Baeck-An coupling 27
3. Quantum Dynamics from Classical Trajectories 29
3.1. Trajectory Basis Functions control 32
3.2. Trajectory substitution 33
3.3. Interpolated trajectories 34
3.4. Method's workflow 38
3.5. Computational details 40
3.6. Application 43
3.6.1. Unidimensional systems 43
3.6.2. Multidimensional system 46
3.7. Conclusion 48
4. Legion 50
4.1. Legion in a Nutshell 50
4.2. Legion in Depth 53
4.2.1. Modified BAT approximation 53
4.2.2. Adaptive timestep 54
4.2.3. Electronic structure interfaces 55
4.2.4. Input and output 56

4.3. Computational details 56
4.4. Application 57
4.4.1. Fulvene 58
4.4.2. DMABN 64
4.5. Conclusion 66
5. Extra contributions 67
5.1. Recommendations for velocity adjustment in surface hopping 67
5.2. Prediction challenge: Cyclobutanone dynamics with different electronic structure methods 69
5.3. Long time scale dynamics 71
5.4. Gravitationally-induced wave function collapse 72
5.5. Unsupervised Learning of Molecular Dynamics 73
Conclusions 75
Bibliography 77
ANNEXES 93
A. Equations-of-motion of the nuclear coefficients 93
B. BAT vs. SPA approximations 97
C. Analytical Models 100
a. Tully 1: Simple avoided crossing 100
b. Tully 2: Dual avoided crossing 100
c. Tully 3: Extended coupling with reflection 100
d. Spin-Boson Hamiltonian 101
D. Confidence Interval Study 103
E. Overlap vs. Dimensionality 106

Table of Abbreviations

AIMS	*Ab Initio* Multiple Spawning
BAT	Bra-ket Average Taylor
BATE	Bra-ket Average Taylor/Exponential
CASPT2	Second-Order Complete Active Space Perturbation Theory
CASSCF	Complete Active Space Self-Consistent Field
DC-FSSH	Decoherence-Corrected Fewest Switches Surface Hopping
DD-vMCG	Direct Dynamics Variational Multi-Configurational Gaussian
ESSAIMS	Energy Stochastic Selection *Ab-Initio* Multiple Spawning
FMS	Full Multiple Spawning
FOMO-CI	Floating Occupation Molecular Orbitals Configuration Interaction
FSSH	Fewest Switches Surface Hopping
IFGA	Independent First Generation Approximation
MCSCF	Multi-Configuration Self Consistent Field
MCTDH	Multi-Configuration Time Dependent Hartree
ML-MCTDH	Multilayer Multi-Configuration Time Dependent Hartree
MRCI	Multireference Configuration Interaction
NAC	Nonadiabatic Coupling
NACV	Nonadiabatic Coupling Vector
NA-MQC	Nonadiabatic Mixed Quantum-Classical
NEA	Nuclear Ensemble Approach
PES	Potential Energy Surface
QDCT	Quantum Dynamics from Classical Trajectories
RASSCF	Restricted Active Space Self-Consistent Field
RMSD	Root Mean Squared Displacement
SH	Surface Hopping
SPA	Saddle Point Approximation
TBF	Trajectory Basis Function
TDBA	Time Derivative Baeck-An
TDC	Time Derivative Coupling
TDDFT	Time-Dependent Density Functional Theory
TDSE	Time-Dependent Schrödinger Equation
TISE	Time Independent Schrödinger Equation
TSH	Trajectory Surface Hopping
vMCG	Variational Multi-Configurational Gaussian
XMS-CASPT2	Extended Multi-State Second-Order Complete Active Space Perturbation Theory

Introduction

The field of photochemistry studies the interaction of photons and molecules. Upon absorbing light, a molecule changes to an electronically excited state. The behavior of the system in this excited condition can be considerably different from that of the same system in the ground, which is the least energetic state. The potential energy experienced by the system varies significantly based on the level of excitation. This can facilitate reactions that, in the ground state, would be slowed down or prohibited by high energy barriers. For example, molecular photo-switches[1] and photochemical dissociations[2] are some of them to name. Alternatively, fast relaxation without any chemical reaction can also be an essential aspect to study, such as the stability of the DNA[3,4] or applications like photovoltaics.[5,6]

Computer simulations of these phenomena are essential to unravel the mechanisms of photoreaction and relaxation, and multiple methods with different levels of approximation are commonly used. Those methods can be classified into time-independent ones,[7] usually focused on analyzing the topography of potential energy surfaces, and dynamical ones,[8] which monitor the time evolution of the system. Depending on the system being studied and the phenomenon one intends to investigate, the theoretically rigorous methods can become computationally unfeasible, limiting the options to more approximated ones. But this comes at the cost of losing part of the effects that would happen in a real system, lessening the reliability of the results. To address this problem, in this thesis, I present QDCT, a method to assess the quality of surface hopping dynamics using Gaussian wavepacket propagation and possibly correct the results. During the development of QDCT, I noticed a lack of easily accessible and efficient multiple spawning software. To address this problem, I created Legion, a platform written to use and develop methods of Gaussian wavepacket propagation. The program already comes interfaced with a large variety of electronic structure methods. It contains multiple strategies to improve the efficiency of the code. This thesis explains the implementation of those two codes and shows how they can be applied to study molecular systems.

Some of the earliest and most important systems of interest in photochemistry are the nucleobases, the building blocks that form the DNA.[9] Those molecules present high photostability; after absorbing a photon, they decay quickly to the ground state and back to their original conformation.[10–12] This stability is important in preserving the structure of DNA. It has been suggested that it is one of the selection factors in the evolutionary choice for the canonical nucleobases in DNA.[13,14] When this structure is not preserved, it can lead to health problems, possibly cancer.[15] A particular subfield of photochemistry, nonadiabatic dynamics, is very important in investigating the deactivation pathways of the nucleobases.[16–21] Those deactivation

pathways tell us what geometries the system will assume as it moves from the initial conformation at the moment of excitation until it is relaxed and stable again. The comprehension of those natural systems can be used to develop modified nucleobases,[22–26] which can have medical applications,[27,28] or even propose and study new lifeforms, as in xenobiology.[29,30]

The contrary can also be found: systems that undergo a conformational change when exposed to light, and their function depends on that. A typical example is the retinal. In its relaxed state, it remains in a *cis* conformation, but when photoexcited, it rapidly switches to a *trans* geometry and initiates a chain of reactions between proteins and neurons that ultimately end up in the brain, the process of vision.[31–33] This effect has recently been investigated more in the field of molecular photoswitches, where a system can be switched between two isomers controled by light.[34] Light has been gaining traction since it is not naturally part of many systems, so it will not interfere with them and can be precisely controlled spatially, in time and wavelength.[35]

The study of photochemistry and nonadiabatic dynamics requires coordination between experiment and theory. Theoretical calculations are cheaper than experiments, so they can be used to explore the chemical space and help guide experiments. They also allow us to inspect the system closely; we can follow the electronic character over time, the conformations the system can assume, the ratio between those conformations, and many other properties. The models used for computer simulations are easier to control, and different effects can be isolated to measure their impact on the phenomena of interest. Conversely, the experiments also serve as a guide for the theory, validating which models could be used for the simulations and verifying the calculations. An example of such a collaboration was the Boostcrop project, a consortium of multiple researchers from experimental and theoretical groups aiming to design molecular heaters to increase crop production under cold conditions.[36] Their work investigated molecules from the barbituric group, known for being good light absorbers in the UV-A region,[37] in their capability to release the absorbed energy as heat. A product of those molecules could then be applied to crops to increase their average temperature, mitigating the adverse effects caused by extreme cold conditions. This would allow harvesting at a prolonged time of the year and in geographic regions otherwise unsuitable for cultivation. The computational investigation, experimental synthesis, spectra, and toxicological analysis led to a candidate molecule to be used as such a product.[36]

However, the theoretical work should not be seen simply as a stepping stone to filter out unuseful molecules to reduce the number of experiments. It can also be used to understand and question the experiments. In Ref[38], De Camillit *et al.* measured the lifetime of the excited state of the four nucleobases and their respective nucleosides (nucleobase plus sugar). The experiments were performed using a pump-probe ionization scheme. They concluded that the

lifetime for adenosine (0.57 ps), the nucleoside, in the gas phase is about half the time for adenine (1.1 ps). Later simulations[39] noticed that the dominant conformation responsible for the decay involves a ring puckering that should not be affected by the presence of the sugar. They also noticed that the ionization potential changes for adenosine as it goes towards the crossing between states, going beyond the experimental setup. The experimentally measured lifetime was shorter than expected, not because the molecule had decayed but because the molecule left the probe detection window.

While computational methods are continuously being developed aiming to simulate larger systems to obtain more precise results, they are not failure-proof. A recent prediction challenge was released, in which a future experiment was announced, and theoretical groups were invited to predict the measurements (Section 5.2). The experiment would measure the deactivation of cyclobutanone excited to a Rydberg state, the second singlet excited state, to be precise. Multiple groups contributed,[40–54] totaling 15 works using a vast combination of nonadiabatic dynamics methods and electronic structure methods. The experimental result has still not been released at the time of writing. Still, the wide range of results obtained by the different methods points to a lack of self-evaluation from the purely theoretical works. There is general knowledge that indicates which methods should be better for describing a given system, but even the golden standard for nonadiabatic dynamics, MCTDH, returns different lifetimes depending on the simulation.[40,41,55] Without a ground on experimental results, we lack ways to assess the quality of the computer simulations.

This series of examples proves the usefulness of theoretical work in helping to understand molecular systems and their interaction with light. It also shows the importance of flexibility in selecting the appropriate electronic structure approach when performing dynamics, which is the major factor in controlling the quality of the simulation.[56] If one specific method is known to describe the system better, having it available for propagation would be desirable. The case of the cyclobutanone prediction challenge[51] also reminds us that we are still dealing with models that may not describe real systems well. In this thesis, I present my work attempting to address those topics.

After going through the theoretical background, I present quantum dynamics from classical trajectories (QDCT) in Chapter 3. , a novel strategy to obtain Gaussian nuclear dynamics by post-processing the output of a trajectory surface hopping (TSH) simulation. QDCT does not require any new electronic structure calculations. Because of that, it comes at almost no extra cost when compared to the dynamics. The method is implemented in a program that has been tested in analytical multidimensional systems (model Hamiltonians) and shows the potential to become a tool to assess the quality of dynamics from a theoretical basis. It contains interfaces to read the trajectories from the Newton-X NS format and Ulamdyn (Figure 1).

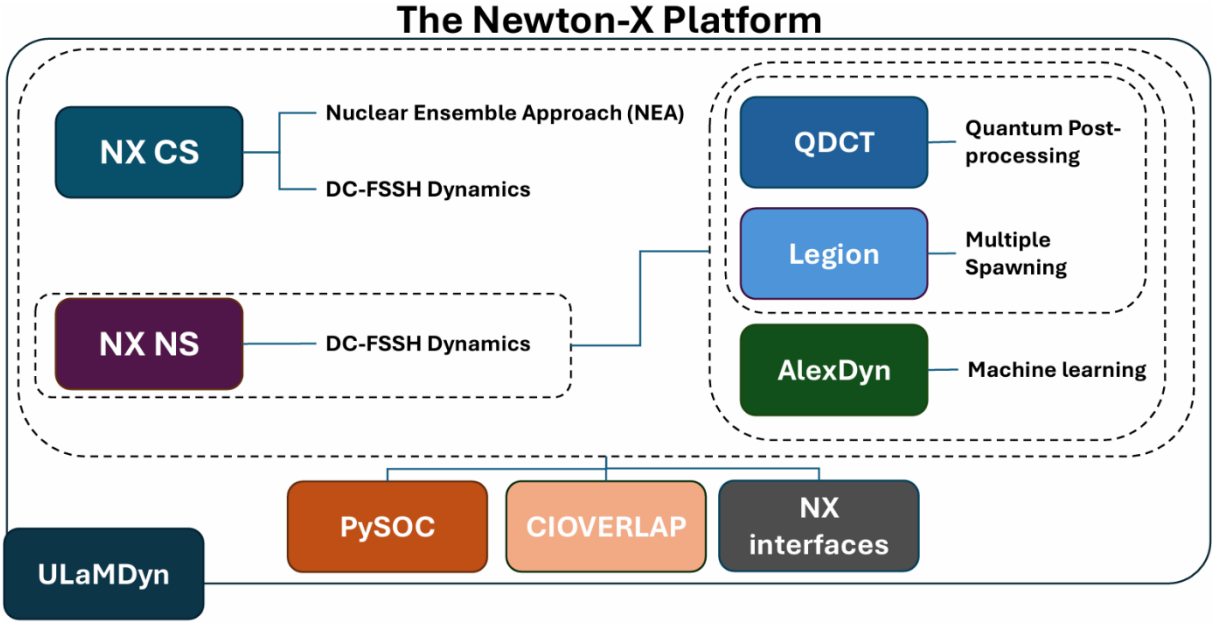

Figure 1 Schematic description of the programs contained within the Newton-X platform. QDCT and Legion, developed in this thesis, are shown on the right side.

The Newton-X package is used for surface hopping dynamics. The code has a long history[57,58] and is interfaced with multiple electronic structure software. The original program, Newton-X classical series (CS), contained the code for the initial condition generation, dynamics propagation, and analysis. In the last five years, the code was reimplemented from scratch in Fortran, with a focus on efficiency and data management, foreseeing applications in long timescale dynamics.[59] Associated with the development of this new series (NS), functions were divided into different modules. The module responsible for initial conditions is still available in Newton-X CS and can be used to generate the initial conditions for Legion as well. Newton-X NS focuses on trajectory propagation and hopping, while the data curation is in charge of Ulamdyn, a new software developed in the group with automated analysis methods. The output of Legion is compatible with Newton-X NS, and Ulamdyn will be extended in the near future also to perform the analysis of Legion's AIMS simulations.

In Chapter 4. I present Legion, a software I designed and created to allow for flexibility in developing nonadiabatic dynamics methods. This software is produced under the umbrella of the Newton-X package and, consequently, inherits all the electronic structure interfaces available in Newton-X. The first nonadiabatic dynamics method I implemented in Legion is *ab initio* multiple spawning (AIMS).[60] To use all those electronic structure methods, Legion also makes use of known approximations and introduces new ones that allow for efficient propagation and circumvents the need to compute the nonadiabatic coupling vector, which is not available for all electronic structures.

I finalize in Chapter 5. with my contribution to papers that do not originate from this thesis but relate to it in some topics.

1. Nonadiabatic dynamics

After a photon excites a molecule, its electronic state is not an eigenvector of the Hamiltonian. This triggers the time evolution of the system until it is re-equilibrated, and energy is released in this process.[61] There are multiple mechanisms for the equilibration, and they are usually summarised in the Jablonski diagram[62] (Figure 2). The process can be classified into radiative, where a photon is absorbed or emitted during the transition, and non-radiative, where no photon emission occurs.

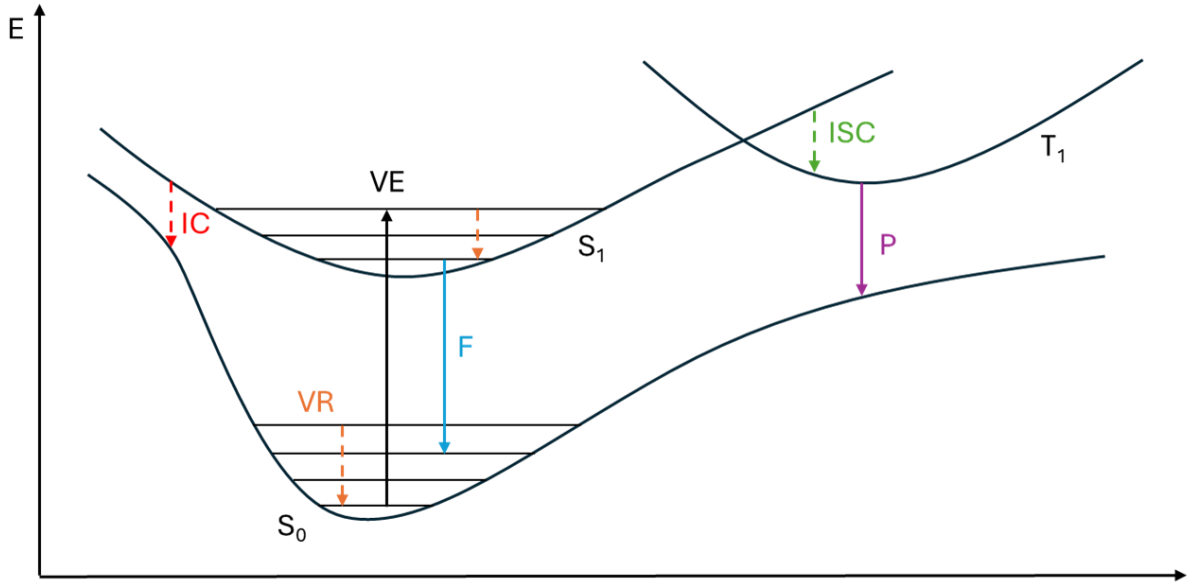

Figure 2 Jablonski diagram. Radiative transitions in solid arrows. VE: Vertical excitation; IC: internal conversion; ISC: intersystem crossing; P: phosphorecence; F: fluorescence; VR: vibrational relaxation.

A molecule in its most relaxed state should be found close to the minimum of the ground state (S_0).[63] When the molecule absorbs a photon, it gains energy that allows it to jump to one of the excited states (S_1 in the figure), a vertical excitation. The system moves on the new potential energy surface (PES), which has its own local minima and can be much different from the ground state PES. The new topography can allow new reactions, while an energy barrier in the ground state would otherwise prevent that. Beyond electronic excitation, the absorbed energy can also cause vibrational excitation. This extra energy is dissipated internally, among the vibrational levels, or to the surrounding molecules in the process of vibrational relaxation.[64]

The system can undergo a transition to a lower-energy electronic state through internal conversion between states with the same spin multiplicity.[65] When the energy surfaces do not favor internal conversion, the system might remain excited long enough to eliminate the extra

energy as a photon and fluoresce back to the ground state. A non-radiative process similar to internal conversion can happen between states of different multiplicities if the system goes from a single to a triplet (T_1) state, an intersystem crossing.[66,67] Those are mediated by the spin-orbit coupling between the spin and orbital angular momenta, but generally, it is a slower process. Once in the triplet state, the system can eventually decay back to the ground state while emitting a photon during phosphorescence.[68,69]

The dynamics methods treated in this thesis focus mainly on ultrafast dynamics, those that happen from a couple hundred femtoseconds to a few picoseconds. This is primarily due to a restrain in computational power to propagate dynamics for dozens or hundreds of thousands of steps.[70] An essential aspect of the ultrafast process is the presence of crossing seams and crossing points.[71] Those unique geometries are characterized by the break of the Born-Oppenheimer approximation, where the nonadiabatic coupling (NAC) is non-negligible and different electronic states are degenerated.[72]

Nonadiabatic dynamics follows the system's behavior and help to understand which processes contribute most to the deactivation.[73] Multiple families of methods with varying degrees of approximation are used to study those systems. They generally propagate the system in time following the time-dependent Schrödinger equation (TDSE) or some analogous.[74–76] They allow us to track how much of the system can be found in each electronic state and the associated nuclear behavior.

1.1. Nonadiabatic quantum dynamics

In molecular quantum dynamics, nuclei and electrons are treated at the same level of theory when solving the TDSE. Multiconfiguration time-dependent Hartree (MCTDH)[77,78] is likely the most known method for performing molecular quantum dynamics. In this method, the potential energy surface is precomputed to build a model system that represents the molecule under study, containing both vibrational and electronic levels. The multiconfigurational wavefunction is expanded as a linear combination of Hartree products of single-particle functions.[77] The equations of motion for the expansion coefficients and the single-particle functions are obtained from the time-dependent variational principle, ensuring that the method will return the optimal solution with the given basis. As is typical for multiconfigurational methods, the number of configurations scales exponentially with the number of elements in the basis, and so does the computational cost to propagate them.[79] On the other hand, since the variational principle propagates the coefficients, the method is expected to converge to the numerically exact result as the number of configurations increases.[80]

To alleviate the scaling problem, some variations of MCTDH have been developed.[81] In particular, a later formulation was introduced in which the single-particle functions could also be expressed as time-dependent multiconfigurational expansions. This can be done recursively,

adding one layer to each level of the single-particle function represented as an expansion. This derived method is named multilayer MCTDH (ML-MCTDH).[82,83] It effectively moves the scaling from a single combinatory problem of many degrees of freedom to multiple smaller spaces. While conventional MCTDH is viable up to dozens of degrees of freedom, ML-MCTDH can treat a few hundred.[83]

Still within the class of quantum dynamics, direct dynamics variational multi-configuration Gaussian (DD-vMCG)[84–87] is a popular method for quantum direct dynamics.[88] In direct dynamics methods, instead of fitting the potential energy surface prior to propagation, they are computed only when necessary. The system evolves following trajectories, with well-defined geometries that can be used to perform single-point calculations with any electronic structure method. In DD-vMCG, those trajectories are used to build the nuclear wavepacket as a linear combination of Gaussian functions.[89] The force guiding the trajectories is obtained variationally, and they are all coupled with each other. The Gaussian functions of the basis are said to follow "quantum trajectories".[85]

1.2. Nonadiabatic mixed quantum-classical dynamics

In an attempt to obtain more straightforward methods and software, nonadiabatic mixed quantum-classical methods[90] (NA-MQC) were developed, such as trajectory surface hopping[91,92] and Ehrenfest[93–95] families of methods. In NA-MQC, the nuclear degrees of freedom and the electronic ones are treated at different levels of theory. They consider nuclei moving as classical trajectories propagated over the electronic surfaces. At the same time, the electrons are treated quantum mechanically by solving the time-independent Schrödinger equation (TISE). They are responsible for the forces used to propagate the nuclei. The classical trajectories usually move independently from one another, and the swarm of trajectories can recover the nuclear wavepacket in the classical limit.[96,97] While those usually show good agreement with higher-level methods, they use multiple approximations and, eventually, some *ad hoc* ones.[98–100]

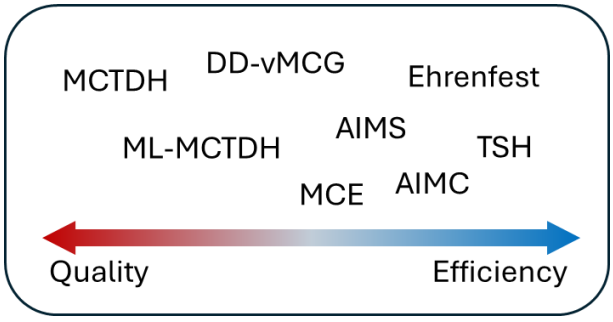

Figure 3 Placement of some nonadiabatic dynamics methods in the balance accuracy vs computational efficiency.

Between the high accuracy of quantum dynamics and the computational efficiency of independent trajectories is the family of Gaussian wavepacket propagation methods (Figure 3). Those also use the classically propagated trajectories, which are then used to construct nuclear wavepackets that are evolved following the TDSE. Heller introduced the idea of propagating a quantum wavepacket built from a linear combination of frozen Gaussians[89] that follows the classical trajectories. An advantage that the Gaussian wavepacket methods have in comparison to other NA-MQC methods is that, in principle, the quality of the result can be improved until convergence by increasing the number of classical trajectories. One family of such methods, which will be one of the foci of this thesis, is the multiple spawning.[101] It optimizes the balance of quality and computational efficiency by automatically expanding the nuclear basis during the propagation in the regions where extra trajectories are needed the most.

Another method that uses a Gaussian wavepacket is the multi-configurational Ehrenfest (MCE)[94,102,103] dynamics. In it, the trajectories that guide the nuclear wavepacket are propagated over an effective potential energy surface, as in Ehrenfest dynamics. The propagation over the effective potential can lead to less separation between trajectories compared to when they are following different electronic states.[102] A combination of the automatic control of the number of functions in the basis, as in multiple spawning, and propagation of the Gaussian functions over Ehrenfest trajectories gives rise to the *ab initio* multiple cloning (AIMC)[104,105] method.

This is not an exhaustive list of all methods used for nonadiabatic dynamics, but it does show the flexibility of the Gaussian wavepacket.[106,107] The equations of motion for those methods can be simple, depending primarily on how one chooses to propagate the trajectories. Those trajectories can be propagated at different levels of theory, such as quantum trajectories, classical ones, or following an effective potential.[60,86,102] The nuclear basis can have a constant number of functions or can be expanded along propagation.[60,104,108] The different combinations of the choice to treat the wavepacket give rise to multiple dynamics methods.

2. Background Theory

2.1. Surface Hopping

Surface hopping is among the most popular families of NA-MQC methods in the literature. In this approach, the nuclear wavefunction is represented by a swarm of classical particles following a single Born-Oppenheimer PES, propagated independently from one another. At each point, the trajectory can hop between electronic surfaces and transfer the population between them. We focus here on the Fewest Switches Surface Hopping (FSSH)[91] variant, where this probability of switching between states is computed as a function of time to minimize the number of hopping while still describing the correct population transfer. A scheme illustrating the multiple trajectories and the hopping process is presented in Figure 4.

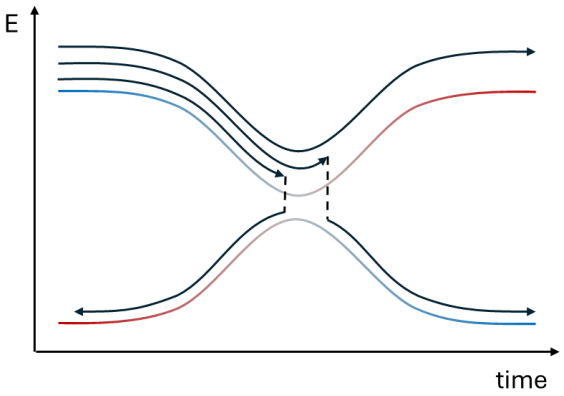

Figure 4 Scheme of the FSSH method. Classical trajectories follow the Born-Oppenheimer PES with a chance to hop between states.

The nuclei of those trajectories are propagated classically, following Newton's equation of motion, and without interaction with the other trajectories in the swarm. The time-dependent electronic wave function is expanded on the time-independent adiabatic electronic states computed at the classical nuclear geometry. The expansion coefficients are propagated according to the TDSE:

$$\begin{aligned} \dot{c}_j &= -\sum_k c_k \left(\frac{i}{\hbar} H_{JK} + \sigma_{JK} \right), \\ H_{JK} &= \langle \phi_J \,|\, \hat{H}_e \,|\, \phi_K \rangle_{\mathbf{r}}, \\ \sigma_{JK} &= \left\langle \phi_J \left| \frac{\partial \phi_K}{\partial t} \right. \right\rangle_{\mathbf{r}} = \mathbf{d}_{JK} \cdot \mathbf{v}, \end{aligned} \tag{1}$$

where $\hat{H}_e$ is the electronic Hamiltonian operator and ϕ are the electronic eigenfunctions, $\boldsymbol{v}$ is the classical velocity of the molecule, and $\mathbf{d}_{JK} = \langle \phi_J \,|\, \nabla_{\mathbf{R}} \,|\, \phi_K \rangle_{\mathbf{r}}$ is the nonadiabatic coupling vector (NACV) between states *J* and *K*. The index $\boldsymbol{r}$ indicates integration over the electronic coordinates. σ_{JK} is the time derivative coupling (TDC) that can be computed directly from the nonadiabatic coupling or using other methods discussed in Section 2.3.

The information required to propagate the coefficients is obtained by single-point calculations computed at the classical coordinates of the nuclei at each timestep, which also provides the gradient of the current electronic state used in Newton's equation. To account for the transition between states, at each timestep, the hopping probability function is evaluated:

$$P_{I->J} = \max\left[0, \frac{2\Delta t}{\rho_{II}}\left(\hbar^{-1}\,\mathrm{Im}(\rho_{JI}H_{JI}) - \mathrm{Re}(\rho_{JI})\mathbf{d}_{JI}\cdot\mathbf{v}\right)\right]. \qquad (2)$$

Within the adiabatic representation, Δt is the size of the timestep. The electronic Hamiltonian $H_{JI} = E_I\delta_{IJ}$ depends on the adiabatic potential energy E_I of state *I* since the electronic states are orthogonal. For a single trajectory, the reduced density matrix elements are:

$$\rho_{IJ} = c_I c_J^{*}. \qquad (3)$$

In a more general case, the off-diagonal terms of the reduced density matrix, the coherences, should also contain the overlap of the environment states,[109] which decreases with time, causing natural decoherence. In the case of an isolated molecular system, the environment is the nuclear wavepacket. This overlap will always be one for a single trajectory, which makes the surface hopping trajectories suffer from an overcoherence problem.[110] Multiple methods attempt to correct the decoherence effect lacking from FSSH while still in the context of independent trajectories,[100,111,112] but they are all *ad hoc* corrections.

A uniform random number is drawn together with the computation of the probability defined in Eq.(2), and compared to it, the relation between them will dictate whether or not a hop will occur. The stochastic process associated with the hopping probability describes the population transfer along the dynamics. The hop between surfaces is also associated with a correction in the momentum of the molecule to conserve the total energy.[113]

The independent trajectories make the method practical from the technical point of view since each trajectory runs individually from a set of initial conditions. The number of processors required is kept constant throughout the simulation and is stipulated by the electronic structure method. Trajectories can also be submitted at different times and on multiple computers and then copied to the same place for analysis. Unfortunately, this convenience is associated with the limitations of the method. Surface hopping considers the linear combination of the

electronic states to treat the nonadiabatic effects. However, the nuclear part of the wavefunction is represented by a single element that does not interact with any other nuclear function.

Despite the limitations, decoherence-corrected FSSH (DC-FSSH) has shown its reliability. Compared to other methods in benchmarks, it usually agrees with more expensive and less approximated methods.[98,114,115]

2.2. Multiple Spawning

2.2.1. Full Multiple Spawning

Another prominent approach to simulating nonadiabatic dynamics are the multiple spawning methods: Full Multiple Spawning (FMS)[116] and *Ab Initio* Multiple Spawning (AIMS).[60,117] These methods present some significant differences compared to surface hopping, particularly in treating the nuclear degrees of freedom and the non-stochastic nature of the propagation.

FMS also uses classical trajectories to propagate the dynamics. However, after the classical propagation, they are blended into a linear combination to approximate the nuclear wavepacket. This wavepacket is propagated quantum mechanically over the basis of classical trajectories. It is said to recover the exact nonrelativistic solution within the limit of an infinite nuclear basis.[118]

The automatic update of the number of trajectory basis functions (TBFs), the classical trajectories, can control the balance between the method's accuracy and computational cost.[119,120] The population transfer between states is intermediated by a transfer between the coefficients of trajectories on different states and happens in regions with high nonadiabatic coupling. To allow for this interaction, the basis is expanded at the coupling region by spawning (adding) a new trajectory, which is at the core of the method (Figure 5).[116] Each trajectory being propagated is monitored, and when they enter the coupling region, a new trajectory is created on the other electronic state with which the initial trajectory is coupled. This child trajectory is a copy of the parent when it reaches the maximum coupling value, and similar to FSSH, it has a momentum correction to keep the total energy of parent and child the same. The child is then added to the basis and is propagated on that new state.

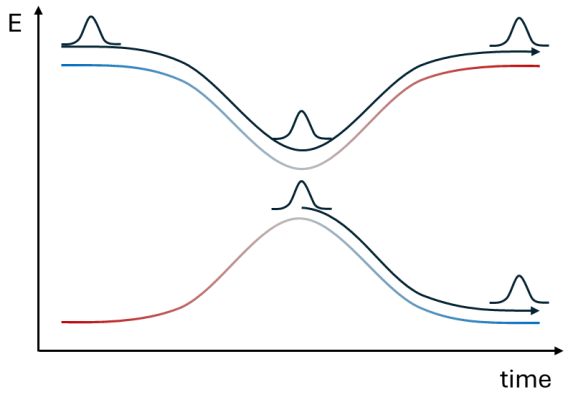

Figure 5 Scheme of the multiple spawning method. Classical trajectories follow the Born-Oppenheimer PES, and new trajectories are added in regions with high coupling between states.

For the propagation of the amplitudes, one uses a set of frozen Gaussians built around the classical trajectories discussed in the following section. It is possible to notice how this leads to a different treatment of the decoherence phenomena, lacking in FSSH, which is naturally accounted for by the interaction between trajectories.

One potential problem due to the automatic expansion of the TBF is that the number of trajectories being propagated increases exponentially. This can be a limiting factor, especially for longer time scales. This is accompanied by the increased computational effort to perform the simulation since each classical trajectory requires electronic structure calculations at each timestep of propagation. Different methods exist to mitigate the cost, either by removing the unpopulated TBFs, which have a negligible influence on the dynamics, from the entire set,[121] or by stochastically selecting a branch of trajectories to follow.[119]

2.2.2. *Ab Initio* Multiple Spawning

AIMS differentiates itself from FMS by employing two main approximations: the saddle-point approximation (SPA)[118] and the independent first-generation approximation (IFGA).[60,122] For the former, the matrix elements of the Hamiltonian associated with the potential energy and nonadiabatic coupling are integrals over the entire nuclear space, which is impractical for molecular applications. Instead, using the SPA, one relies on the localized nature of the Gaussian functions to compute the potential energies and couplings at the centroid position between each pair of trajectories. For the latter approximation, it is expected that for systems with higher dimensionality, the trajectories rapidly move away from each other, and the overlap between them decreases quickly, making the trajectories independent. In IFGA, instead of starting the simulation from a set of initial conditions, multiple simulations are performed starting from a single initial condition each.[122]

In his seminal work on semiclassical approximation,[89] Heller proposed using a collection of frozen Gaussians to represent the nuclear wavepacket. Each Gaussian is built as a distribution

centered at the position (R_i) and momenta (P_i) of a particle following a classical trajectory. The resulting wavepacket is a linear combination that can be written as

$$\Omega_J(\mathbf{R},t) = \sum_j^{N_J} C_j^J(t)\chi_j^J(\mathbf{R}),$$
$$\chi_j^J(\mathbf{R}) = \prod_{\rho=1}^{3N}\left(\frac{2\omega_\rho}{\pi}\right)^{1/4} exp[-\omega_\rho(R_\rho - \bar{R}_{j\rho}^J(t))^2 + i\bar{P}_{j\rho}^J(t)(R_\rho - \bar{R}_{j\rho}^J(t)) + i\gamma_j(t)]. \quad (4)$$

The index *j* counts the trajectories associated with an electronic state *J*. The index ρ runs over all nuclear coordinates, *N* is the number of atoms in the system, and N_J is the number of Gaussians associated with state *J*. During the propagation, the widths (ω_ρ) are specific for each atom type and are kept constant,[123] characterizing them as frozen Gaussians. The phase factor γ_j is specific for each trajectory. This combines the advantage of approximating the quantum wavepacket with the simplicity of using classical equations to propagate the trajectories.

To obtain the total wavefunction, one can use the Born-Huang expansion,[124] where for each electronic state, there is a linear combination of Gaussian functions representing the nuclear wavepacket associated with that electronic state, as in

$$\Psi(\mathbf{r},\mathbf{R},t) = \sum_J^\infty \Omega_J(\mathbf{R},t)\phi_J(\mathbf{r};\mathbf{R}). \quad (5)$$

The electronic functions ($\phi_J(\mathbf{r};\mathbf{R})$) are the eigenfunctions of the electronic TISE for each electronic state *J*. While the trajectories are propagated using a classical equation of motion, the coefficients associated with each of them can be optimally propagated using the TDSE. Where each electronic state *J* has its own set of trajectories *j*. Each trajectory is propagated classically, independent from the others, but the coefficients *C* connect them. When the Born-Huang wavefunction[124] in Eq. (5) is inserted into the TDSE:

$$i\frac{\partial\Psi(\mathbf{r},\mathbf{R},t))}{\partial t} = \hat{H}(\mathbf{r},\mathbf{R})\Psi(\mathbf{r},\mathbf{R},t), \quad (6)$$

we obtain the equation of motion for the nuclear coefficients. The detailed development can be found in Annex A. The resulting equation for the time derivative of the coefficients in the matrix notation is

$$\dot{\mathbf{C}} = -iS^{-1}(T - \tau + V - i\dot{S})\cdot\mathbf{C}, \quad (7)$$

where

$$
\begin{aligned}
S_{ij} &= \langle \chi_i^I \mid \chi_j^J \rangle_{\mathbf{R}} \delta_{IJ} \\
\dot{S}_{ij} &= \langle \chi_i^I \mid \dot{\chi}_j^J \rangle_{\mathbf{R}} \delta_{IJ} \\
T_{ij} &= \langle \chi_i^I \mid \hat{T}_n \mid \chi_j^J \rangle_{\mathbf{r},\mathbf{R}} \delta_{IJ} \\
V_{ij} &= \left\langle \chi_i^I \phi_I \left| \hat{H}_{el} \right| \chi_j^J \phi_J \right\rangle_{\mathbf{r},\mathbf{R}} \\
\tau_{ij} &= \frac{1}{M} \langle \chi_i^I \mid \mathbf{d}_{IJ} \cdot \nabla_{\mathbf{R}} \mid \chi_j^J \rangle_{\mathbf{R}}
\end{aligned}
\tag{8}
$$

The matrix S contains information on the overlap between different Gaussians, $\dot{S}$ contains the products of one Gaussian with the time derivative of another, T contains the nuclear kinetic energy, V is the potential energy and τ_{ij} has information on the nonadiabatic coupling, which connects trajectories in different electronic states using $\boldsymbol{d}_{IJ}$. The index $\boldsymbol{r}$ denotes integration over the electronic coordinates, while the index $\boldsymbol{R}$ denotes integration over the nuclear coordinates.

Other than the trajectory coefficients, the phase factors also depend on time. The phase is independent of the coordinates and is associated with each trajectory, making it redundant with the coefficient.[125,126] This grants freedom of choice for the equation of motion for the phase, which can be used to improve the stability of the coefficient integration. Here, we choose the phase propagation[127]

$$
\dot{\gamma}_i = \sum_{\rho}^{3N} \frac{P_{i\rho}^2 - \omega_\rho}{2M_\rho} - E_i \tag{9}
$$

so that the nuclear coefficient remains constant unless it exchanges population with another trajectory. This means that the diagonal elements of the resulting matrix multiply the coefficients on the right side of Eq. (7) are zero, and the amplitude variation is only due to population transfer between trajectories.

The automatic control of the TBFs employs a combination of trajectory spawning and elimination, following pre-defined criteria. To deal with nonadiabatic effects, the most critical region to describe is where there are strong nonadiabatic couplings. Multiple spawning algorithms follow each classical trajectory, checking the norm of the nonadiabatic coupling ($\boldsymbol{d}_{ij}$) or the dot product of velocity with the coupling ($\boldsymbol{v}\cdot\boldsymbol{d}_{ij}$), i.e., the scalar time-derivative coupling (TDC). Once the trajectory being monitored reaches a threshold that defines the beginning of the coupling region, this trajectory is propagated independently from the rest of the system until it reaches the maximum coupling value. At this point, a child trajectory is created in the corresponding electronic state, retaining positions, energies, gradients, and coupling of the parent but adjusting the velocity to conserve the total energy between parent and child. This adjustment can follow the same relation used in FSSH:[128]

$$
v_\alpha^{(J)} = v_\alpha^{(L)} + \gamma_{LJ} \frac{u_\alpha}{M_\alpha}. \tag{10}
$$

The child trajectory is added to the nuclear basis and backpropagated to the origin of the coupling region. From that point, when the coefficients are propagated, the new trajectory allows population transfer between states. Along a single simulation, the system should enter multiple coupling regions. As the number of trajectories increases, more will pass through new coupling regions and cause new spawns. This exponential increase in the number of TBFs can become a computational problem due to the cost of running multiple electronic structure calculations for each timestep.

An optional strategy to alleviate the increase of the nuclear basis is trajectory elimination, where various factors can be checked to decide whether a trajectory is still important for propagation. First, one checks whether the trajectories are coupled through the Hamiltonian in the same sense as in Energy Stochastic Selection AIMS (ESSAIMS).[119] This considers both direct and indirect coupling and one trajectory can only be considered for elimination if it is entirely uncoupled from all others. The second checks whether the trajectory significantly overlaps with any other. If the absolute value of the overlap of the trajectory being checked with all others is smaller than a given threshold, then it can be considered for elimination. Lastly, the nuclear population of that trajectory can be computed as:

$$p_i = c_i^* \sum_j^{Ntraj} \langle \chi_i^I \mid \chi_j^J \rangle_R c_j \ . \tag{11}$$

If the nuclear population is below a given threshold, then it is another approval for elimination. A TBF should only be removed from the basis if it passes all those checks for elimination repeatedly for a given amount of time. When the TBF is removed from the basis, the nuclear wavepacket is projected into the new reduced basis to adjust the coefficients:

$$\sum_i^{Ntraj} \langle \chi_j^{(n)} \mid \chi_i^{(n)} \rangle_R c_i^{(n)} = \sum_k^{Ntraj} \langle \chi_j^{(n)} \mid \chi_k^{(o)} \rangle_R c_k^{(o)}. \tag{12}$$

The new coefficients $c_i^{(n)}$ are obtained by solving the projection of the molecular wavefunction before elimination, $\{c_k^{(o)}, \chi_k^{(o)}\}$, into the new basis $\chi_j^{(n)}$.

During the propagation or afterward, the expectation value of any arbitrary operator ($\hat{O}$) can be computed for each independent simulation by the relation:[101]

$$\begin{aligned} O(t) &= \frac{\left\langle \Psi(t) \middle| \hat{O} \middle| \Psi(t) \right\rangle_{R,r}}{\left\langle \Psi(t) \middle| \Psi(t) \right\rangle_{R,r}} \\ &= \sum_{JI}^{N_{state}} \sum_{ji}^{N_J(t) N_I(t)} (c_j^J(t))^* c_i^I(t) \left\langle \phi_J \chi_j^J(t) \middle| \hat{O} \middle| \phi_I \chi_i^I(t) \right\rangle_{R,r} \end{aligned} \tag{13}$$

Under the IFGA, the total property computed with AIMS is obtained by performing a simple average of the expectation values for each simulation starting from independent initial

conditions. So the expectation value is computed as in Eq. (13) for all trajectories derived from a single initial condition, but the cross term in between different initial conditions are neglected.

2.2.3. BAT approximation

Another source of computational time is the extra electronic structure calculations that have to be performed at the centroid between pairs of trajectories. In principle, the integrals presented for the potential energy (V_{ij}) and the nonadiabatic (τ_{ij}) terms from Eq. (7) run over the whole position space. The SPA[118] allows AIMS to be used in on-the-fly dynamics, approximating the integrals by the evaluation of the Gaussian, using the energies and nonadiabatic coupling at the centroid between trajectories, as in the relation:

$$\langle \chi_i^I \mid f(\mathbf{R}) \mid \chi_j^J \rangle \approx \langle \chi_i^I \mid \chi_j^J \rangle f(\bar{\mathbf{R}}). \tag{14}$$

From here on, we are omitting the integral indexes **R** and **r**; all integrals are assumed to be over the nuclear position unless otherwise specified.

The first step to alleviate the computational effort is to perform the single-point calculation only when the centroid values are necessary. Since all matrix elements depend on the overlap, there is no need to perform electronic structure calculations when this overlap is small enough.

Furthermore, one can opt to use the bra-ket averaged Taylor expansion[104] (BAT) to approximate those integrals without calculating the values at the centroid points. For potential energy, where the energy gradients are also available, the first-order Taylor expansion expressed in Eq. (15) can be used, which already considers that the potential energy term is only nonzero when both trajectories evaluated are in the same electronic state.

$$V_{ij} \approx \frac{V_I(\bar{\mathbf{R}}_i)+V_I(\bar{\mathbf{R}}_j)}{2} S_{ij} + \frac{\langle \chi_i \mid \mathbf{R}-\bar{\mathbf{R}}_j \mid \chi_j \rangle \nabla_{\mathbf{R}} V_I(\bar{\mathbf{R}}_j) + \langle \chi_i \mid \mathbf{R}-\bar{\mathbf{R}}_i \mid \chi_j \rangle \nabla_{\mathbf{R}} V_I(\bar{\mathbf{R}}_i)}{2}. \tag{15}$$

Similarly, we can use the zeroth-order Taylor expansion to approximate the nonadiabatic matrix element:

$$\tau_{ij} \approx \frac{\mathbf{d}_{IJ}(\bar{R}_i)+\mathbf{d}_{IJ}(\bar{R}_j)}{2M} \langle \chi_i^J \mid \frac{\partial}{\partial \mathbf{R}} \mid \chi_j^J \rangle. \tag{16}$$

The BAT approximation has shown promising results[104] while significantly reducing the amount of necessary electronic structure computations.

2.3. Time derivative coupling

The requirement to use nonadiabatic coupling can be a limiting factor for nonadiabatic dynamics propagation. Various electronic structure methods can compute energy and gradients, but coupling vectors are not always available due to fundamental restrictions or implementation difficulties.[129–131] Computing time-derivative coupling without nonadiabatic coupling is a

common practice in surface-hopping methods[132,133] and has been proposed and used for multiple spawning.[126,134,135]

In surface hopping, the propagation of the coefficients (Eq. (1)) depends directly on the TDC, and no modification is required. In multiple spawning, the working equations need to be altered, but this is straightforward. It arrives from a simple application of the chain rule in the formula for the nonadiabatic (τ_{ij}) terms. In the context of the SPA approximation, they can be computed with Eq. (17) evaluated at the centroid:

$$\begin{aligned}\tau_{ij} &\approx \mathbf{d}_{IJ} \cdot \frac{\langle \chi_i^I \,|\, \nabla \,|\, \chi_j^J \rangle_{\mathbf{R}}}{M}, \\ &\approx \frac{i}{\hbar} \mathbf{d}_{IJ} \cdot \mathbf{v}_c = \left\langle \phi_I \left| \frac{\partial \phi_J}{\partial t} \right\rangle = \frac{i}{\hbar} \sigma_{IJ,c}.\end{aligned} \tag{17}$$

Meanwhile, the BAT approximation can be written as Eq. (18), evaluated at both trajectories:

$$\tau_{ij} \approx \frac{i}{2\hbar} (\sigma_{IJ,i} + \sigma_{IJ,j}) S_{ij} \,. \tag{18}$$

For the evaluation of the time derivative coupling (σ_{IJ}), a method commonly used in surface hopping is based on the work of Hammes-Schiffer and Tully,[136] which uses the overlap of the electronic wavefunctions at sequenced time steps:

$$\sigma_{IJ} \,|_{t_0+\Delta t/2} \approx \frac{1}{2\Delta t} \Big[\big\langle \phi_I(t_0) \big| \phi_J(t_0+\Delta t) \big\rangle - \big\langle \phi_I(t_0+\Delta t) \big| \phi_J(t_0) \big\rangle \Big]. \tag{19}$$

Alternatively, a newer proposition that uses a unitary formalism shows potentially improved stability[134] but also depends on the overlap between electronic wavefunctions:

$$\sigma_{IJ} \,|_{t_0+\Delta t/2} \approx \frac{\int_{t_0}^{t_0+\Delta t} \big\langle \phi_I(t_0) \big| U^\dagger(\tau) \frac{\partial}{\partial \tau} U(\tau) \big| \phi_J(t_0) \big\rangle \, d\tau}{\Delta t} \,. \tag{20}$$

2.3.1. Time-dependent Baeck-An coupling

An alternative that circumvents the computation of the electronic overlaps entirely and has been gaining traction in surface hopping is the Baeck-An coupling,[137] proposed for dynamics separately by do Casal *et al.*[138] and Shu *et al.*[139]. In this, the time derivative Baeck-An (TDBA) coupling is approximated by the relation:

$$\sigma_{IJ} \approx \begin{cases} \dfrac{\mathrm{sgn}(\Delta E_{IJ})}{2} \sqrt{\dfrac{1}{\Delta E_{IJ}} \dfrac{d^2 \Delta E_{IJ}}{dt^2}} & if \ \dfrac{1}{\Delta E_{IJ}} \dfrac{d^2 \Delta E_{IJ}}{dt^2} > 0 \\ 0 & if \ \dfrac{1}{\Delta E_{IJ}} \dfrac{d^2 \Delta E_{IJ}}{dt^2} \leq 0 \end{cases} \tag{21}$$

while the second-order central difference can approximate the energy derivative:

$$\frac{d^2\Delta E_{IJ}(t)}{dt^2} \approx \frac{1}{\Delta t^2}\left[\Delta E_{IJ}(t-\Delta t) - 2\Delta E_{IJ}(t) + \Delta E_{IJ}(t+\Delta t)\right]. \quad (22)$$

This method has shown good agreement with dynamics using the nonadiabatic coupling in surface hopping.[51,128]

3. Quantum Dynamics from Classical Trajectories

The content of this chapter gave origin to the following publication:

R. S. Mattos, S. Mukherjee, M. Barbatti, **Quantum Dynamics from Classical Trajectories**, J. Chem. Theory Comput. (accepted, 2024). DOI: 10.1021/acs.jctc.4c00783.

The main code can be downloaded from https://gitlab.com/rafaelcpii93/qdct.git

---

In this chapter, we present Quantum Dynamics from Classical Trajectories (QDCT), a post-processing strategy to assess or improve the quality of a surface hopping simulation compared to a multiple spawning simulation at virtually no additional costs. QDCT leans on the strengths of each method. From surface hopping, we import the trajectories, which are expected to map the most important regions of the phase space. Since they are run independently, the computational cost is predictable. From multiple spawning, we import the heuristics to manage the trajectories, which are dressed by frozen Gaussians[89] and associated with a coefficient propagated using the TDSE that mediates the interaction between trajectories. In surface hopping, the properties are obtained as a simple average of all trajectories. With QDCT, the trajectories can be reweighted with the TDSE coefficients (Figure 6), and the properties can be computed similarly to conventional multiple spawning.

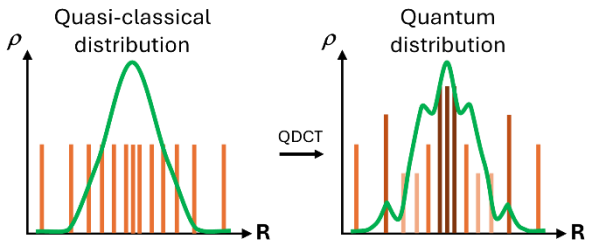

Figure 6 Conceptualization of the QDCT treatment. It can be interpreted as reweighting the pre-computed classical trajectories with the coefficients propagated using the TDSE.

Although in this first QDCT implementation, we have exclusively taken multiple spawning as the target level, this is not a restriction of the method's general idea. Any approach that uses Gaussian functions as a basis to propagate the TDSE can be replicated with QDCT. Thus, one could develop an alternative algorithm to the one presented here to propagate the widths as in DD-vMCG,[85,88] following the same principle of using pre-computed trajectories as the basis.

Looking at the equations of motion of the trajectories in multiple spawning, it can be realized that each trajectory is not dependent on the rest of the nuclear basis. This implies that they do not need to be propagated simultaneously. Other than the fact that the spawned trajectories will only appear when the parents reach a specific point in time, the trajectories are independent. With the trajectories computed, the coefficients can be integrated. This opens the way for new approaches, like using pre-computed trajectories from surface hopping and only propagating the coefficients.

The trajectories generated by surface hopping have some distinctions compared to those generated by conventional multiple spawning. The most obvious one is that the AIMS trajectories remain in the same state throughout their existence. In contrast, the FSSH trajectories will eventually change state due to the hoppings, occasionally multiple times in a single trajectory. This distinction creates a problem of discontinuities of trajectories that must be addressed if one intends to use them for coefficient propagation. The other and more subtle distinction is that the spawned trajectories are created at the ideal point in space and time to maximize the overlap between trajectories, favoring their communication and allowing the TDSE to control the population transition. The FSSH trajectories are not subjected to this constraint, creating an increasingly impeditive problem for computing the overlap as the dimension of the system increases.

On the other hand, using pre-computed trajectories means that the electronic structure calculations do not need to be repeated, so one obtains an approximation of a multiple spawning calculation at the cost of computing an analytical model since obtaining the electronic energies and gradients has the price of a simple memory lookup. It is also easier to control the computational cost of running multiple independent trajectories since the cost of each trajectory is easy to predict. The proposition is not a method to replace AIMS calculations but a correction to existing surface hopping dynamics that can work as a guide to assess the quality of the original calculation. Other methods employ the exploration of classical trajectories.[140] However, in those cases, the trajectories exist in the function of the coefficient propagation and the simulation only makes sense in combination with the coefficients. In QDCT, the pre-computed trajectories are a valid dynamic by themselves. The difference between the results before and after QDCT can point to potential shortcomings of surface hopping, while the similarity between them can increase confidence in the result at almost no extra cost.

The classical trajectories are used similarly to a conventional AIMS simulation. They are dressed with frozen Gaussians to create the nuclear wavepacket, and use the same equations of motion for the coefficients presented in Section 2.2. The condition for the increase in the number of trajectories being considered is also the same spawning condition mentioned in the same Section 2.2. A threshold for the nonadiabatic coupling is established to define the coupling

region. At the maximum point for this coupling value, a new trajectory is added to the nuclear basis, forming this relation between parent and child trajectories.

In our case, instead of creating a new trajectory during spawning, one of the available surface hopping trajectories is selected and added to the active nuclear basis (Section 3.2). This addition may be assisted by interpolated trajectories (Section 3.3), which use data from the pre-computed trajectories to approximate the ideal child trajectory (Figure 7).

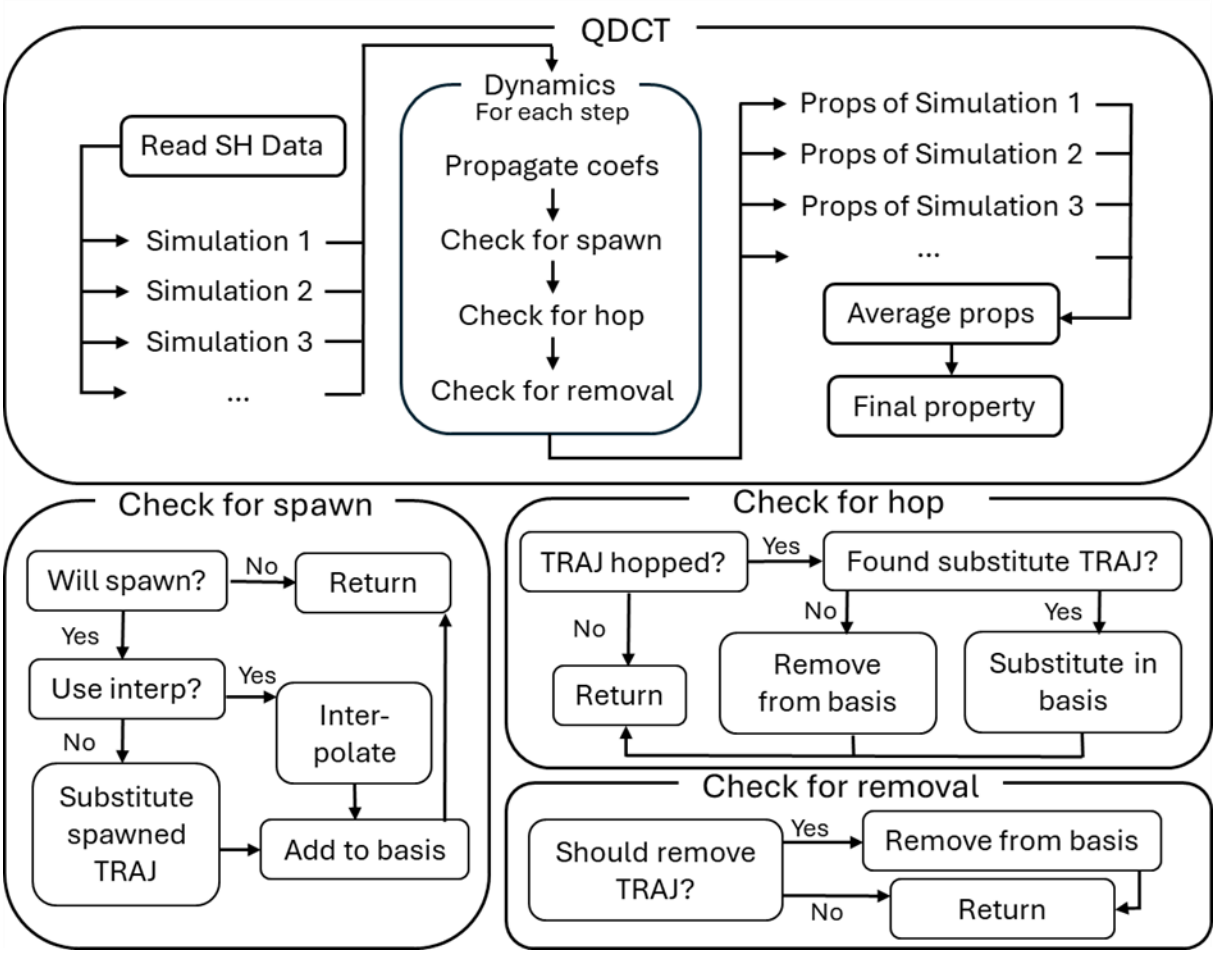

Figure 7 Flowchart of the most critical steps in QDCT. It reads the pre-computed trajectories and starts a new simulation for each trajectory. The available pre-computed trajectories can be added or removed from the active nuclear basis during the simulation.

Next, we discuss the strategies to circumvent the problems that arise when using surface hopping trajectories to propagate AIMS equations. To deal with the discontinuities caused by hoppings, we perform trajectory substitutions. When computing the overlap between parent and child trajectories, we create a pair of interpolated trajectories that approximate the spawning and lead to a smooth population transfer. We detail how the spawnings and trajectory elimination are treated and summarize how those ideas can be combined into a single workflow that allows QDCT to correct surface-hopping results.

3.1. Trajectory Basis Functions control

Similar to the spawning procedure, QDCT can control the number of trajectories in the nuclear basis by adding extra pre-computed trajectories in regions of high coupling. The norm of the nonadiabatic coupling vector or its product with the velocity can be monitored for each TBF until it reaches a predefined threshold. At this point, the rest of the simulation is put on hold, and the algorithm follows the trajectory until the maximum coupling value. At this time, a child trajectory is created, keeping the same geometry of the system and, consequently, the same gradients, energies, and nonadiabatic coupling. The nuclear momentum is adjusted to conserve total energy, as in Section 2.2.2.

In conventional AIMS, one would backpropagate the child trajectory to the current simulation time and return the rest of the simulation to its regular run. Here, we are not propagating the classical trajectories, so instead of this backpropagation, we perform a trajectory substitution to increase the number of trajectories in the basis. The details of how this substitution happens will be discussed in Section 3.2. Still, the idea is to find the one most similar to the trajectory being substituted in the list of surface hopping trajectories. In this case, the new trajectory would fill in the role of the child being added to the nuclear basis, already considering the corrected momenta when performing the substitution. Instead of backpropagating, we add the new trajectory to the nuclear basis at the beginning of the coupling region and continue coefficient propagation. The surface hopping trajectory may change state between the beginning of the coupling region and the maximum coupling time. This is considered when choosing a trajectory to perform the substitution. In this case, the trajectory will be added to the nuclear basis as soon as it enters the correct state. When the trajectory is added to the simulation, its phase and coefficients are zero.

Trajectory elimination can occur for a couple of reasons, including intentionally reducing the basis size. The usual elimination performed in AIMS can remove trajectories that are not coupled with the rest of the TBFs and do not contribute to the population. In QDCT, this elimination can also happen in case of a failed substitution, when the TBF being followed needs to be replaced, but no other is found suitable to fill its role.

In the first case, when the removal is performed on purpose, it follows the same criteria of Section 2.2.2, where the algorithm checks: if the trajectory evaluated for removal is coupled with any other through the Hamiltonian;[119] it checks whether the trajectories significantly overlap with any other TBF; it checks if the nuclear population of that trajectory is below a given threshold. If the trajectory has been marked for elimination for a defined number of timesteps, it is removed from the nuclear basis.

On the other hand, if a failed substitution causes the elimination, one can decide at the beginning of the algorithm whether to attempt to continue the simulation and perform the

removal or whether the run should be stopped altogether. A compromise between the two alternatives could be to evaluate the population of the trajectory being removed and how it would affect the norm of the wavefunction to decide on performing the elimination or stopping the simulation.

When the trajectory is removed from the nuclear basis, the nuclear wavepacket is projected into the new reduced basis (Eq. (12)). After this, there is another normalization step to ensure that each electronic state conserves the population through the elimination process and a second normalization to ensure that the total norm before and after the elimination is the same. The norm after this step is not set to unity but is conserved from whatever the value it was before the trajectory removal. If the trajectory is being removed on purpose, this renormalization step is redundant, but when the removal is imposed due to failed substitution, the projection in Eq. (12) may not go so well, meaning that the nuclear wavefunction after elimination is different from the wavefunction before the elimination. In this case, the difference between the wavefunction norm before and after the removal can also be used as a criterion to decide whether to continue the simulation.

3.2. Trajectory substitution

As mentioned in Section 3.1, trajectory substitution can be applied at spawning to add the child trajectory to the simulation. Given the nature of the surface hopping trajectories, this procedure can also be necessary after the original trajectory has hopped and changed state. In the ideal case, we expect the trajectory to follow a specific state; when there is a hop, this is not the case, and it is necessary to replace this TBF with another one in the correct electronic state.

Once the trajectory that needs to be substituted has been identified, one needs only their position and momentum. The algorithm can then go through all other surface hopping trajectories in the correct state and compare the overlap between them and the one being replaced. Initially, it can attempt to compare trajectories at the same simulation time, considering that the swarm of trajectories is expected to move with the nuclear wave packet. However, this can also be extended by looking at extra steps around the current time. This can be seen as inexpensively increasing the number of TBFs, in a slightly similar philosophy as in the "trains" of trajectories.[127,141] Then, one finds the highest overlap among all trajectories within the time window chosen (Figure 8). When comparing the overlaps, one can define a minimum value worth considering and ignore trajectories that overlap below this threshold.

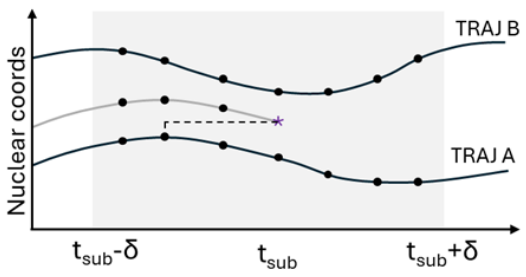

Figure 8 Schematic representation of the substitute search. The greyed-out trajectory has to be replaced. Within the same timestep, TRAJ B is the closest trajectory and will be used as a replacement; within a time window (grey region), TRAJ A is the closest, and the point at 2 steps back will be used as a replacement.

With the increase in the system's dimensionality, the chance to find a pair of trajectories with a high nuclear overlap falls dramatically. In this case, the simple overlap between pairs of trajectories will always fall below the threshold, and no substitution can be performed. In this scenario, the root mean square displacement (RMSD) can be optionally used to select trajectories. It will also use the same time window to find the best match. This alternative will always find the substitute with the highest similarity, even if it is low. Suppose this is used when replacing the spawned trajectory. In that case, this will lead to a deficit in population transfer since a trajectory that does not overlap with the child will also not overlap with the parent. On the other hand, when used after a hop to replace a trajectory completely decoupled from the other TBFs, it does not extensively affect the final result of the simulation.

Once the trajectory has been found, be it from the overlap of the RMSD, the substitution is performed, and the new coefficients are obtained from the same type of projection mentioned for trajectory elimination (Eq. (12)).

The differences are that, in this case, the projection is a square matrix, and the diagonal element of the overlap between the trajectory being substituted and the new one is artificially set to one to ensure proper inheritance of the original population. After the projection, the same normalization procedures ensure that the electronic populations and the norm are the same as before the substitution.

In the case of a failed substitution of a child trajectory, the spawn is denied, and the simulation can be concluded as failed or continued based on the input. If it fails at a hopping, the simulation can also be finished as failed, or the trajectory being removed will be eliminated normally, with projection and normalization.

3.3. Interpolated trajectories

The increase in dimensionality of the system can usually lead to difficulties. In this case, the problem is the lack of overlap between any pair of trajectories, which depends on their

positions and momenta. In traditional AIMS, this is circumvented by the spawns happening at specific points in the phase space to maximize the similarity between parent and child. This is never a criterion for a trajectory generated by usual surface hopping; consequently, the trajectories of a high-dimensional system never meet. As the interaction between coefficients depends on this overlap, either one would need an infinite number of trajectories so they can meet by chance, or the overlaps will be negligible in all cases, and the trajectories will never interact. This prohibitive condition invites the use of another approximation to make it feasible to treat large systems.

Virtual trajectories can artificially increase the number of TBFs and allow them to be added in the most critical regions of the phase space. Multiple ways to create those virtual trajectories can be imagined: the new points can be interpolated from a single trajectory, or they could be interpolated from the closest trajectories in the phase space. Alternatively, instead of simply interpolating the points of the trajectories, the actual energy surface around the spawning region could be fitted from the geometries pre-computed around it,[142] and the virtual trajectory could be propagated over this fitted potential surface. With the development of machine learning potentials,[143] we could reach a point where they are automated enough that a simple model, valid only for a short region of the phase space where the virtual trajectories are required, could be trained from the other pre-computed trajectories. Both the fitting or training of machine learning potential would be restricted to a small part of the phase space, which could potentially make those approaches computationally viable. Alternatively, one could only compute new electronic structure calculations for a reduced number of points within the coupling region. However, in this work, we want to test the method without requiring new single-point calculations. Also, while machine learning potentials have been gaining traction, they are still not straightforward enough to be used as a black box method. We will then focus only on the most straightforward and inexpensive interpolation to show the potential of the idea. There will always be a pair of trajectories: the parent, the trajectory pre-computed by surface hopping, and the spawned/child trajectory, which in QDCT is the virtual trajectory. Here, we choose to obtain the data of those virtual trajectories (gradients, energies, and couplings) by interpolating the data already available in the parent.

Those interpolated trajectories are the most important within the coupling region, where the interaction between parent and child trajectories controls the electronic population transfer. Starting at the maximum of the coupling region, the child trajectory (interpolated) has the same information as the parent, except for the current state of the trajectory and the momentum correction (Eq. (10)) to preserve total energy. At this point, the approximation expects that the forces for the two electronic states were evaluated. After interpolation, both trajectories have their forces and momenta available, and one can then compute the distance of each atom in each coordinate as

$$m_\alpha \Delta r_\alpha^{(k)} = p_\alpha^{(k)} dt_{(k)} + \frac{f_\alpha^{(k)} dt_{(k)}^2}{2}, \tag{23}$$

where *k* represents either interpolated (*i*) or original (*o*) trajectories, and α stands for each nuclear coordinate. Since both trajectories move with different momentum (*p*) and force (*f*), they will run different distances. It is possible to determine at which time the original trajectory will match in position with the interpolated one by equating the distances traveled, as in

$$p_\alpha^{(i)} dt_{(i)} + \frac{f_\alpha^{(i)} dt_{(i)}^2}{2} = p_\alpha^{(o)} dt_{(o)} + \frac{f_\alpha^{(o)} dt_{(o)}^2}{2}. \tag{24}$$

In Eq. (24), all values are fixed except by the timestep size of the original trajectory (dt_o). This quadratic equation can be solved for the smallest real positive result to obtain the time at which the values of the parent should be interpolated to get the values of the interpolated trajectory, as exemplified in Figure 9. Let us clearly state that this does not mean that the interpolated and original trajectories are moving with different timesteps. All trajectories in the simulation run with the same step size. What we are doing is, by knowing the velocity of the original trajectory, we can determine what timestep would be required for it to be in the same coordinates as the interpolated.

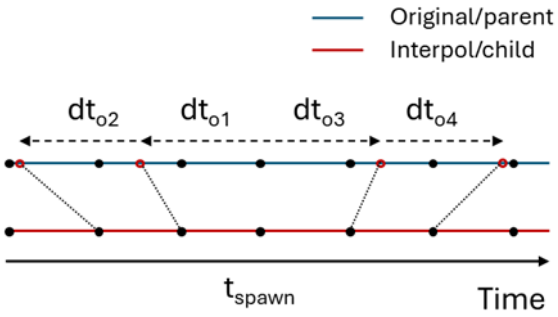

Figure 9 Scheme of creation of the interpolated trajectory using the original trajectory. In this case, the child is created in a lower state and moves faster due to momentum rescaling. The original timestep size (dt_o) is used to compute the time at which the parent and child are in the same position, and the information of the original trajectory is used to interpolate the data of the child.

With this theoretical coordinate, we can use the data around already computed to interpolate the data of the interpolated trajectory using cubic Hermite spline interpolation. For the vectorial quantities (positions, gradients), each coordinate will have an interpolation time *t*, and the interpolated value can be computed coordinate-wise, as in

$$y(t) = (2t^3 - 3t^2 + 1)y_0 + (t^3 - 2t^2 + t)\left(\frac{dy}{dt}\right)_0 + (-2t^3 + 3t^2)y_1 + (t^3 - t^2)\left(\frac{dy}{dt}\right)_1. \tag{25}$$

y(t) is the value to be interpolated, y_0 is the value on the original trajectory at the beginning of the timestep, and y_1 is the value at the end of the step. *dy/dt* are their derivatives at those same beginning and end of the timestep. The free variable *t* is normalized so that $y_0 = y(0)$ and

$y_1 = y(1)$. In some coordinates, Eq. (24) might not have a solution. In this case, we can use the average timesteps of the other coordinates and perform the interpolation normally.

Eq. (24) usually returns slightly different timestep sizes for each coordinate. This can be explained by gradients in different states giving more energy to different coordinates. Using a time for each coordinate can be justified because cartesian coordinates are orthogonal, so the force applied in one coordinate will not affect the position in another. This is why the coordinate-wise interpolation was used only for positions and gradients, while momentum is computed from the gradients. At first, we experimented with an average time for all coordinates, but we noticed that the current scheme could better approximate the interpolated trajectory from the trajectory created by conventional spawning.

Not all data will have a derivative available, so we opted to use numerical derivatives in all cases:

$$\left(\frac{dy}{dt}\right)_i = \frac{y_{i+1} - y_{i-1}}{2}. \tag{26}$$

Suppose that there is a simulation with a timestep of 0.5 a.u. and the interpolation time is at 10.2 a.u. In this case, the interpolation would use:

$$\begin{aligned} t &= \frac{(10.2 - 10.0)}{0.5} = 0.4 \\ y_{-1} &= y(9.5) \\ y_0 &= y(10.0) \\ y_1 &= y(10.5) \\ y_2 &= y(11.0) \end{aligned} \tag{27}$$

For the interpolation of the energies and coupling vectors, the time used is an average between all nuclear coordinates. Despite the coupling vector also being a vectorial quantity, we chose to interpolate it for a single time, where the molecule has a defined geometry instead of coordinate-wise. Once the interpolated gradients are computed in the new time, the momentum is also updated by using the usual Verlet algorithm:

$$p_1^{(v)} = p_0^{(v)} + \frac{f_0^{(v)} + f_1^{(v)}}{2} dt\,. \tag{28}$$

It can be noticed by looking at the Verlet algorithm and equation to propagate the coefficients in the Annex A that for the interpolated trajectory to be possible, the parent trajectory must have the gradient in the state of the child trajectory pre-computed at the surface hopping stage. At this point, both the original and interpolated trajectories have all their information computed and ready to be used, the original since it was pre-computed and the new trajectory due to the interpolation. The following timesteps can be computed following the same procedure until the interpolated trajectory is no longer required.

To a reasonable degree, around the maximum coupling point, the path they are following is still similar. By the time the trajectories have drifted apart enough to decrease the quality of the interpolation, the overlap between them will have reduced and uncoupled them. All population transfer should have happened by that point, and the trajectories can be considered independent. The larger the system's dimensionality, the faster the overlap should fall and the safer the interpolated trajectory should be.

We are not interested in the interpolation for the whole trajectory, so we need some criteria to stop interpolating. First, we check if the norm of the nonadiabatic coupling of the interpolated trajectory is decreasing. The interpolation starts at the maximum coupling, so when we are propagating forward and backward in time, away from this point, the norm of the nonadiabatic coupling vector should decrease. If it reaches an inflection point and starts to rise, it will enter a new coupling region. A new interpolated trajectory should be created to describe this new region better so the current interpolated trajectory will not be propagated further in that direction and will be substituted. Second, it checks the overlap between the interpolated child and parent trajectories. While the overlap is high, the trajectories still interact, and the interpolation should continue. After the overlap falls below a given threshold, the norm of the nonadiabatic coupling is also checked, and the interpolation stops when this norm is smaller than the threshold that defines the beginning of the coupling region.

The interpolated trajectories are necessary only to replace the child trajectories, but in the context of surface hopping, there is a chance of hops in the coupling region. The parent is also created as an interpolated trajectory to avoid dealing with trajectory hopping within the coupling region. In the case of a hop, the interpolated parent trajectory return will behave as if the trajectory remained in the same state for the whole coupling region.

After the interpolated trajectories are created, they are added to the nuclear basis, and the coefficient propagation continues. The interpolated child is added as a new trajectory, and the interpolated parent is added as a replacement. After the coefficient propagation passes through the coupling region, the overlap between the interpolated trajectories and all other TBFs is evaluated until they are entirely independent of the others and can be replaced again by another trajectory generated by FSSH. At this point, the substitution will not significantly overlap in higher dimensions. However, since the trajectory is independent of the other TBFs, this can still recover a good population description.

3.4. Method's workflow

We chose to start the coefficient propagation from a single trajectory. Then, multiple propagations can be performed starting from different initial conditions, similar to the IFGA. It is possible to attempt to start from various nuclear configurations, create a reference initial wave packet to determine the initial coefficients, and perform the propagation. However, this tends

to give good agreement with IFGA in higher dimensions,[122] especially considering we are working with many, primarily independent, trajectories.

Initially, we follow a single trajectory, but along the propagation, new trajectories will be added to the nuclear basis, reproducing a spawn. At each timestep, checks are performed to evaluate the need for spawning or substitution. This can be described by the following steps, which lead to the overall scheme represented in Figure 10:

1. **Coefficient propagation:** the data of the current and previous timesteps are used to propagate the coefficients (Eq. (7)) and the phase (Eq. (9)) to the current step;
2. **Trajectory substitution:** each trajectory is checked for a hop in the following step. In the case it hops, it would create a problem for the coefficient propagation, so the trajectory is substituted as described in Section 3.2, and the new coefficients are computed by Eq. (12). This is exemplified in time t_{H1} in Figure 10.
3. **Trajectory spawning:** the nonadiabatic couplings are compared with the given threshold to determine whether the trajectory (T_A) entered the spawning region. If so, it is followed until the maximum coupling point, independent from the rest of the simulation, and the pair of interpolated trajectories is created in the parent and child states (i-T_AS_0 and i-T_AS_1), as explained in Section 3.3. The values of the interpolated trajectories are interpolated from the parent trajectory (T_A) as per Eq. (25). They are added to the nuclear basis at times t_{C1} (in Figure 10) and used normally for the coefficient propagation, as any other trajectory originated from surface hopping. The interpolated trajectories are not evaluated for new spawns;
4. **Interpolated substitution:** the interpolated trajectories are interpolated only within the coupling region, so they must be replaced after this interval. The same check as in step 2 is used to replace the interpolated trajectory with another pre-computed from surface hopping at the end of the interpolation region, marked with times t_{S1} in Figure 10. Notice that in t_{S1} and t_{S4}, the interpolated is replaced by the same trajectory that originated it, so they should be a good match, while in t_{S2} and t_{S3} a new trajectory is replacing the interpolated, and there will be a difference in positions and other values between trajectories. The original trajectory might remain in the same state during the coupling region, as in t_{S1}, or might have hopped and will be replaced accordingly, as in t_{S4};
5. **Trajectory elimination:** in case of a failed substitution in step 2 or following the criteria of low population and coupling with the TBFs mentioned in Section 2.2.2, a trajectory can be removed, as in t_{E1} in Figure 10. At this point, the wavepacket before the removal is projected into the remaining trajectories to obtain the optimal coefficients (Eq. (12));

6. **Closing the step:** update the timestep of the classical trajectories and return to step 1 to continue the propagation.

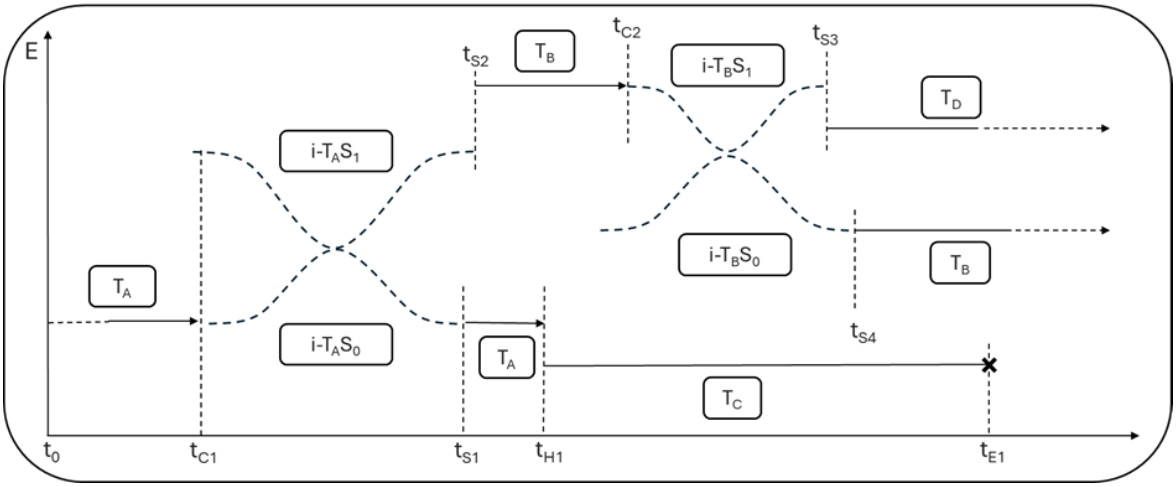

Figure 10 Schematic representation of the management of classical trajectories computed with surface hopping (T_A, T_B, T_C, and T_D) or interpolated trajectories (i-T_AS_0, i-T_AS_1, i-T_BS_0, and i-T_BS_1) during a QDCT propagation and the critical events that can happen: t_C spawning with the creation of interpolated trajectories; t_S end of coupling region with the substitution of interpolated trajectories by an original one; t_H hop of the surface hopping trajectory, triggering a substitution; t_E trajectory elimination due to low population.

This process can be started independently for all or part of the trajectories available from surface hopping. As is the case for AIMS simulations,[115] QDCT needs fewer initial conditions to converge, so starting from all the trajectories may not be necessary. After propagation, the properties of interest, such as the population, can be computed using Eq. (13), as one would do for conventional multiple spawning. The expectation value can be computed for each simulation starting from independent initial conditions (IFGA). The final value is the simple average between multiple simulations.

3.5. Computational details

The FSSH calculations were performed in Newton-X v3.5.1[59] using the decoherence correction from Granucci and Persico.[98] The multiple spawning references were computed using Legion, described in Chapter 4. . The QDCT post-processing was performed with a code developed for this project, available at https://gitlab.com/rafaelcpii93/qdct.

For the unidimensional testing, the Tully models[91] were used (Figure 11). The trajectories are sampled from a Wigner distribution of a Gaussian wavepacket[59,144] around the position -8 a_0 for models A and B in Figure 11 and position -15 a_0 for model C. In all cases, different initial momenta were used. During the initial sampling, the width for the Gaussian followed Tully's original recommendation of $\Delta_p = 20/p_0$. The mass was set as 2000 m_e, and the Gaussian width for both multiple spawning propagation and QDCT was chosen to be 4.7 a_0^{-2}.

The trajectories start on the ground state and are propagated with a timestep of 0.1 fs. The common parameters between the multiple spawning and QDCT simulations shared the same values. The coupling threshold is achieved when the norm of the NAC vector passes the value 0.08 a.u.$^{-1}$, and the absolute value of the overlap between child and parent is 0.7 to accept a spawn. The BAT approximation was also used in the multiple spawning calculations to enable a clearer comparison with QDCT. The comparison between the BAT and SPA results can be found in Annex B. In QDCT, a time window of 60 timesteps around the simulation time was used when looking at trajectories for substitution, and the threshold of the absolute value of the overlap to accept a substitution is 0.9.

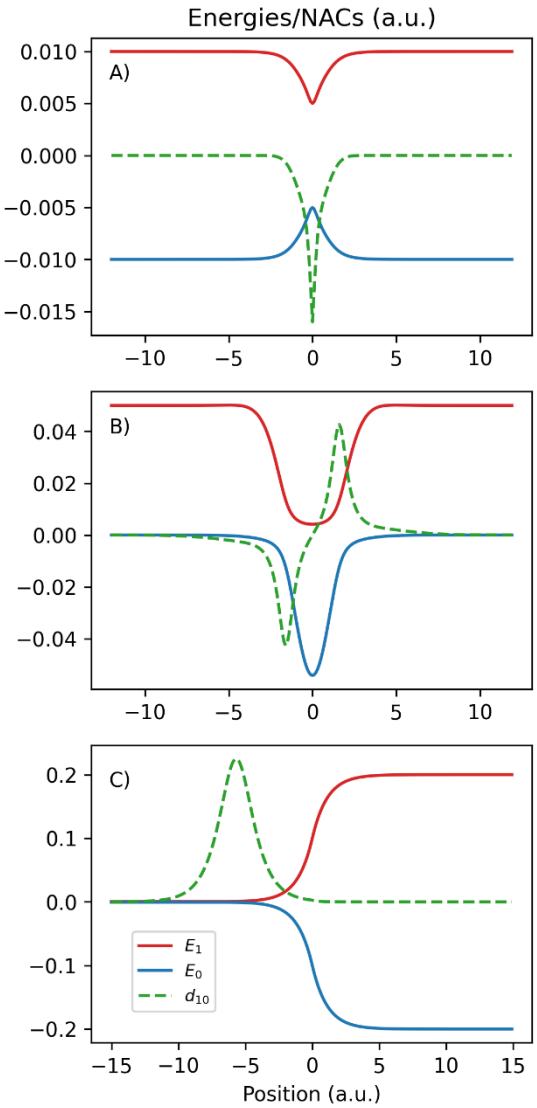

Figure 11 Tully model potentials in adiabatic representation. Energies and nonadiabatic couplings from E_1 to E_0 in a.u. The presented d_{10} values are rescaled to fit with the energies: A) Simple avoided crossing $d_{10}/100$, B) Dual avoided crossing $d_{10}/20$, and C) Extended coupling with reflection d_{10} without rescaling.

A total of 500 initial conditions were used for all calculations, starting at the lower electronic state. The same initial conditions were used for the surface hopping, multiple

spawning, and, consequently, the QDCT simulations. This number of initial conditions is low for treating analytical models, which usually is in the thousands for surface hopping.[91,145,146] Nevertheless, we chose to use fewer trajectories to show the potential of the method, considering that a routine ab initio simulation tends to have between 100 and 200 trajectories.[114,128,147]

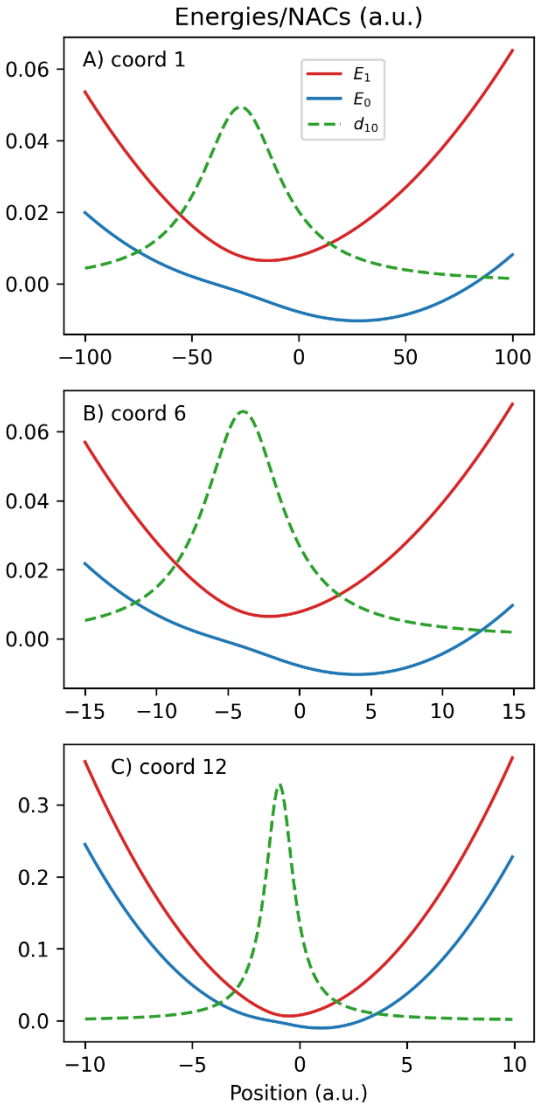

Figure 12 Cuts of the SBH model potential in adiabatic representation. Energies of E_0 and E_1 and the nonadiabatic coupling norm in a.u from state 1 to state 0. The presented d_{10} values are rescaled to fit with the energies. The panels show profiles along A) coordinate 1 ($\omega = 14 cm^{-1}$), $d_{10}/20$; B) coordinate 6 ($\omega = 96 cm^{-1}$), $d_{10}/15$; and C) coordinate 12 ($\omega = 400 cm^{-1}$), $d_{10}/3$.

For the multidimensional test, we used the spin-boson Hamiltonian[148–151] model with 12 dimensions. The functional form, parameters for this system (and also the Tully models), and adiabatic transformation are found in the Annex C. In Figure 12, we present cuts of the potential energies and the norm of the nonadiabatic coupling over three coordinates: A) the coordinate associated with the lowest vibrational frequency; B) a coordinate associated with a medium-

valued frequency; C) the coordinate associated with the highest frequency in the model. Other than testing QDCT in a multidimensional case, the model was parametrized such that the nonadiabatic transitions occur in 0.5 ps simulation time (a typical timescale for ultrafast photodynamics) to test the data management capability of the software.

Most parameters used in the 1D case are kept the same in the multidimensional tests. In this case, the population threshold to remove a trajectory is 0.01 in multiple spawning and QDCT. The same initial conditions were used for the multiple spawning and surface hopping dynamics for the sets with 100 and 500 trajectories. The particles used were hydrogen atoms with a mass of 1822 m_e. They were sampled from a Wigner distribution around the minimum position of the ground state with zero average initial momentum and then vertically lifted to the first excited state.

All the populations presented show the average value in the lines and the confidence interval of 95% in the shaded area. The averages and standard deviation were computed using the bootstrap method using 100000 resamples.

3.6. Application

3.6.1. Unidimensional systems

3.6.1.1. Tully 1: Simple avoided crossing

The simple avoided model is characterized by the potential energy surfaces coming reasonably close (≈ 0.27 eV) once but never crossing each other (Figure 11-A). Depending on the initial velocity, this can cause a partial transfer to the upper state.

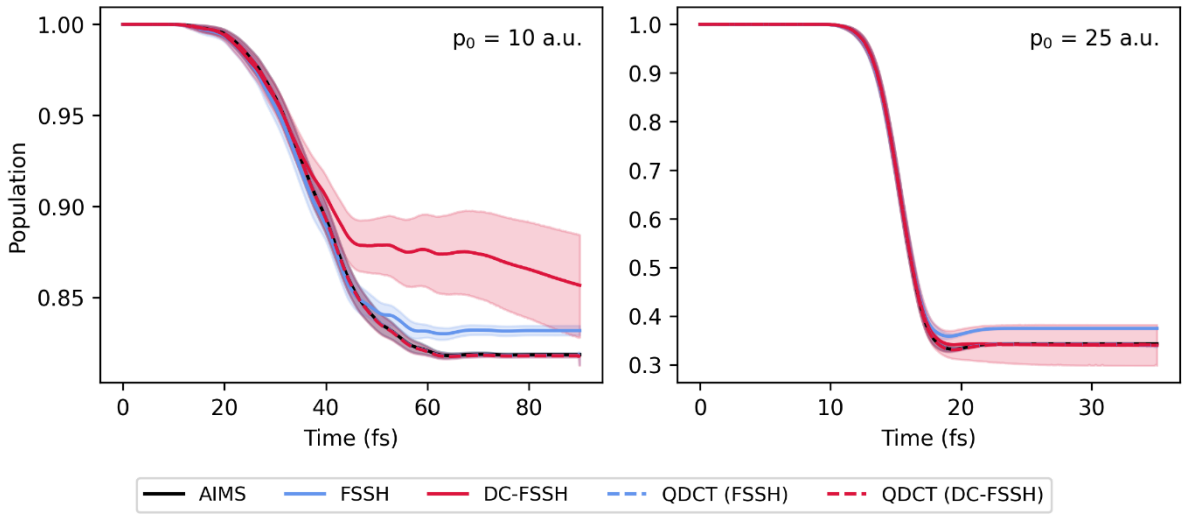

Figure 13 Lower state population for the simple avoided crossing Tully model. The initial condition was sampled around the momenta of 10 a.u. and 25 a.u. The shaded area in all curves represents a confidence interval of 95%.

In general, surface hopping should be performed with decoherence correction. As can be seen in Figure 13, in the low initial momentum, the DC-FSSH population underestimates the transfer, and even as the trajectories have already left the coupling region beyond 80 fs, the population is still not stabilized. Compared to the trajectories without decoherence correction, the confidence interval is much wider for the corrected trajectories. The original FSSH algorithm is much closer to the behavior of the AIMS population and the results found in previous work for this model.[145] When applied to both the trajectories generated by FSSH and DC-FSSH, QDCT recovers the AIMS population and, most importantly, does the same for both surface hopping outputs. The larger confidence interval in DC-FSSH is the effect of the decoherence correction tempering with the coefficients. In Annex D, there is a short discussion of this topic with an example.

In the case of higher initial momentum, where the particle behaves more like a classical particle and surface hopping should work better,[91,99] there is a good agreement between all methods. In this case, the DC-FSSH is closer to the reference than the original FSSH. Even with the improved result, the corrected decoherence still has a wider confidence interval than the other methods. Once again, QDCT can improve the population of the FSSH and not alter the result of DC-FSSH other than reducing the confidence interval.

The take-home message here (and in the following sections) is not that QDCT corrects DC-FSSH to return uncorrected FSSH, but that QDCT will return satisfactory results no matter the quality of the initial surface hopping basis we have.

3.6.1.2. Tully 2: Dual avoided crossing

The second of the Tully models is the dual avoided crossing, characterized by two sequential regions of high coupling where the potential energy surfaces approach each other (Figure 11-B). The small interval between the pair of couplings makes it possibly the hardest of the three models.[146,152]

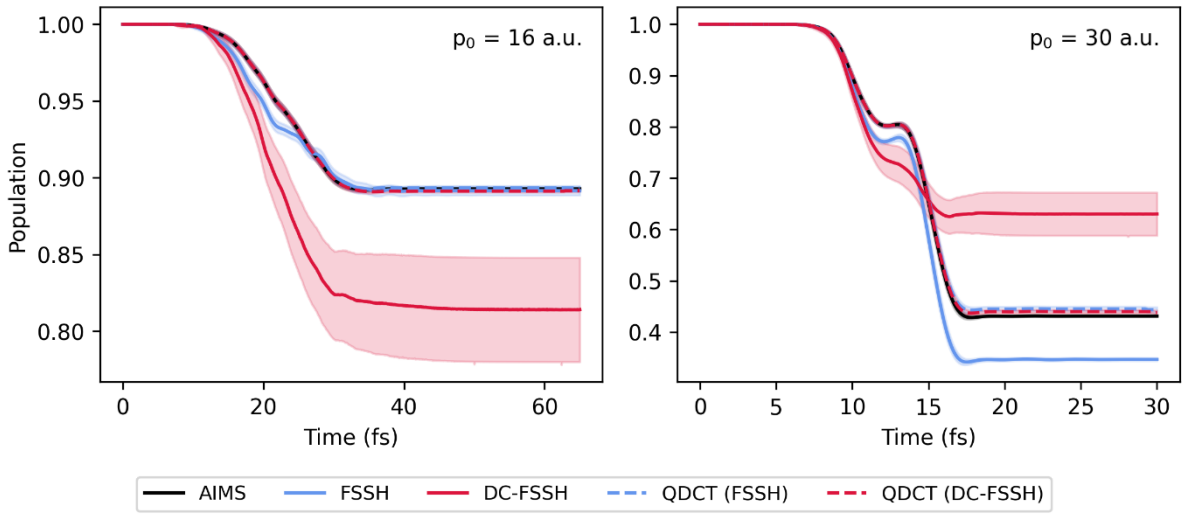

Figure 14 Lower state population for the dual avoided crossing Tully. The initial condition was sampled around the momenta of 16 a.u. and 30 a.u. The shaded area in all curves represents a confidence interval of 95%.

Once again, Figure 14 shows that using decoherence correction returns the asymptotic population 0.1 smaller than the reference for the lower momentum. On the other hand, despite having a slight difference in the transfer region, the original FSSH agrees with the AIMS asymptotic result.

In the high initial momentum simulations, the DC-FSSH disagrees even more with the reference. In this case, even the original FSSH disagrees with the AIMS result. The difficulty of FSSH in dealing with the sequential coupling regions has already been observed for this model.[146] When this system reaches the second coupling region, the fine control of the decoherence should influence the remaining transfer between states. It could be related to the large discrepancy between this system's expected behavior and what is observed with DC-FSSH. Also, in this case, the QDCT recovers the AIMS result for both initial momenta and for both sets of surface hopping trajectories.

3.6.1.3. Tully 3: Extended coupling with reflection

The last unidimensional model starts in a region where the upper and lower electronic surfaces are degenerated. They pass through a coupling region, and the energies separate (Figure 11-C). If the trajectories that go through the upper state do not have enough kinetic energy, they are reflected and cause a second wave of population transfer, as can be seen in Figure 15.

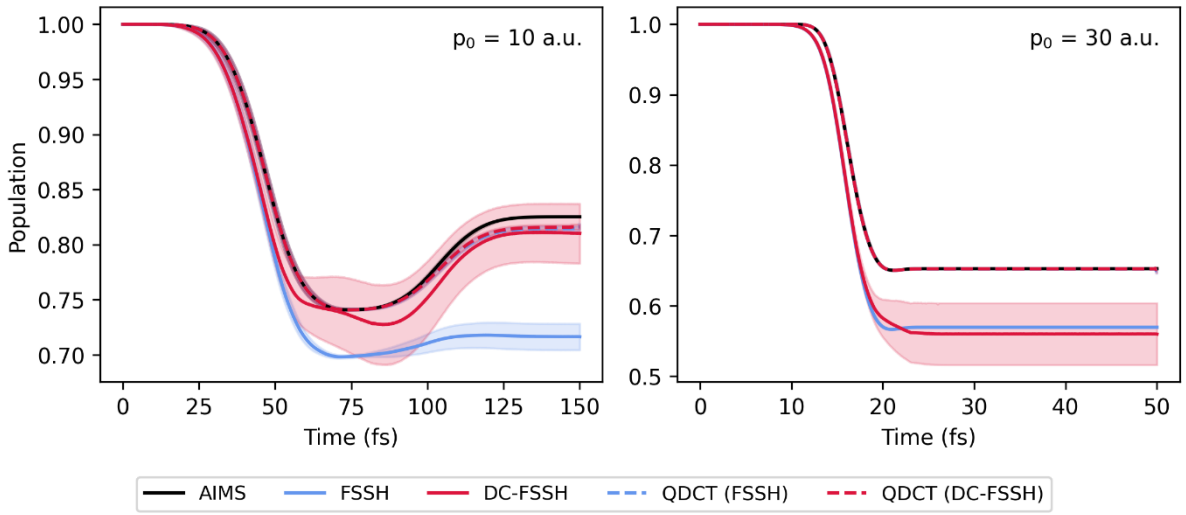

Figure 15 Lower state population for the simple avoided crossing Tully model. The initial condition was sampled around the momenta of 10 a.u. and 30 a.u. The shaded area in all curves represents a confidence interval of 95%.

For the low momentum case, most of the methods recover the population being transferred back to the lower state when the trajectories in the upper state are reflected. DC-FSSH has a slightly different profile from the reference but agrees with it overall. Original FSSH almost has no population being transferred back and has a wider confidence interval than observed in the other models. In the high-momentum case, the trajectories have enough kinetic energy to overcome the barrier in the upper state. Once the initial transfer is completed, the populations remain constant. Curiously, in this case, both surface hopping results agree among themselves but deviate from the reference. Once again, QDCT approximates the reference well, with a slight deviation in the low momentum case.

3.6.2. Multidimensional system

Although testing new methods in the Tully models is standard practice in the development of nonadiabatic dynamics, they are all unidimensional. To be practical, QDCT should also be able to deal with larger systems. This creates a problem that uncorrelated trajectories in higher dimensions will rarely, if ever, have a significant overlap, which is essential for communication and population transfer between them. The Annex E exemplifies how the overlap falls with increasing system dimensionality. The interpolated trajectories are required for the method to keep working in this scenario.

The Spin-Boson Hamiltonian is a family of models used to test nonadiabatic dynamic methods with the feature that its dimensionality can be arbitrarily increased. It linearly couples a two-state system (analogous to a spin-half system) to a bath of harmonic oscillator modes (the bosons). Due to its flexibility and rich dynamics, SBH has played a central role in the discussion of phenomena ranging from decoherence to nonadiabatic dynamics.[153] SBH is defined in terms of diabatic potentials for the bosonic modes. However, for surface hopping and multiple

spawning, we move to the adiabatic representation (see Annex C). In this representation, the SBH model gives rise to two-state, multidimensional potential energy surfaces with significant anharmonicities and crossings analogous to a molecular system.

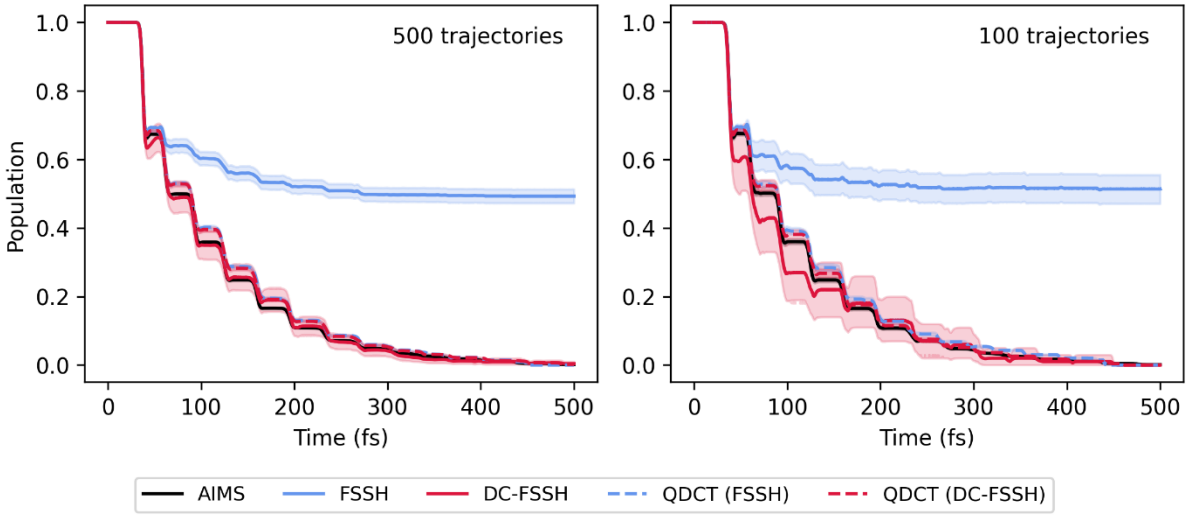

Figure 16 Upper state population for the SBH model using 500 trajectories (left) and 100 (right). The shaded area in all curves represents a confidence interval of 95%.

In the SBH model, we can see from Figure 16-left that the decoherence correction makes a difference and allows surface hopping to recover the correct result. This contrasts with the original FSSH, which considerably underestimates the population transfer, with an asymptotic population for the upper state above 50% at the end of the simulation. This illustrates a more realistic situation where decoherence corrections are essential. Although most methods agree well, DC-FSSH is generally closer to the reference population than the QDCT-corrected dynamics. In this case, the agreement of the different methods can be used to increase confidence in the result.

The result from Figure 16-left is from a converged simulation with 500 trajectories. Due to the cost of the single-point calculations, it is uncommon to see such many trajectories for an *ab initio* method. If, instead, we take only the first 100 trajectories of AIMS and (DC-)FSSH to average and to give as input to QDCT, Figure 16-right shows how one can take advantage of the faster convergence of the multiple spawning method to improve the statistics of the surface hopping results. In this case, AIMS and QDCT give essentially the same result with the smaller number of trajectories as they did with the larger one. At the same time, DC-FSSH overestimates the population transfer in the first half of the simulation. The original FSSH shows a good convergence to a wrong result, showing that just ensuring convergence does not guarantee the quality of the result. The example of Figure 16-right is likely the closest to an actual application of the method, considering the number of trajectories used and that it is a multidimensional system. It does not show a significant improvement over DC-FSSH results but still converges well with the number of trajectories.

3.7. Conclusion

We have shown here the first steps of QDCT, a strategy to post-process surface hopping dynamics to obtain results at multiple spawning levels. QDCT helps to detect and correct potential problems in surface hopping. It can, for instance, be used as a method to recover decoherence effects in an over-coherent simulation. Even when QDCT leads to the same result as surface hopping, it comes at almost no extra cost since QDCT requires no new electronic structure calculation and increases confidence in the original simulation. If, on the other hand, the methods disagree in the behavior of the dynamics, QDCT can point to a problematic system that should be studied further, revealing possible problems with an analysis that would be otherwise considered correct.

The collection of unidimensional cases shows how, in some cases, the surface hopping dynamics can converge to an incorrect result. For a new system, there is no way to determine that other than by comparing it with different dynamics methods. In a multidimensional scenario, especially with heavier atoms, the system is supposed to approach classical behavior more, which is reflected in the vast success of surface hopping methods. Yet, approximations or corrections are necessary. Some should fare better in one type of system and worse in others. QDCT approaches this problem from a different perspective and is not susceptible to those approximations. Given the non-stochastic nature of the method and the increase of the basis size during the propagation, QDCT inherits from multiple spawning its improved convergence with the number of initial conditions, which can also be leveraged to improve the confidence in the initial results from surface hopping.

This post-process method inherits the problems of energy conservation of frozen Gaussian propagation used in AIMS,[154–156] but we also have the fact that the classical trajectories will have, in general, different total energies, as chosen in the initial condition generation of the surface hopping trajectories. In that case, the total energy of each simulation will be within the range of total energies of the trajectories, with a particular case that the expected value of the energy will be a weighted average of the energies of each trajectory when the overlap between all trajectories is negligible.

The quality of FSSH results depends significantly on how the electronic coefficients are propagated and corrected along the simulation. They will then only affect the classical trajectories by influencing the hopping points. QDCT is indifferent to those coefficients from surface hopping. As long as there are enough trajectories and the electronic structure used is reliable, the method should be able to approximate AIMS, as has been shown.

Although our entire discussion has focused on post-processing FSSH trajectories, QDCT can work on any surface hopping basis, stochastic[157] or deterministic,[158] even when nonadiabatic coupling vectors are not available, such as in curvature-based approaches[95,138,139]

or global probability estimates.[159–163] In this case, however, it becomes necessary to modify the coefficient equation of motion (Eq. (7)) to replace the nonadiabatic coupling with the time derivative coupling.[126,134]

QDCT depends on a series of approximations. While some are more established, such as the BAT approximation, some can still be crude and invite extensive testing and refinement, particularly the interpolated trajectories. We plan to have our multiple spawning reference script interfaced with electronic structure codes to allow testing with real molecules. We will also investigate how the train of trajectories[104,141] and linear dependence removal[164] can improve the robustness of the QDCT method.

Although we have exclusively used QDCT to deliver results at a multiple-spawning calculation level, it is not restricted to trajectory spawning. It should be possible to emulate any strategy that uses Gaussian functions as a basis to propagate the TDSE: trains of trajectories and widths propagation, for example. Thus, in principle, we could devise QDCT versions that would aim to assess and improve the surface hopping quality against other quantum dynamics levels.

4. Legion

The content of this chapter will give origin to the following publication:

R. S. Mattos, S. Mukherjee, M. Barbatti, Legion: a Platform for Mixed Quantum-Classical Nonadiabatic Dynamics, (2024). In preparation.

The main code can be downloaded from https://gitlab.com/rafaelcpii93/legion.git

---

This chapter presents the newly developed Legion, a platform for mixed quantum-classical nonadiabatic dynamics propagation, specifically AIMS, created within the Newton-X platform[59] and is one of the products of this thesis. During the development of QDCT (Chapter 3.), we noticed a lack of options for easily accessible and efficient multiple spawning software with a large variety of electronic structure interfaces. Legion improves on those two aspects. It is intended to be a modular program that allows for the easy implementation and testing of new methods and approximations in the family of Gaussian wavepacket propagation. The software is written as a combination of Python for data management and Fortran for numerical operations. It is interfaced with multiple widely used electronic structure software, with some interfaced directly and others being intermediated by Newton-X. Among those interfaces, there are methods from semi-empirical and machine learning potentials up to CASPT2 and MRCI. We have decided to start development by implementing multiple spawning for nuclear propagation and trajectory management. Still, Legion should be understood as a playground for testing different methods.

The program follows the same heuristics and equations as expected for AIMS that was presented in Section 2.2. The method is also extended to include alternative ways to compute the TDC without requiring the explicit computation of the nonadiabatic coupling, as discussed in Section 2.3. Using orbital overlap to compute the time derivative coupling is not widespread in the multiple spawning literature but has been proposed and used before. To the best of our knowledge, this is the first time that TDBA has been proposed in the context of multiple spawning, and it will extend the number of electronic structure methods available for AIMS.

4.1. Legion in a Nutshell

The program comprises independent building blocks that can be personalized depending on the method intended. In the initialization, the appropriate objects will be loaded according

to the parameters defined in the input file, and they can perform their task independently of the other parts:

- *Ensemble*: aggregates the classical trajectories and the simulation information, like the overlaps and Hamiltonians used for coefficient propagation. Not only does it store the information, but it is the interface that creates new trajectories and their centroids or removes them from the simulation;
- *Nuclear Interface*: indicates how the Hamiltonian will be computed and the forces for the classical propagation. For AIMS, the Hamiltonian is the one presented in Eq. (7), and the force is merely the negative of the gradient of the current state of the trajectory;
- *Time Derivative Coupling*: if the nonadiabatic coupling vector is not read from the electronic structure, this is going to be responsible for computing the time derivative coupling using the alternative methods based on overlap (Eq. (19)) of the Baeck-An coupling (Eq. (21));
- *Integrator*: responsible for performing the coefficient integration using one of the methods implemented. Various methods are available, including Runge-Kutta integration, Hamiltonian diagonalization, and Magnus expansion, which contain different orders and adaptive step sizes to ensure convergence. In the case of adaptive step size integration, the intermediary points are not computed with electronic structure calculations but interpolated with a cubic Hermite spline interpolation;
- *Coefficient Integration*: is the interface between the trajectory information and the integrator. It computes the Hamiltonians required for the integrator and creates the interpolation that the integrator will use;
- *Spawning*: is responsible for keeping track of which trajectories should be spawning, and in the positive case, creates the new trajectory to add to the nuclear basis. It performs the propagation of the parent trajectory up to the maximum coupling point, creation of the child with energy conservation and momentum correction in the nonadiabatic coupling vector or momentum direction, and backpropagation of the child;
- *Dynamics*: this module combines all the previous ones, calling each one of them when necessary. It contains the initialization of the dynamics and the propagation up until the maximum time, as described in Figure 17.

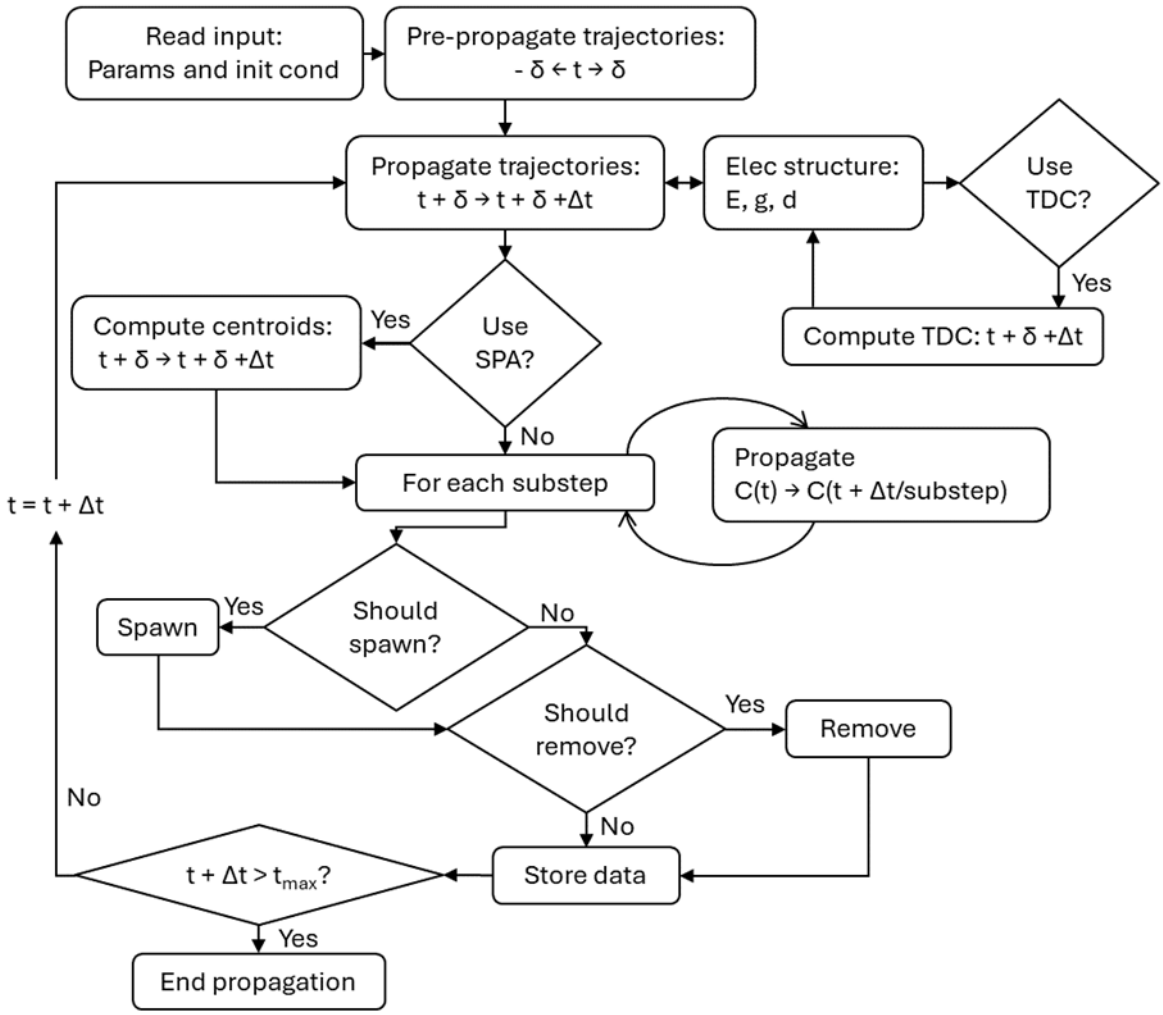

Figure 17 Flowchart of Legion. δ is the number of steps in the classical trajectories are being propagated ahead of the coefficient, useful for the TDBA and interpolation approximations. Before starting the dynamics, the pre-propagation ensures that there will be enough points since time $t = 0$ to compute the centroid numerical derivatives and interpolation.

In some situations, running the trajectory propagation with some extra time steps with respect to the coefficient integration might be interesting. For example, suppose one is computing the time derivative coupling using the TDBA approach. In that case, it is better to calculate the numerical second derivative of energy if one has information on the energy at a future time step, as seen in Eq. (22). In this case, Legion will automatically propagate the TBF one step ahead of the coefficients. This is possible because trajectory propagation is not dependent on the coefficients; they are only integrated synchronously so that the information on the population can be used when choosing to remove trajectories from the nuclear basis.

To perform frozen Gaussian propagation, the Gaussian width has to be chosen for each atom. Legion can read the widths from the geometry file, and also has as default the values recommended in the literature.[123] Those values are restricted to the first rows in the periodic table. In a recent work, Tomaz *et al*[165] fitted a formula to obtain the Gaussian width for any

element in the periodic table, computed from their atomic radius, and it allows multiple spawning to be used with almost any element on the periodic table. The fitted formula is:

$$(2\omega)^{-1/2} = 6255\exp(-R_{at}/0.139) + 0.0744, \quad (29)$$

where ω is the Gaussian width, and R_{at} is the atomic radius.[166]

The initial condition necessary to start the dynamics propagation consists of two pieces of information: the initial geometry and velocity of the molecule at time zero. Legion is a software for performing the propagation of the dynamics, and for now, it does not contain a method to generate the initial condition. The Newton-X CS within the Newton-X platform provides their generation to the user. This uses the nuclear ensemble approach (NEA)[167,168] to generate initial conditions and spectrum, usually employing the Wigner probability distribution function to generate the geometries and velocities.[169]

4.2. Legion in Depth

4.2.1. Modified BAT approximation

We present a newly developed modification to the bra-ket averaged Taylor approximation that has never been published before. A zeroth-order Taylor expansion approximates the centroid value for the NAC and, consequently, the TDC. Within this approximation, those curves are assumed to behave as straight lines, but the nonadiabatic coupling is known for its fast variation around a small region of the phase space. It behaves much more similar to an exponential function, where *A* and *B* are the fitted constants, and *x* is the free variable:

$$f(x) = A\exp(xB). \quad (30)$$

Under that assumption, one can use the same information used in the standard BAT to fit an exponential that passes through the values of the NAC curve at both trajectories, *i* at *x = 0* and *j* at *x = 1*, and ρ runs through the coordinates:

$$A_\rho = d_{IJ\rho}(\bar{R}_i),$$
$$B_\rho = \ln\left(\frac{d_{IJ\rho}(\bar{R}_j)}{d_{IJ\rho}(\bar{R}_i)}\right). \quad (31)$$

Then, knowing that the centroid is found in the middle of those two points, the centroid value can be computed at *x = 0.5*:

$$d_{IJ\rho}(\bar{R}_c) = \sqrt{ABS(d_{IJ\rho}(\bar{R}_i) \times d_{IJ\rho}(\bar{R}_j))}. \quad (32)$$

To compute the square root, we take the absolute value of the product of the elements of the coupling vector. The couplings at trajectories *i* and *j* are compared; the one with the smallest

norm will dictate the sign of the vector at the centroid. The justification is that for an exponential curve, the value at the middle is closer to the smaller value.

The same relation can be used to compute the centroid TDC when the NACs are not used. In the results, this is shown as the bra-ket averaged Taylor/exponential (BATE) approximation.

4.2.2. Adaptive timestep

A feature that improves efficiency is the capability to propagate the classical trajectories with fewer single-point calculations far from the coupling region and reduce the classical step size within this region. The implementation is inspired by the idea of substeps used for surface hopping.[57,59] In that case, the timestep used for integrating the coefficients has to be smaller than the timestep for the classical propagation, so intermediate values are interpolated and used for coefficient propagation. Far from the coupling region, the systems behave better, and the usual timestep of 0.5 fs should be enough for a smooth integration of the classical trajectories. Within the coupling region, the nonadiabatic coupling varies fast, and a smaller integration step will be able to capture it better.

In Legion, the user defines the number of substeps to compute and the total timestep of the dynamic. During the propagation of the classical trajectories, if they are below the coupling threshold, the classical integration of the nuclei takes the full timestep, and the substep points are interpolated using the cubic Hermite spline interpolation:

$$y(t) = (2t^3 - 3t^2 + 1)y_0 + (t^3 - 2t^2 + t)\left(\frac{dy}{dt}\right)_0 + (-2t^3 + 3t^2)y_1 + (t^3 - t^2)\left(\frac{dy}{dt}\right)_1. \quad (33)$$

In it, $y(t)$ is the value to be interpolated, y_0 is the value on the original trajectory at the beginning of the timestep, and y_1 is the value at the end of the step. dy/dt are their derivatives at those same beginning and end of the timestep. The free variable t is normalized so that $y_0 = y(0)$ and $y_1 = y(1)$. The spline interpolation ensures that the points and first derivatives of the exact function and the interpolated one are the same at the extremes of the interpolation interval. Not all properties will have a derivative available, so they can be computed using the numerical derivatives in all cases:

$$\left(\frac{dy}{dt}\right)_i = \frac{y_{i+1} - y_{i-1}}{2}. \quad (34)$$

This again uses trajectories propagated ahead of the coefficient to evaluate derivatives using the central difference. If the classical trajectories have crossed the coupling threshold, using the same criteria checked for spawning, then instead of interpolation, the timestep is reduced to the size of the substep, and no interpolation is necessary.

The coefficient integration is unaware of this process and computes the new coefficients for each substep. This way, part of the trajectories may be within the coupling region and are

propagated every substep, while the other part takes larger steps, and the data is complemented with interpolation.

4.2.3. Electronic structure interfaces

Legion requires an external electronic structure program to propagate the classical trajectories. This program is responsible for computing the energies, gradients, and, optionally, nonadiabatic couplings. Living under the umbrella of the Newton-X platform, Legion inherits all the methods interfaced with Newton-X through external calls. Those calls are responsible for adapting the input for the different electronic structure programs, calling them, reading their outputs, and returning them all in a structured, unified format. Newton-X will also be responsible for reading the orbital at different timesteps and calling the CIOverlap[132] program to compute the overlap of subsequent timesteps used in Eq. (19). This interface is seamless for the user, who is not required to be familiar with Newton-X or surface hopping to use Legion. We do not imply that the program can only be used with Newton-X, but new direct interfaces have yet to be added as the need arises. This intermediary interface calls conventional electronic structure software, and the possible overhead of passing through the Newton-X call is negligible.

In recent years, semi-empirical methods[170–177] and machine learning potentials[178–180] have been gaining popularity. In this case, the single-point calculation is so fast that small overheads can start to impact the performance of the simulation. For that case, we have created a direct interface to MLatom,[143,163] an independent software that implements those faster methods. Since MLatom is provided as a Python API, we can call it from within the Legion interface. This can be significant for speeding up since calculating energies with machine learning potential is so fast that importing the Python libraries at each time step can take a noticeable chunk of the time. Being called from the interface, MLatom is initiated only once, getting rid of the overhead caused by reinitializing it multiple times.

A third direct interface is present for PySCF,[181] a general-purpose electronic structure software with multiple methods that have been amply developed. It follows the philosophy of being a modular software that gives flexibility for developing new methods. The program is also provided as a Python API, which means it is also called from within its interface, similar to MLatom. The complete list of programs and methods interfaced with Legion is available in Table 1.

Table 1 Programs and Methods Interfaced with Legion.

program	methods	couplings
COLUMBUS[a]	MCSCF, MRCI	nacv, cioverlap, TDBA
TURBOMOLE[a]	RICC2, ADC2, TDDFT	nacv, cioverlap, TDBA
ORCA[a]	TDDFT	cioverlap, TDBA
GAUSSIAN[a]	TDDFT	nacv, cioverlap, TDBA

OpenMolcas[a]	RASSCF, CASPT2	nacv, TDBA
MOPAC (Pisa)[a]	FOMO-CI	nacv, third-party overlap, TDBA
MNDO[a]	OMx/MRCI	nacv, TDBA
OQP[a]	MRSF/TDDFT	TDBA
MLatom	AIQM1/ML potentials	TDBA
PySCF	TDDFT, ADC2, MCSCF	TDBA, nacv
build-in codes	Analytical models	nacv, TDBA

[a]Program interface mediated by Newton-X NS.

4.2.4. Input and output

The input is composed of three parts:

- a single input file with the options to be used by Legion, defining multiple parameters of the dynamics. Most of them contain default values, except information such as the number of electronic states to consider and maximum simulation time;
- a pair of files containing the initial geometry and velocity of the first trajectory in xyz format;
- a folder containing the input to run the electronic structure calculation.

The output is composed of a folder for each trajectory containing its information: positions, momenta, gradients, energies, and coefficients. If the electronic structure methods compute the nonadiabatic coupling vectors, those will also be present. If the coupling is calculated with one of the auxiliary methods, then the time derivative coupling will be saved to a text file. The same information is stored in extra folders containing the centroid if the user decides to use the SPA approximation. Those trajectories are stored in a format compatible with Newton-X so that Ulamdyn[59] can be used to analyze them.

Outside the trajectory folders, the matrices used to propagate the coefficient are also stored: S, Sdot, V, T, and τ. The electronic population and the coherences of the wavepacket are also printed, together with the complete list of parameters and their respective values used in that simulation, including the default ones.

4.3. Computational details

To validate Legion, we performed dynamics of fulvene and DMABN (4-(N,N-dimethylamino)benzonitrile) using multiple electronic structure methods implemented in various software. The simulations were performed interfaced with a development version of Newton-X NS 3.5.2,[59] with electronic structure calculations computed with OpenMolcas 24.06,[182–184] for complete active space self-consistent field (CASSCF) and complete active space perturbation theory of second order (CASPT2), Columbus 7.2[185–187] for CASSCF, and Orca v5.0.4[188,189] and Gaussian 16[190] for the time-dependent density functional theory (TDDFT) calculations.

For fulvene, we used two sets of initial conditions. One set contains the first 20 initial conditions from the set of dynamics in Ref[128], generated from a harmonic oscillator Wigner distribution. The other set contains 18 trajectories, also generated from a harmonic Wigner sampling, but the momenta was set to zero.[114] A set of dynamics was run using SA-2-CASSCF(6,6) in Columbus and OpenMolcas, consisting of the 3 pairs of bonding π and anti-bonding π* orbitals. Dynamics with extended multistate (XMS) CASPT2 used the same active space through the OpenMolcas interface. In all cases, the 6-31g* was the basis set. The propagation started from the first excited state (S_1) and continued up until 45 fs with a full timestep of 0.5 fs and a sub-timestep in the coupling region of 0.1 fs. The population limit to allow spawning or trajectory elimination was 0.01, and the overlap threshold between trajectories to allow spawning was set to 0.6. The coupling criteria used was the time derivative coupling ($\boldsymbol{v}\cdot\boldsymbol{d}_{ij}$), with a threshold of 0.01 a.u.$^{-1}$. In most cases, the NAC was computed by the electronic structure calculation, and the momentum was corrected along the NAC direction at spawning time. Different sets of calculations were performed, varying the coupling threshold, type of coupling (NAC vs TDBA), the centroid method (SPA, BAT, BATE), and direction of momentum correction, either in the direction of the NAC or the momentum vector.

For DMABN, we used the 21 initial conditions presented in Ref[114], also generated from a harmonic Wigner distribution. The sets of dynamics used LC-ωHPBE[191]/6-31g in Gaussian and ωB97X-D3[192]/def2-SV(P) in Orca, using the Tamm-Dancoff Approximation (TDA) and RIJCOSX[193] to approximate Coulomb integrals. In both cases, the lowest three excited states were asked. The dynamics started from the second excited state (S_2) and propagated until 100 fs, with a full timestep of 0.5 fs and a step of 0.1 fs in the coupling region. The population to kill and spawn is 0.1, the overlap threshold is 0.6. The coupling criteria is the TDC computed with TDBA with a threshold of 0.005 a.u.$^{-1}$. In all sets of dynamics the coupling was computed using TDBA, varying the centroid method (BAT, BATE).

4.4. Application

When Tully proposed the FSSH dynamics, he validated the method using three one-dimensional analytical models that could also be solved numerically.[91] Those models were amply adopted for testing algorithms, but they are very simplified representations of avoided crossing and coupling with reflection. In a newer publication, Ibele and Curchod proposed three molecules to be used as analogous to the Tully models.[114] Of those molecules, we chose Fulvene and DMABN (Figure 18) to validate Legion.

Fulvene is widely used in nonadiabatic dynamics benchmarks[120,128,138,147,154] due to its ultrafast relaxation time and rigidity, which allow for stable complete active space (CAS) calculation throughout the propagation. Previous CASSCF calculations with multiple spawning[114,154] and surface hopping[114,128] have been characterized mainly by two deactivation

channels: a stretch of the $C=CH_2$ involving a sloped conical intersection and a twist of the same bond involving a peaked conical intersection. The intense population transfer previously observed for CASSCF starts at the first 10 fs of propagation, with a partial reflection back to the first excited state.

DMABN has also been added as an example of a TDDFT/AIMS calculation. TDDFT has been previously used to compute multiple spawning dynamics,[194,195] but this is the first time the nonadiabatic coupling calculation is completely circumvented. We show examples of interfaces with different electronic structure methods.

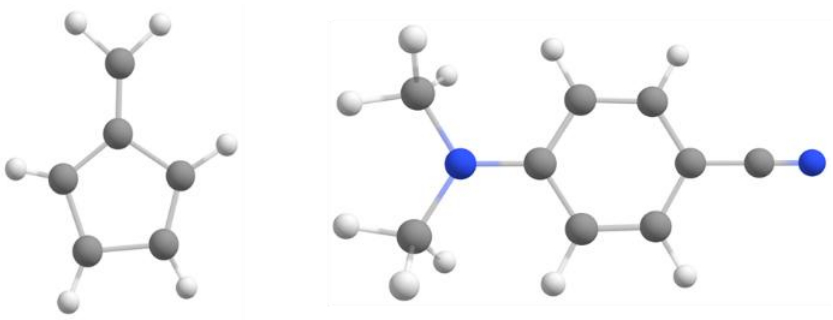

Figure 18 Molecular structures of Fulvene and DMABN.

4.4.1. Fulvene

We used two combinations of initial conditions and computed the S_1 population profile using both SA-2-CASSCF(6,6) and XMS-CASPT2 for each set, computing the ground and first excited states. The first collection of initial conditions, *null_KE*, is extracted from Ref[114], and contains 18 trajectories; the second collection contains the first 20 trajectories of Ref[128]. For both electronic structure methods, we used different sets of parameters to test the convergence of the simulation. In the *default set*, we used the coupling threshold of 0.01 $a.u.^{-1}$; the coupling used was the nonadiabatic coupling vector computed from the electronic structure calculation, and the momentum was corrected in the direction of the NAC at a spawn. The centroid was calculated using the BAT approximation. In the *thresh 0.015*, the coupling threshold was modified to 0.015 $a.u.^{-1}$. In the *tdba set*, the coupling was computed with the TDBA approximation, and the momentum corrected in the direction of the momentum. In the *momdir set*, the nonadiabatic coupling was calculated, but the momentum was corrected in the direction of the momentum. Finally, in the *thresh 0.005*, only the coupling threshold was modified to 0.005 $a.u.^{-1}$. This last set was used only in the CASPT2 dynamic. The plot of the S_1 population for all sets with both CASSCF and CASPT2 is shown in Figure 19.

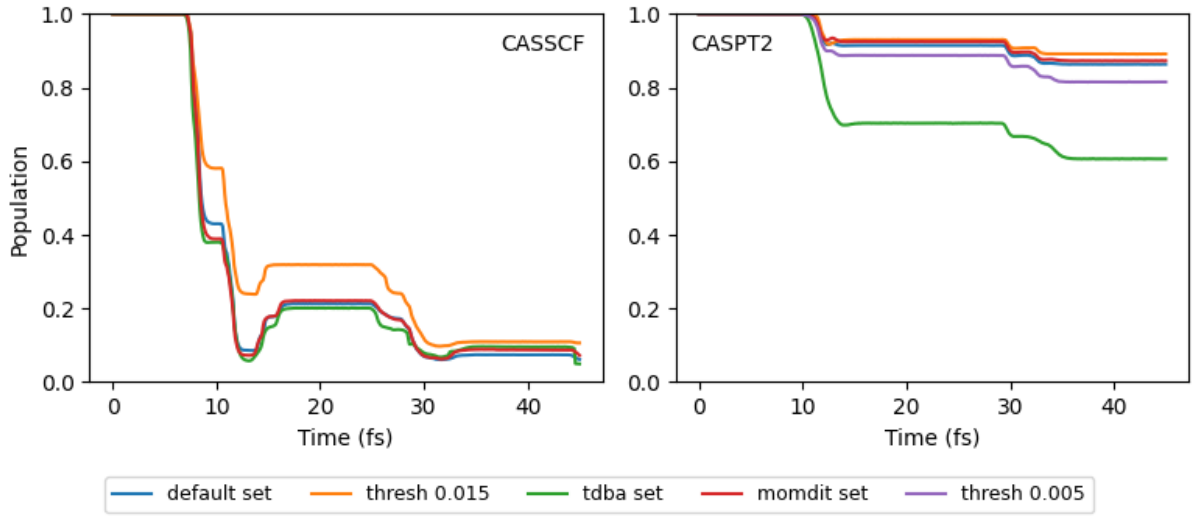

Figure 19 Population of the first excited state (S_1) for the fulvene dynamics with SA-2-CASSCF(6,6)/6-31g* and XMS-CASPT2, computed with Legion/OpenMolcas from the initial conditions presented in Ref[114], where the initial momentum is set to zero, *null_KE* and using different sets of parameters.

For CASSCF, almost all sets return the same population profile except for the high coupling threshold. In particular, we call attention to the *tdba set*, which is practically indistinguishable from the remaining sets. The profile matches both Ref[114] and Ref[154], which computed AIMS/CASSCF dynamics for fulvene using FMS90/Molpro and PySpawn/OpenMolcas, respectively, and used the same initial conditions.

For CASPT2, the population transferred to the ground state in the same time window is completely different. While in CASSCF, the S_1 population at 45 fs is around 6% for most sets, for CASPT2, the same population is close to 85% (Table 2). We can notice that the lower threshold of 0.005 leads to slightly more population transfer, and a threshold of 0.015 (used in Ref[154]) leads to an almost unnoticeable loss of transfer. The TDBA approximation overestimates the amount of population transferred to the S_0. The general trend of the populations also agrees with the dynamics in a recent pre-print interfacing the CASPT2 PySpawn/OpenMolcas.[154]

Table 2 Population of the first excited state (S_1) at time 45 fs for the fulvene dynamics with SA-2-CASSCF(6,6)/6-31g* and XMS-CASPT2, computed with Legion/OpenMolcas from the initial conditions presented in Ref[114], where the initial momentum is set to zero, *null_KE* and using different sets of parameters.

	CASSCF	CASPT2
default set	0.062	0.863
thresh 0.015	0.106	0.891
tdba set	0.050	0.606

momdir set	0.073	0.873
thresh 0.005	--	0.815

While the CASSCF results agree with previous publications using multiple spawning dynamics, they do not compare as well with surface hopping populations.[128] Also, the intensity of the difference between CASSCF and CASPT2 dynamics is surprising. Ref[154] explained this difference using static calculations and showed that the reaction path to the sloped conical intersection has a minimum in S_1 for CASPT2 that is not present, or not as intensely, in the PES with CASSCF. Although this could explain the difference, we wanted to test whether other aspects of the dynamics could be partially responsible. To evaluate this, we performed the same sets of dynamics with both CASSCF and CASPT2 using the first 20 trajectories previously used in surface hopping.[128] Both initial conditions were generated from a Wigner distribution, but the first collection of initial conditions had the initial velocity set to zero. This choice was made explicitly to favor the decay through the sloped conical intersection and probe the reflection mechanism in fulvene,[114] analogous to Tully model 3.[91] The second collection of initial conditions uses the velocity generated by the sampling without modification (Figure 20).

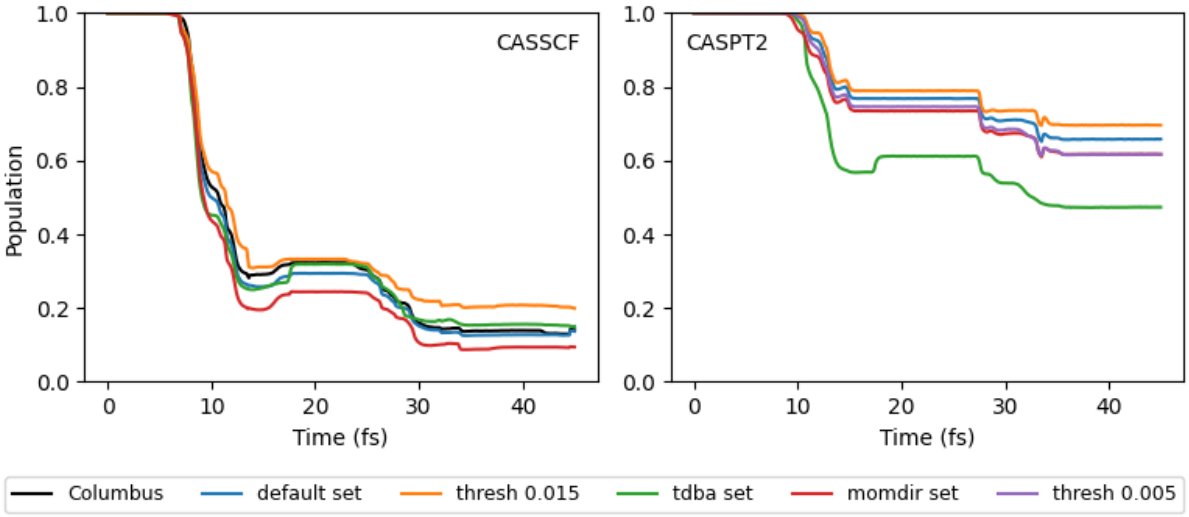

Figure 20 Population of the first excited state (S_1) for the fulvene dynamics with SA-2-CASSCF(6,6)/6-31g* and XMS-CASPT2, computed with Legion/OpenMolcas and Legion/Columbus from the initial conditions presented in Ref[128], where the initial momentum is not altered, *full_KE* and using different sets of parameters.

The CASSCF dynamics already show a difference when compared to the *null_KE* initial conditions, both in the actual population profile and in the fact that the different sets of dynamics cause a more noticeable impact. In this case, the higher threshold does not affect the population as much, and the TDBA approximation once again agrees very much with the dynamics using NAC. In this case, the momentum direction at spawning time leads to more population being transferred to the ground state, although the difference is small, 4% (Table 3). We performed an extra set of dynamics using the default parameters but using CASSCF implemented in

Columbus. This program was used in previous publications in the FSSH dynamics of fulvene and agrees with the Legion/OpenMolcas interface simulations.

For CASPT2, there is a noticeably less population in S_1 for all sets of parameters. Both the lower coupling threshold of 0.005 a.u.$^{-1}$ and the direction of momentum correction increase the amount of population being transferred to S_0. Similar to the previous CASPT2, the TDBA also overestimates the amount of population transfer.

Table 3 Population of the first excited state (S_1) at time 45 fs for the fulvene dynamics with SA-2-CASSCF(6,6)/6-31g* and XMS-CASPT2, computed with Legion/OpenMolcas and Legion/Columbus from the initial conditions presented in Ref[128], where the initial momentum is set to zero, *full_KE* and using different sets of parameters.

	CASSCF	CASPT2
default set	0.137	0.657
thresh 0.015	0.200	0.694
tdba set	0.150	0.474
momdir set	0.095	0.617
thresh 0.005	--	0.616
Columbus	0.141	

A comparison of the default parameters for the different initial conditions with CASSCF and CASPT2 is presented in Figure 21. We can see how the initial kinetic energy can be used to favor one decay pathway over the other. In the *null KE*, which favors the sloped conical intersection, the reflection of the CASSCF dynamics is strongly noticeable. At the same time, the CASPT2 dynamics, which has an S_1 minimum before the sloped intersection, has a significantly delayed decay time. In the *full KE*, on the other hand, the peaked conical intersection is expected to contribute to the relaxation mechanism. This is corroborated by the less pronounced reflection observed in the CASSCF calculation and the stronger population transfer in the CASPT2 dynamics, enabled by the peaked intersection that does not have an S_1 minimum.[154]

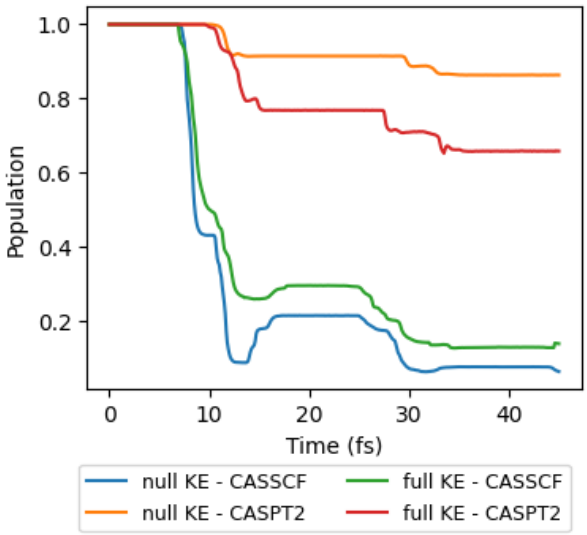

Figure 21 Population of the first excited state (S_1) for the fulvene dynamics with SA-2-CASSCF(6,6)/6-31g* and XMS-CASPT2, computed with Legion/OpenMolcas from the initial conditions presented in Ref[114] and Ref[128], the *null_KE* and *full_KE* initial conditions and for the default set of parameters.

Beyond the discussion of the molecular systems, it is worth focusing on the BAT approximation, which has been used in all calculations presented up until now. In Section 4.2.1, we presented the modified BAT approximation, BATE. Still, we chose to use the original approximation for the calculations presented here since this is the one established in the literature. Despite that, we can compare the S_1 population of fulvene when computed with the SPA approximation, BAT, and BATE, as shown in Figure 22. In all cases, the difference in population between SPA and the other methods is less than 1.5%. This is well within a tolerable error for the population, considering the speed-up provided by not needing to compute the centroid values. Particularly when noticing that this error is below 1% most of the time.

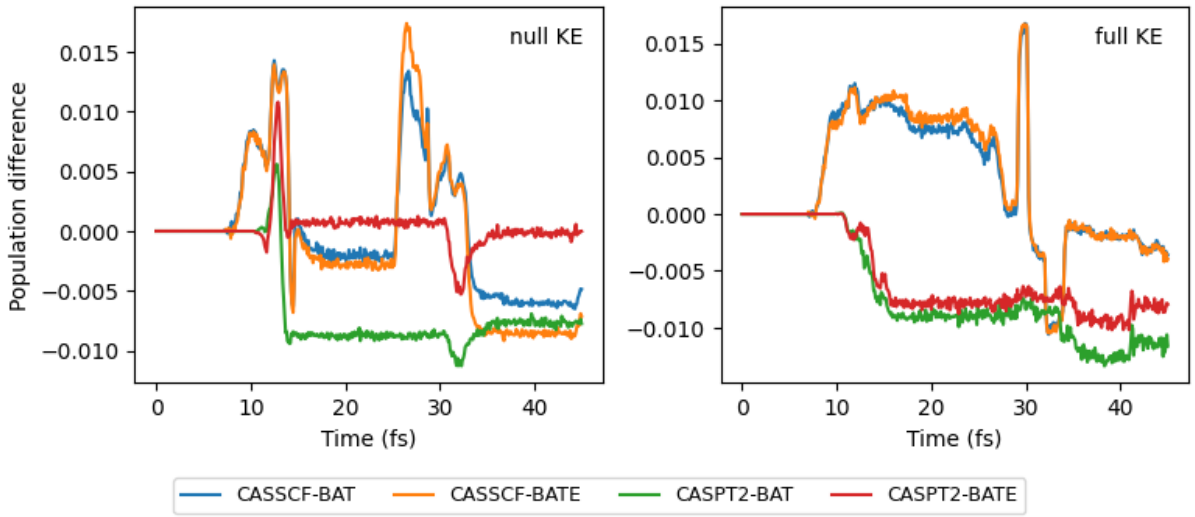

Figure 22 Difference between the S_1 population, computed as *SPA - BAT(E)* for the *null KE* and *full KE* collections of initial conditions, using default parameters, for dynamics using CASSCF and CASPT2 electronic structures.

When comparing the conventional BAT approximation and the newly suggested BATE, one can see that they can reproduce the SPA almost numerically. With both initial conditions, the difference between BAT and BATE is minimal for both CASSCF dynamics, but BAT is closer to the centroid dynamics. On the other hand, for the CASPT2 dynamics, BATE can approach the SPA population better. Particularly for the *null KE*, which has almost no population transfer, BATE reproduces almost exactly the SPA calculation. The improvements of BATE over BAT are marginal, but it shows that although the BAT approximation is already quite good, there is room for improvement if one considers the correct shape of the nonadiabatic coupling curve.

Another method used to speed up the calculation, the adaptive step, can be evaluated by comparing the population at different timestep sizes. Figure 23 has the difference between the reference calculation, where all steps taken are 0.1 fs. There is no data interpolation between steps, and the adaptive scheme, where the classical trajectory moves with a timestep of 0.5 fs outside the coupling region and 0.1 fs within, with the missing data being interpolated every 0.1 fs to propagate the coefficients. This scheme also has a difference below 1% with the reference, showing a good balance between error and efficiency, and can be modified with different step sizes and amounts of substeps.

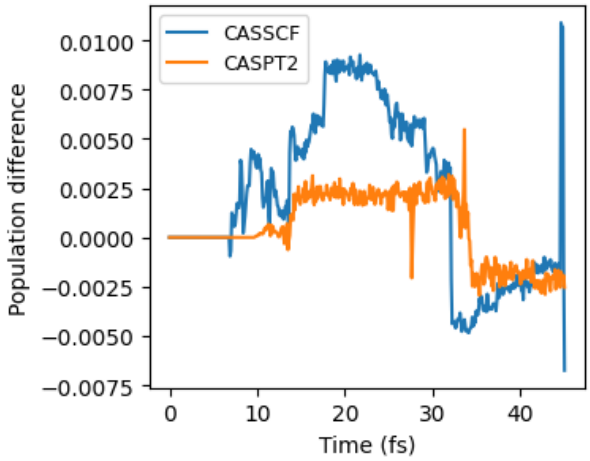

Figure 23 Population difference of S_1 between timesteps of 0.5 fs with 5 substeps vs timesteps of 0.1 fs without substeps. Computed for the *null KE* initial conditions with CASSCF and CASPT2 electronic structures.

Finally, we can look closer at the TDBA approximation to understand why it fails for CASPT2. Figure 24 contains the time derivative coupling for the same trajectory from the null KE initial conditions computed from the nonadiabatic coupling, with the formula

$$\sigma_{ij} = d_{ij} \cdot v\,, \tag{35}$$

and computed using TDBA. In CASSCF, where the coupling is high, TDBA can follow the general behavior of the time derivative coupling. It peaks at the same time, and the difference in sign does not seem to cause much of a problem with the coefficient integration. In CASPT2,

on the other hand, the coupling is considerably smaller. In this case, TDBA seems to overestimate the amount of coupling, consequently leading to more population transfer. This is taken as a representative case; the same is observed in the *full KE* sets of initial conditions.

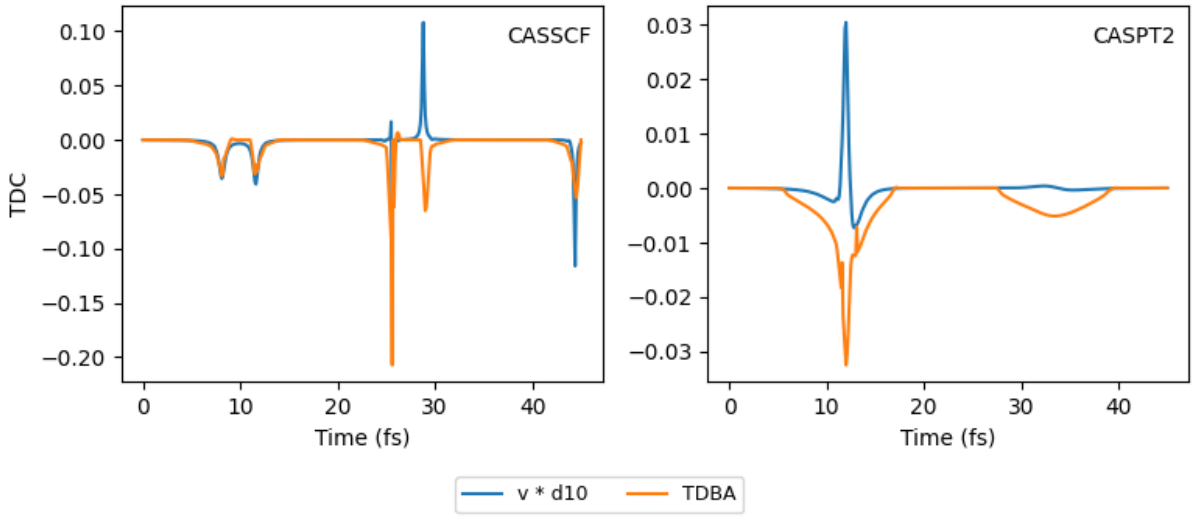

Figure 24 Time derivative coupling (TDC) between S_0 and S_1 computed with TDBA approximation and the dot product velocity (v) times nonadiabatic coupling (d_{10}) for a single trajectory from the *null KE* initial conditions computed with CASSCF and CASPT2 electronic structures.

4.4.2. DMABN

The interest in DMABN is because the PES of the first and second excited states meet multiple times along the dynamics, which causes S_1 and S_2 to keep exchanging populations. This sequence of avoided crossings is a good representation of the Tully model 2.[114]

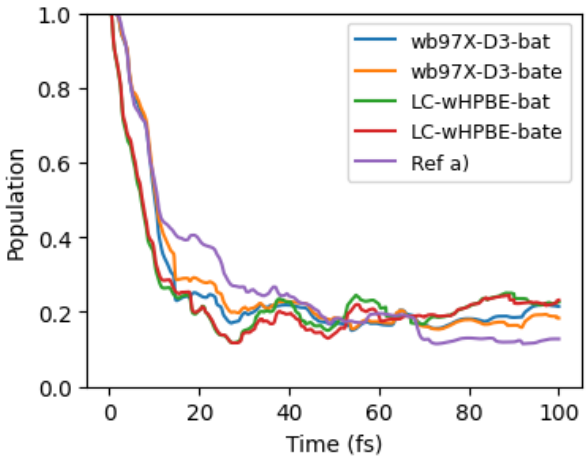

Figure 25 S_2 population for DMABN propagated with ωB97X-D3/def2-SV(P) in Legion/ORCA and LC-ωHPBE/6-31g in Legion/Gaussian. a) is Ref[114] LC-PBE/6-31g computeing NAC.

Figure 25 shows the population of the second excited state computed for DMABN using different TDDFT functionals (ωB97X-D3 and LC-ωHPBE) implemented on different electronic structure software. All calculations use the same set of parameters, except for the BAT and BATE approximations. The reference for comparison is available in the Supporting Information of Ref[114] and was propagated with LC-ωPBE implemented in TeraChem,[196–199] using the same coupling threshold as the calculations presented here, 0.005 a.u.$^{-1}$. TDBA causes the population to transfer more intensely within the first 20 fs of propagation. Afterward, the population oscillates around 0.2 in the S_2 state. Despite the variation, it agrees qualitatively with the reference.

A closer inspection of the time derivative coupling (Figure 26) indicates the repetitive interactions between S_1 and S_2, denoted by the peaks. An inspection of the TDC of fulvene shows the correlation between the high coupling in the CASSCF dynamics and a good approximation with TDBA, while the dynamics with a small coupling, CASPT2, have the TDC being overestimated. DMABN also shows a higher population transfer of 20% around 20 fs, the same intensity of the TDC as seen for the fulvene/CASPT2 dynamics. This shows that while TDBA can still return quantitatively correct results in some cases, this is not always reliable, and nonadiabatic coupling calculation is still required.[95] Still, even in those situations, TDBA seems to return at least a qualitatively good description of the dynamics. The trend observed here of higher TDC leading to better results could lead to tools to assess the quality of the TDBA in a given system without recurring comparison with a calculation that computes the nonadiabatic coupling. Future investigations are still necessary to establish general rules for this evaluation if this trend holds for other molecular systems, in which situation it holds, and if the values observed here are universal or system-specific.

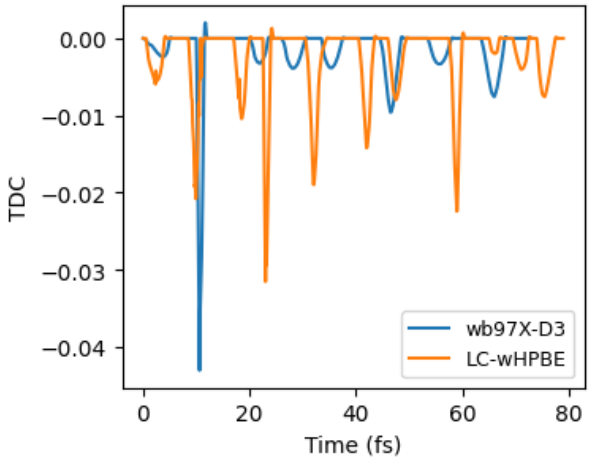

Figure 26 Time derivative coupling between states S_1 and S_2 for a single trajectory of DMABN computed with TDBA. Dynamics propagated with ωB97X-D3/def2-SV(P) in Legion/ORCA and LC-ωHPBE/6-31g in Legion/Gaussian.

4.5. Conclusion

We presented Legion, a computer program intended to facilitate the development of nonadiabatic mixed classical-quantum dynamics. The program is part of the Newton-X platform and inherits the interfaces to electronic structure programs already available for Newton-X. Legion is mostly written in Python3, a flexible language that allows for modular code, where tasks run independently. This makes it easy to reuse code in different sections and switch between modules to use different dynamics methods and approximations. Although the computationally expensive part of the dynamics is usually the electronic structure calculation, Legion uses modules written in Fortran for the mathematical operations, such as building the Hamiltonian for the coefficient propagation. Beyond the Fortran module, Legion also employs strategies like adaptive timestep for classical propagation, parallel trajectory propagation, and avoiding computation of the centroid.

We have detailed the code's structure and the implementation of a conventional AIMS method. We have also presented a modification for the BAT approximation, which, although only marginally improved over the original, shows that there is still room to improve in BAT. We also took a new approximation developed for surface hopping calculations, TDBA. We implemented it for the first time in the context of multiple spawning, allowing dynamics propagation with any electronic structure method.

In the validation of the software, we showed the dynamics for DMABN, completely avoiding the computation of nonadiabatic coupling vectors. We also performed a series of dynamics with fulvene, varying some of the multiple spawning parameters and complementing the discussion presented in the literature. We saw how the choice of initial condition is related to the different population profiles observed from dynamics with CASSCF and CASPT2 since the initial condition can increase the relevance of specific relaxation paths.

While we showed that, in some cases, the TDBA approximation works as well as NAC dynamics, we also saw examples where it overestimates the population transfer. However, we lack tools to evaluate whether TDBA will be a good approximation for a given system. Still, even in cases where the approximation does not agree numerically with the reference, the dynamics seem to be able to recover the qualitative behavior of the system. The computation of the time derivative coupling using overlap is becoming routine in both surface hopping and multiple spawning methods, and this is currently being implemented in Legion.

5. Extra contributions

During my PhD, I made contributions to different works produced in our group that were not directly connected to the thesis but were relevant to my formation and the topics discussed here. In this section, I will give a short description of them.

5.1. Recommendations for velocity adjustment in surface hopping

This section reports the results of the following publication:

J. M. Toldo, R. S. Mattos, M. Pinheiro, Jr., S. Mukherjee, M. Barbatti, **Recommendations for Velocity Adjustment in Surface Hopping**, J. Chem. Theory Comput. **20**, 614 (2024). DOI: 10.1021/acs.jctc.3c01159

In this paper,[128] we investigated some of the approximations necessary for surface hopping, as discussed in Section 2.1, namely the kinetic energy correction and the direction of rescaling at hopping to conserve total energy.

As mentioned in Section 2.1, when there is a hop in the system, the momentum has to be scaled to ensure energy conservation. This correction should be an impulse in the direction of the nonadiabatic coupling, such that the difference in kinetic energy equilibrates the difference in potential energy due to hopping. When the hop is towards a more energetic state, there might not be enough kinetic energy, causing a frustrated hop. The procedure becomes more dubious in the case of unavailability of the nonadiabatic coupling vectors between the electronic states.

In its absence, the usual direction for the correction is either the direction of the difference of gradients of the states involved in the hopping or the direction of momentum. The former is justified by a theoretical basis[71] but involves the computation of an extra gradient; the latter is the least recommended but still used due to lower computational cost. The problem with using the momentum direction for the correction is that it overestimates the available kinetic energy when hopping up, which leads to an artificial population transfer to the higher excited state. In the paper, we discuss, for two systems using CASSCF dynamics, how the choice of direction can influence the dynamics and how this effect could be correlated to the potential energy surfaces around the conical intersection. We also propose a scaling method for rescaling the

kinetic energy during the hopping evaluation to account for the overestimation in the direction of the momentum.

My contribution to this project was to evaluate the validity of two strategies to approximate the nonadiabatic coupling vector, taking fulvene as the system of interest. The first one is based on the work of Shu *et al.*,[139] who proposed a method, the curvature-driven NAC, to approximate the nonadiabatic coupling vector (***G***$_{IJ}$) only from information on the energies and their gradients, as in:

$$\mathbf{G}_{IJ} = \mathbf{g}_{IJ} + \alpha \dot{\mathbf{R}}. \tag{36}$$

Where:

$$\mathbf{g}_{IJ} = \frac{\partial V_I}{\partial \mathbf{R}} - \frac{\partial V_J}{\partial \mathbf{R}},$$
$$\alpha = \frac{\sigma_{IJ} - \dot{\mathbf{R}}.\mathbf{g}_{IJ}}{\dot{\mathbf{R}}.\dot{\mathbf{R}}}. \tag{37}$$

They justify calling ***G***$_{IJ}$ the effective nonadiabatic coupling vector because, when multiplied with the velocity, it will return the time derivative coupling by construction:

$$\dot{\mathbf{R}}.\mathbf{G}_{IJ} = \sigma_{IJ} \tag{38}$$

The other approximation for the nonadiabatic coupling is to use the actual vector computed by a semi-empirical method, FOMO-CI.[200] Despite being an extra calculation, we wanted to see how this approximation would behave, given how little computation time the semi-empirical methods cost.

We discussed the final effect of the different approximations on the average population, but I also compared the exact coupling vector with those two approximations. For the curvature-driven coupling (***G***$_{IJ}$), I opened the components of the approximation to see how they compare with the exact coupling vector and the gradient difference, which is used to compute ***G***$_{IJ}$.

We showed how the velocity and gradient difference compare with NAC for a single trajectory. Both, as well as ***G***, remain almost perpendicular to the coupling for the entirety of the trajectory run. Comparing the angle of ***G*** with the gradient difference (***g***) shows that ***G*** oscillates following the direction of ***g***. The curvature-driven coupling vector simply reproduces the direction of g, except in the regions with stronger coupling. A comparison between the angle of ***G*** and NAC shows that the two vectors are, for all purposes, pointing at random directions, ***G*** does not follow NAC.

The same comparison of the angle between the NAC computed by the CASSCF calculation and the semi-empirical FOMO-CI method shows that they point in similar directions, but the FOMO-CI is much faster to perform.

We concluded that the kinetic energy rescaling proposed in the paper can improve the results in general and should be employed when correcting momentum in the direction of momentum. Curvature-driven coupling should fare no better than correcting in the direction of the gradient difference. Also, the use of a semi-empirical method to compute the coupling vector shows potential and could lead to further developments.

5.2. Prediction challenge: Cyclobutanone dynamics with different electronic structure methods

This section reports the discussion of the following publication:

S. Mukherjee, R. S. Mattos, J. M. Toldo, H. Lischka, M. Barbatti, **Prediction Challenge: Simulating Rydberg photoexcited cyclobutanone with surface hopping dynamics based on different electronic structure methods**, J. Chem. Phys. **160**, 154306 (2024). DOI: 10.1063/5.0203636

This work[51] was part of an open challenge to predict the nonadiabatic dynamics of cyclobutanone after excitation into the second excited state, which has a Rydberg character. The theoretical groups were given instructions for a future experiment on cyclobutanone. They were invited to attempt to predict the signal that would be measured in the experiment, which is related both to the lifetime of the excited state and to the possible reaction paths it can take. Multiple groups accepted this challenge, which is an example of the large variety of nonadiabatic dynamics methods found in the literature and the large number of electronic structure methods used in those dynamics.

We performed four sets of dynamics, changing the electronic structure methods and the approximations. Set 1 used the multiconfigurational self-consistent field (MCSCF) electronic structure, using the exact NACV; set 2 used the same electronic structure method, but instead of computing NACV, we used the Baeck-An approximation to compute the time derivative coupling, TDBA (Section 2.3.1); set 3 used TDDFT/CAM-B3LYP,[201] also using TDBA to approximate the coupling; and set 4 used the semi-empirical ODM3 method[202] as a basis for a multireference configuration interaction (MRCI) calculation that also computes the NACV. The method chosen for sets 1 and 2 can become increasingly costly as one adds more orbitals to the active space. Given the uncertainty of the total time of the dynamics, we chose to build the active space as a product of smaller sub-spaces. It describes the relevant excitations for the states of interest and gives flexibility to the molecule, allowing bond braking and geometrical

modifications during the dynamics. Since most orbitals are not interacting with one another, they only interact within their subspaces. The combination of orbitals and occupations does not rise as usual for MCSCF, and the single-point calculation was fast enough to allow the dynamics to run for approximately 10 ps.

In the end, we obtained widely different lifetimes for the different electronic structures. Sets 1 and 2 returned an estimated lifetime of 9.0 ps and 10.4 ps, respectively. Set 3 estimated a lifetime of 0.4 ps and set 4 a lifetime of 0.04 ps. Similarly, the different sets also point at different reaction paths as being the most relevant to the dynamics. An extended table at the end of Ref[51] contains a summary of the lifetimes and dominant mechanisms for all publications present in the challenge, and the lifetimes are reproduced in Figure 27. It shows that there is no general agreement between methods, either in reaction paths or lifetimes. The experimental results have not been published yet, so we cannot tell which predictions were right and which were wrong, but it already tells us that we as a community are still unable to make predictions of experiments and detect the mistakes from within the theory without comparing them to the experiments.

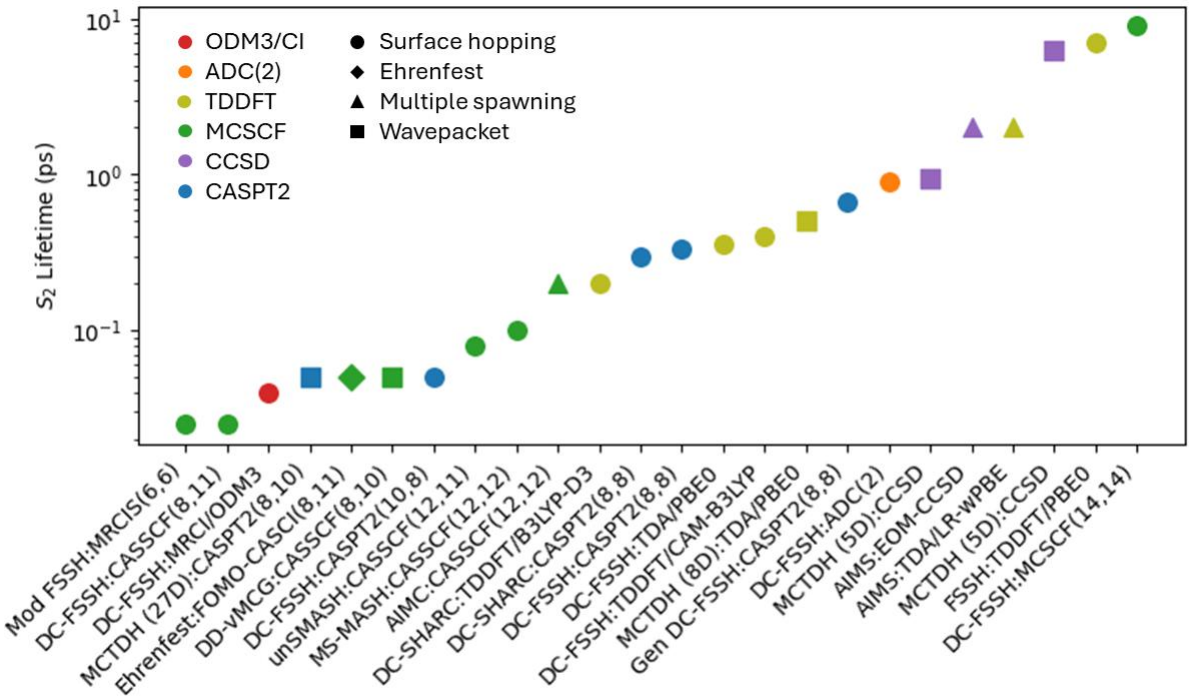

Figure 27 S_2 lifetime of cyclobutanone for all nonadiabatic dynamics and electronic structure methods used in the prediction challenge.

My contributions to this project were to monitor and analyze the dynamics of Set 2 and generate the plot of the probability distribution function for all sets, which will be compared with experiments. Despite the overall message, there is one silver lining regarding the TDBA approximation. We showed that even for a long timescale with significantly large energy gaps between states (up to around 2 eV), TDBA is still capable of reproducing the correct hops,

agreeing with the NACV dynamics in both lifetime and reaction paths. The combination of all the works shows not only how many variations of nonadiabatic dynamics methods are currently being developed but also how important it is to be able to use the largest possible number of methods for them, which is possible in Legion. It also reinforces the need for methods to verify the results, as in QDCT.

5.3. Long time scale dynamics

This section reports the discussion that will give rise to the following publication:

S. Mukherjee, Y. Lassmann, R. S. Mattos, B. Demoulin, B. F. E. Curchod, M. Barbatti, **Assessing Nonadiabatic Dynamics Methods in Long Timescales**, (2024). In preparation.

In this work, we evaluate how different methods fare when used to simulate phenomena happening in a long time scale. Due to computational limitations, the methods for nonadiabatic dynamics were used to simulate photo-relaxation happening in an ultrafast regime, up to a few picoseconds. Recent developments in semi-empirical methods[172,174,200] and machine learning potentials[143,163] are making the propagation of hundreds of thousands of timesteps a feasible process, but the current nonadiabatic dynamics methods have not been tested for such long propagation.

We compared the convergency, efficiency, and practical aspects of using MCTDH, ML-MCTDH, AIMS, and FSSH to propagate an analytical 10-dimensional SBH model up to 100 fs. Due to the independent trajectories and the newly developed Newton-X NS, FSSH calculations could be performed very efficiently in a matter of hours and without modification to the code. For AIMS, the particularities of the weakly coupled PES required the development of local changes in the method, which continuously spawned new trajectories.[203] This causes an uncontrollable increase in the size of the nuclear basis set and requires an aggressive trajectory elimination scheme, the cannibalistic stochastic selection approach of AIMS (CSS-AIMS).[120,147] Different from the other methods, in MCTDH and ML-MCTDH, the propagation of the dynamics is the computationally expensive part of the method, not the electronic structure calculation. Due to that, the comparison of the methods could also be performed only up until 50 ps. The implementation of those methods was not intended to be used for such a long timescale, so the data analysis can be problematic due to software limitations.

Despite the different levels of approximations on those families of methods, they generally agree on the decay lifetime and population profile. CCS-AIMS seems to be a particularly good match with converged MCTDH and ML-MCTDH. The convergency tests suggest that the

results are still reliable, and the biggest problem seems to be the software structure, which is not prepared to deal with such a large amount of data.

When I arrived, the project was already in development, and my contributions were mostly in the discussions rather than actually running the simulations.

5.4. Gravitationally-induced wave function collapse

This section reports the discussion of the following publication:

A. Tomaz, R. S. Mattos, M. Barbatti, **Gravitationally-induced Wave Function Collapse Time for Molecules**, Phys. Chem. Chem. Phys. **26**, 20785 (2024). DOI: 10.1039/D4CP02364A

Here,[165] we investigate the Diósi-Penrose proposition that the wave function collapse is caused by the instability of coexisting gravitational collapse systems in different geometric conformations.[204–207] We study how this could be applied to molecular systems and develop the equations necessary to compute the collapse time. We then used the proposed equation to estimate the collapse time of systems of varying scales and suggested an experimental setup to test the original hypothesis.

Superposition is a staple in the quantum realm, but when we transition to the classical scale, we are always restricted to the observation of definite results. In this transition from quantum to classical, some phenomena need to occur that are not entirely understood. A good part of this can be explained by decoherence effects.[153] Decoherence is the delocalization of the coherence of a subsystem over the environment entangled with it.[165] It is a general phenomenon, but its reflection in nonadiabatic dynamics can be seen in the decoherence-corrected surface hopping methods.[109,110] After decoherence, the subsystem can still be left in an improper mixture, and it may still be observed in one of its possible states. The collapse is responsible for bringing the system to be well-defined in a single one of its states, but how it does that (or even if the collapse actually happens) is still an open question.

The Diósi-Penrose model assumes that gravity causes the collapse of the quantum superposition. When a system is in a superposition of quantum states that present different geometrical conformations, they generate mismatching gravitational potential, which causes instabilities and leads to collapse. Within this model, the time constant of the collapse is inversely proportional to the gravitational self-energy of the difference between the two superposed states, based on the Heisenberg time-energy uncertainty principle.[207]

To test this assumption, we present a series of equations to compute the gravitational self-energy under different levels of approximation, which allow us to make predictions for systems as small as the ammonia molecule and as big as a small dog. We start by supposing that the molecular nuclei will follow a Gaussian mass distribution and obtain an equation for the energy of small systems. This involves the pair-wise distance for all atoms of the system. To be able to apply the model to larger systems, we also develop an alternative equation for a homogeneous or identical nucleus. We conclude with an even simple equation for the case where the displacement distance between the different states superposed is considerably smaller than the scale of the system. We test the validity of those approximations for the fullerene C_{70} and use them to predict the collapse time for systems of different scales, from quantum to macro.

This project's topic is on a much more fundamental level than usual, but the hypothesis of the Diósi-Penrose model has not been proved, and it is not the only model to explain the collapse.[208] To address this, we also propose an experimental setup using a Talbot-Lau interferometer to measure a system's collapse time. This could then be compared to the predicted values to validate or disprove the current assumptions of the model.

During my PhD, I developed an interest in phenomena involving decoherence and collapse. When I heard of the project, I was curious if it could help in understanding collapse and if it could eventually be applied to dynamics. My contribution to the project was restricted to discussions and minor modifications to the code used to compute the decoherence time of the molecular systems. In particular, my experience developing QDCT and Legion helped to clarify formal aspects of the derivation of the gravitational self-energy.

5.5. Unsupervised Learning of Molecular Dynamics

This section reports the discussion of the following publication:

M. Pinheiro Jr, M. de O. Bispo, B. C. Garain, R. S. Mattos, M. T. do Casal, J. M. Toldo, S. Mukherjee, M. Barbatti, **ULaMDyn: Enhancing Excited-State Dynamics Analysis Through Streamlined Unsupervised Learning**, (2024). In preparation.

In this work, we present ULaMDyn (Unsupervised Learning of Molecular Dynamics), an open-source Python package for automating the analysis of high-dimensional molecular dynamics data. In trajectory surface hopping, we propagate multiple trajectories, usually in the order of a hundred, to study the behavior of molecular systems when photoexcited. After propagation, it is necessary to make a statistical analysis of the generated data to extract

important insights into the dynamic features, and ULaMDyn helps to identify and extract those features.

The properties obtained from the dynamics can be straightforward to analyze, such as the average population of each electronic state, that can be used to compute the excited-state lifetime. However, they can also increase in complexity with the system size and propagation time, such as characterizing geometries at hopping time and isolating the most important molecular motions of the possible reaction channels. In the latter, automatic methods of pattern recognition can speed up the analysis work and possibly even detect unexpected relations that would go unnoticed in the most complicated systems.

In ULaMDyn, the data generated from the dynamics is aggregated in a single place and can be freely explored by the user, allowing one to identify patterns in the data. Beyond that, the package also contains a set of unsupervised machine learning methods that can be classified as *dimensionality reduction* and *clustering*. In the dimensionality reduction schemes, the machine will reduce the complexity of the high-dimensional datasets by mapping them to lower-dimensional spaces. It reduces the number of variables to be analyzed while preserving the essential information. The clustering techniques take the entirety of the data points and find shared attributes among the points. Those patterns can be, for instance, geometries with similar electronic properties or nuclear conformation, which is essential in identifying the reaction pathways.

ULaMDyn was developed for surface hopping and is seamlessly interfaced with Newton-X, both CS and NS. Future plans include extending the interface to Legion and QDCT, and modifying ULaMDyn to treat also multiple spawning dynamics. Most of the information generated by the dynamics is the same and originates from the classical trajectories. While surface hopping has the hopping geometries that are characteristic of the crossing regions, multiple spawning has the spawning points with similar information. The biggest difference is adding information on the coefficients of the classical trajectories, exclusive for AIMS, and its use to compute the expectation values.

My contribution to this project mainly consisted of testing the interface of ULaMDyn to Newton-X and the user experience, with minor contributions to the code on the same aspects. I will also be responsible for extending its usability to include multiple spawning methods.

Conclusions

This thesis presented developments based on frozen Gaussian wavepacket propagation to perform and correct nonadiabatic mixed quantum-classical dynamics. We showed how NA-MQC methods, in collaboration with experiments, can help us study molecular systems with multiple applications. We also showed how those methods can fail without proper tools to assess their quality.

In Chapter 3. we used the Gaussian wavepacket methods to perform a post-processing analysis in surface hopping trajectories. We present a novel scheme to use the pre-computed classical trajectories to build the Gaussian wavepacket and propagate the coefficients, reproducing AIMS dynamics. This tool can be used to assess the quality of the surface hopping dynamics at the cost of running an analytical model.

We validate the method using a series of one-dimensional analytical models and a 12-dimensional SBH model. Treating multidimensional systems is only possible with the addition of interpolated trajectories, a method developed in this thesis, to artificially increase the nuclear basis set and simulate a spawning procedure.

In Chapter 4. , we presented Legion, a software for running and developing Gaussian wavepacket propagation methods. This chapter, together with Chapter 2. , presented the working equation and method description of *ab initio* multiple spawning, which is implemented in Legion. Since the program is created under the umbrella of the Newton-X platform, it inherits a large collection of electronic structure interfaces.

We also used Legion to investigate the dynamics of fulvene and showed how the initial condition could favor the relaxation mechanism of a sloped conical intersection. This discussion is centered around the variation of the kinetic energy in the initial condition and the difference in the potential energy surface for CASSCF and CASPT2 methods. Legion was also used to perform DMABN dynamics, completely avoiding the computation of the nonadiabatic coupling but still recovering the population profile available in the literature.

We extended the AIMS equations of motion to support the computation of the time derivative coupling without requiring the nonadiabatic coupling from the electronic structure. We also, for the first time, applied the time derivative Baeck-An method to compute the TDC and showed this approximation can be as good as in surface hopping. Moreover, we proposed criteria to estimate the validity of the TDBA approximation for a given system by the maximum intensity of the TDC. This should be tested further to see if it holds, in general, beyond the two systems studied here. The multiple spawning equations using the time derivative coupling can

also be added to QDCT since many electronic structure methods conventionally used in surface hopping do not produce the nonadiabatic coupling. The derivative could be computed from scratch using TDBA or, preferably, read from the dynamics.

Frequently, a particular molecular system is only adequately described by a few electronic structure methods,[56] so it is crucial to have the largest diversity of methods available to perform dynamics. Legion addresses this point, as well as the lack of open-source, easily available, and efficient multiple spawning software. On the other hand, QDCT is a tool to assess the quality of surface hopping dynamics. It performs a propagation of the nuclear wavepacket and is independent of the *ad hoc* approximation intrinsic to surface hopping.

Legion now contains the structure necessary to propagate dynamics, but we are planning the following steps to extend the tools available in the package. Our current focus, after implementing the overlap methods to compute the time derivative coupling, will be on the train of trajectories[104,141] and a recently proposed variational propagator for a linearly dependent moving basis.[164] The former is a computationally inexpensive way of increasing the nuclear basis by adding different points in time of the same classical trajectory to the basis. It allows trajectory communication in a larger range of the phase space. The latter is an alternative way of computing the trajectory coefficients that deals with a known problem of frozen Gaussian propagation methods: energy conservation.[154–156] Those two will also be added to QDCT once they have been tested in Legion.

Now that we can compute and control the multiple spawning dynamics with various electronic structure methods, we can create reference calculations and test QDCT extensively for real molecules. The post-processing in QDCT deals with the decoherence effect independent of the original treatment in surface hopping. Comparing the dynamics before and after this treatment can also help identify systems where the current decoherence correction methods fail, as in some of the unidimensional Tully models, and develop better corrections.

Lastly, the tools of automatic data analysis of Ulamdyn can be extended to multiple spawning, allowing it to be used for treating Legion and QDCT output.

Bibliography

(1) Goulet-Hanssens, A.; Eisenreich, F.; Hecht, S. Enlightening Materials with Photoswitches. *Adv. Mater.* **2020**, *32* (20), 1905966. https://doi.org/10.1002/adma.201905966.

(2) Vallance, C.; Orr-Ewing, A. J. Virtual Issue on Photodissociation: From Fundamental Dynamics and Spectroscopy to Photochemistry in Planetary Atmospheres and in Space. *J. Phys. Chem. A* **2023**, *127* (28), 5767–5771. https://doi.org/10.1021/acs.jpca.3c03975.

(3) Alexandrova, A. N.; Tully, J. C.; Granucci, G. Photochemistry of DNA Fragments via Semiclassical Nonadiabatic Dynamics. *J. Phys. Chem. B* **2010**, *114* (37), 12116–12128. https://doi.org/10.1021/jp103322c.

(4) Canuel, C.; Mons, M.; Piuzzi, F.; Tardivel, B.; Dimicoli, I.; Elhanine, M. Excited States Dynamics of DNA and RNA Bases: Characterization of a Stepwise Deactivation Pathway in the Gas Phase. *J. Chem. Phys.* **2005**, *122* (7). https://doi.org/10.1063/1.1850469.

(5) Borges, I.; Uhl, E.; Modesto-Costa, L.; Aquino, A. J. A.; Lischka, H. Insight into the Excited State Electronic and Structural Properties of the Organic Photovoltaic Donor Polymer Poly(Thieno[3,4-b]Thiophene Benzodithiophene) by Means of Ab Initio and Density Functional Theory. *J. Phys. Chem. C* **2016**, *120* (38), 21818–21826. https://doi.org/10.1021/acs.jpcc.6b07689.

(6) Modesto-Costa, L.; Borges, I.; Aquino, A. J. A.; Lischka, H. Electronic Structure Theory Gives Insights into the Higher Efficiency of the PTB Electron-Donor Polymers for Organic Photovoltaics in Comparison with Prototypical P3HT. *J. Chem. Phys.* **2018**, *149* (18). https://doi.org/10.1063/1.5054919.

(7) do Casal, M. T.; Veys, K.; Bousquet, M. H. E.; Escudero, D.; Jacquemin, D. First-Principles Calculations of Excited-State Decay Rate Constants in Organic Fluorophores. *J. Phys. Chem. A* **2023**, *127* (48), 10033–10053. https://doi.org/10.1021/acs.jpca.3c06191.

(8) *Quantum Chemistry and Dynamics of Excited States: Methods and Applications*; González, L., Lindh, R., Eds.; Wiley: Hoboken, NJ, 2021.

(9) Improta, R.; Santoro, F.; Blancafort, L. Quantum Mechanical Studies on the Photophysics and the Photochemistry of Nucleic Acids and Nucleobases. *Chem. Rev.* **2016**, *116* (6), 3540–3593. https://doi.org/10.1021/acs.chemrev.5b00444.

(10) Arpa, E. M.; Brister, M. M.; Hoehn, S. J.; Crespo-Hernández, C. E.; Corral, I. On the Origin of the Photostability of DNA and RNA Monomers: Excited State Relaxation Mechanism of the Pyrimidine Chromophore. *J. Phys. Chem. Lett.* **2020**. https://doi.org/10.1021/acs.jpclett.0c00935.

(11) Barbatti, M.; Aquino, A. J. A. A.; Szymczak, J. J.; Nachtigallová, D.; Hobza, P.; Lischka, H.; Nachtigallova, D.; Hobza, P.; Lischka, H. Relaxation Mechanisms of UV-Photoexcited DNA and RNA Nucleobases. *Proc. Natl. Acad. Sci.* **2010**, *107* (50), 21453–21458. https://doi.org/10.1073/pnas.1014982107.

(12) Barbatti, M.; Szymczak, J. J.; Aquino, A. J. A.; Nachtigallov, D.; Lischka, H. The Decay Mechanism of Photoexcited Guanine - A Nonadiabatic Dynamics Study. *J. Chem. Phys.* **2011**, *134* (1). https://doi.org/10.1063/1.3521498.

(13) Beckstead, A. A.; Zhang, Y.; De Vries, M. S.; Kohler, B. Life in the Light: Nucleic Acid Photoproperties as a Legacy of Chemical Evolution. *Phys. Chem. Chem. Phys.* **2016**, *18* (35), 24228–24238. https://doi.org/10.1039/c6cp04230a.
(14) Serrano-Andrés, L.; Merchán, M. Are the Five Natural DNA/RNA Base Monomers a Good Choice from Natural Selection?. A Photochemical Perspective. *J. Photochem. Photobiol. C Photochem. Rev.* **2009**, *10* (1), 21–32. https://doi.org/10.1016/j.jphotochemrev.2008.12.001.
(15) Narayanan, D. L.; Saladi, R. N.; Fox, J. L. Ultraviolet Radiation and Skin Cancer. *Int. J. Dermatol.* **2010**, *49* (9), 978–986. https://doi.org/10.1111/j.1365-4632.2010.04474.x.
(16) Barbatti, M.; Lischka, H. Nonadiabatic Deactivation of 9H-Adenine: A Comprehensive Picture Based on Mixed Quantum-Classical Dynamics. *J. Am. Chem. Soc.* **2008**, *130* (21), 6831–6839. https://doi.org/10.1021/ja800589p.
(17) Crespo-Hernández, C. E.; Cohen, B.; Hare, P. M.; Kohler, B. Ultrafast Excited-State Dynamics in Nucleic Acids. *Chem. Rev.* **2004**, *104* (614), 1977–2020. https://doi.org/10.1021/cr0206770.
(18) Hudock, H. R.; Levine, B. G.; Thompson, A. L.; Satzger, H.; Townsend, D.; Gador, N.; Ullrich, S.; Stolow, A.; Martínez, T. J. Ab Initio Molecular Dynamics and Time-Resolved Photoelectron Spectroscopy of Electronically Excited Uracil and Thymine. *J. Phys. Chem. A* **2007**, *111* (34), 8500–8508. https://doi.org/10.1021/jp0723665.
(19) Lan, Z.; Fabiano, E.; Thiel, W. Photoinduced Nonadiabatic Dynamics of 9H-Guanine. *Chemphyschem Eur. J. Chem. Phys. Phys. Chem.* **2009**, *10* (8), 1225–1229. https://doi.org/10.1002/cphc.200900030.
(20) Markwick, P. R. L.; Doltsinis, N. L. Ultrafast Repair of Irradiated DNA: Nonadiabatic Ab Initio Simulations of the Guanine-Cytosine Photocycle. *J. Chem. Phys.* **2007**, *126* (17), 1–7. https://doi.org/10.1063/1.2728897.
(21) Pecourt, J. M. L.; Peon, J.; Kohler, B. DNA Excited-State Dynamics: Ultrafast Internal Conversion and Vibrational Cooling in a Series of Nucleosides. *J. Am. Chem. Soc.* **2001**, *123* (42), 10370–10378. https://doi.org/10.1021/ja0161453.
(22) Hirao, I. Unnatural Base Pair Systems for DNA/RNA-Based Biotechnology. *Curr. Opin. Chem. Biol.* **2006**, *10* (6), 622–627. https://doi.org/10.1016/j.cbpa.2006.09.021.
(23) Hirao, I. Unnatural Base Pair Systems toward the Expansion of the Genetic Alphabet in the Central Dogma. *Proc Jpn Acad Ser B* **2012**, *88* (7), 345.
(24) Lee, K. H.; Hamashima, K.; Kimoto, M.; Hirao, I. Genetic Alphabet Expansion Biotechnology by Creating Unnatural Base Pairs. *Curr. Opin. Biotechnol.* **2018**, *51* (Figure 1), 8–15. https://doi.org/10.1016/j.copbio.2017.09.006.
(25) Malyshev, D. A.; Romesberg, F. E. The Expanded Genetic Alphabet. *Angew. Chem. - Int. Ed.* **2015**, *54* (41), 11930–11944. https://doi.org/10.1002/anie.201502890.
(26) Matarazzo, A.; Hudson, R. H. E. Fluorescent Adenosine Analogs: A Comprehensive Survey. *Tetrahedron* **2015**, *71* (11), 1627–1657. https://doi.org/10.1016/j.tet.2014.12.066.
(27) Ashwood, B.; Pollum, M.; Crespo-Hernández, C. E. Photochemical and Photodynamical Properties of Sulfur-Substituted Nucleic Acid Bases,. *Photochem. Photobiol.* **2019**, *95* (1), 33–58. https://doi.org/10.1111/php.12975.
(28) Xu, W.; Chan, K. M.; Kool, E. T. Fluorescent Nucleobases as Tools for Studying DNA and RNA. *Nat. Chem.* **2017**, *9* (11), 1043–1055. https://doi.org/10.1038/NCHEM.2859.

(29) Hamashima, K.; Kimoto, M.; Hirao, I. Creation of Unnatural Base Pairs for Genetic Alphabet Expansion toward Synthetic Xenobiology. *Curr. Opin. Chem. Biol.* **2018**, *46*, 108–114. https://doi.org/10.1016/j.cbpa.2018.07.017.
(30) Hirao, I.; Ohtsuki, T.; Fujiwara, T.; Mitsui, T.; Yokogawa, T.; Okuni, T.; Nakayama, H.; Takio, K.; Yabuki, T.; Kigawa, T.; Kodama, K.; Yokogawa, T.; Nishikawa, K.; Yokoyama, S. An Unnatural Base Pair for Incorporating Amino Acid Analogs into Proteins. **2002**, *20* (February), 177–182.
(31) Boulton, M.; Różanowska, M.; Różanowski, B. Retinal Photodamage. *J. Photochem. Photobiol. B* **2001**, *64* (2), 144–161. https://doi.org/10.1016/S1011-1344(01)00227-5.
(32) Huntress, M. M.; Gozem, S.; Malley, K. R.; Jailaubekov, A. E.; Vasileiou, C.; Vengris, M.; Geiger, J. H.; Borhan, B.; Schapiro, I.; Larsen, D. S.; Olivucci, M. Toward an Understanding of the Retinal Chromophore in Rhodopsin Mimics. *J. Phys. Chem. B* **2013**, *117* (35), 10053–10070. https://doi.org/10.1021/jp305935t.
(33) Manathunga, M.; Yang, X.; Luk, H. L.; Gozem, S.; Frutos, L. M.; Valentini, A.; Ferrè, N.; Olivucci, M. Probing the Photodynamics of Rhodopsins with Reduced Retinal Chromophores. *J. Chem. Theory Comput.* **2016**, *12* (2), 839–850. https://doi.org/10.1021/acs.jctc.5b00945.
(34) Calbo, J.; Weston, C. E.; White, A. J. P.; Rzepa, H. S.; Contreras-García, J.; Fuchter, M. J. Tuning Azoheteroarene Photoswitch Performance through Heteroaryl Design. *J. Am. Chem. Soc.* **2017**, *139* (3), 1261–1274. https://doi.org/10.1021/jacs.6b11626.
(35) Volarić, J.; Szymanski, W.; A. Simeth, N.; L. Feringa, B. Molecular Photoswitches in Aqueous Environments. *Chem. Soc. Rev.* **2021**, *50* (22), 12377–12449. https://doi.org/10.1039/D0CS00547A.
(36) T. Abiola, T.; Rioux, B.; M. Toldo, J.; Alarcan, J.; M. Woolley, J.; P. Turner, M. A.; L. Coxon, D. J.; Casal, M. T. do; Peyrot, C.; M. Mention, M.; J. Buma, W.; R. Ashfold, M. N.; Braeuning, A.; Barbatti, M.; G. Stavros, V.; Allais, F. Towards Developing Novel and Sustainable Molecular Light-to-Heat Converters. *Chem. Sci.* **2021**, *12* (46), 15239–15252. https://doi.org/10.1039/D1SC05077J.
(37) Tehfe, M.-A.; Dumur, F.; Graff, B.; Morlet-Savary, F.; Gigmes, D.; Fouassier, J.-P.; Lalevée, J. Push–Pull (Thio)Barbituric Acid Derivatives in Dye Photosensitized Radical and Cationic Polymerization Reactions under 457/473 Nm Laser Beams or Blue LEDs. *Polym. Chem.* **2013**, *4* (13), 3866–3875. https://doi.org/10.1039/C3PY00372H.
(38) De Camillis, S.; Miles, J.; Alexander, G.; Ghafur, O.; D. Williams, I.; Townsend, D.; B. Greenwood, J. Ultrafast Non-Radiative Decay of Gas-Phase Nucleosides. *Phys. Chem. Chem. Phys.* **2015**, *17* (36), 23643–23650. https://doi.org/10.1039/C5CP03806E.
(39) Mansour, R.; Toldo, J. M.; Barbatti, M. Role of the Hydrogen Bond on the Internal Conversion of Photoexcited Adenosine. *J. Phys. Chem. Lett.* **2022**, *13* (26), 6194–6199. https://doi.org/10.1021/acs.jpclett.2c01554.
(40) Bennett, O.; Freibert, A.; Spinlove, K. E.; Worth, G. A. Prediction through Quantum Dynamics Simulations: Photo-Excited Cyclobutanone. *J. Chem. Phys.* **2024**, *160* (17), 174305. https://doi.org/10.1063/5.0203654.
(41) Eng, J.; Rankine, C. D.; Penfold, T. J. The Photochemistry of Rydberg-Excited Cyclobutanone: Photoinduced Processes and Ground State Dynamics. *J. Chem. Phys.* **2024**, *160* (15), 154301. https://doi.org/10.1063/5.0203597.
(42) Hait, D.; Lahana, D.; Fajen, O. J.; Paz, A. S. P.; Unzueta, P. A.; Rana, B.; Lu, L.; Wang, Y.; Kjønstad, E. F.; Koch, H.; Martínez, T. J. Prediction of Photodynamics of 200 Nm

Excited Cyclobutanone with Linear Response Electronic Structure and Ab Initio Multiple Spawning. *J. Chem. Phys.* **2024**, *160* (24), 244101. https://doi.org/10.1063/5.0203800.
(43) Hutton, L.; Moreno Carrascosa, A.; Prentice, A. W.; Simmermacher, M.; Runeson, J. E.; Paterson, M. J.; Kirrander, A. Using a Multistate Mapping Approach to Surface Hopping to Predict the Ultrafast Electron Diffraction Signal of Gas-Phase Cyclobutanone. *J. Chem. Phys.* **2024**, *160* (20), 204307. https://doi.org/10.1063/5.0203667.
(44) Jaiswal, V. K.; Montorsi, F.; Aleotti, F.; Segatta, F.; Keefer, D.; Mukamel, S.; Nenov, A.; Conti, I.; Garavelli, M. Ultrafast Photochemistry and Electron-Diffraction Spectra in n → (3s) Rydberg Excited Cyclobutanone Resolved at the Multireference Perturbative Level. *J. Chem. Phys.* **2024**, *160* (16), 164316. https://doi.org/10.1063/5.0203624.
(45) Janoš, J.; Figueira Nunes, J. P.; Hollas, D.; Slavíček, P.; Curchod, B. F. E. Predicting the Photodynamics of Cyclobutanone Triggered by a Laser Pulse at 200 Nm and Its MeV-UED Signals—A Trajectory Surface Hopping and XMS-CASPT2 Perspective. *J. Chem. Phys.* **2024**, *160* (14), 144305. https://doi.org/10.1063/5.0203105.
(46) Lawrence, J. E.; Ansari, I. M.; Mannouch, J. R.; Manae, M. A.; Asnaashari, K.; Kelly, A.; Richardson, J. O. A MASH Simulation of the Photoexcited Dynamics of Cyclobutanone. *J. Chem. Phys.* **2024**, *160* (17), 174306. https://doi.org/10.1063/5.0203695.
(47) Makhov, D. V.; Hutton, L.; Kirrander, A.; Shalashilin, D. V. Ultrafast Electron Diffraction of Photoexcited Gas-Phase Cyclobutanone Predicted by Ab Initio Multiple Cloning Simulations. *J. Chem. Phys.* **2024**, *160* (16), 164310. https://doi.org/10.1063/5.0203683.
(48) Martín Santa Daría, A.; Hernández-Rodríguez, J.; Ibele, L. M.; Gómez, S. Photofragmentation of Cyclobutanone at 200 Nm: TDDFT vs CASSCF Electron Diffraction. *J. Chem. Phys.* **2024**, *160* (11), 114303. https://doi.org/10.1063/5.0197895.
(49) Miao, X.; Diemer, K.; Mitrić, R. A CASSCF/MRCI Trajectory Surface Hopping Simulation of the Photochemical Dynamics and the Gas Phase Ultrafast Electron Diffraction Patterns of Cyclobutanone. *J. Chem. Phys.* **2024**, *160* (12), 124309. https://doi.org/10.1063/5.0197768.
(50) Miller, E. R.; Hoehn, S. J.; Kumar, A.; Jiang, D.; Parker, S. M. *Ultrafast Photochemistry and Electron Diffraction for Cyclobutanone in the S2 State: Surface Hopping with Time-Dependent Density Functional Theory*. arXiv.org. https://doi.org/10.1063/5.0203679.
(51) Mukherjee, S.; Mattos, R. S.; Toldo, J. M.; Lischka, H.; Barbatti, M. Prediction Challenge: Simulating Rydberg Photoexcited Cyclobutanone with Surface Hopping Dynamics Based on Different Electronic Structure Methods. *J. Chem. Phys.* **2024**, *160* (15), 154306. https://doi.org/10.1063/5.0203636.
(52) Peng, J.; Liu, H.; Lan, Z. The Photodissociation Dynamics and Ultrafast Electron Diffraction Image of Cyclobutanone from the Surface Hopping Dynamics Simulation. *J. Chem. Phys.* **2024**, *160* (22), 224305. https://doi.org/10.1063/5.0203462.
(53) Suchan, J.; Liang, F.; Durden, A. S.; Levine, B. G. Prediction Challenge: First Principles Simulation of the Ultrafast Electron Diffraction Spectrum of Cyclobutanone. *J. Chem. Phys.* **2024**, *160* (13), 134310. https://doi.org/10.1063/5.0198333.

(54) Vindel-Zandbergen, P.; González-Vázquez, J. Non Adiabatic Dynamics of Photoexcited Cyclobutanone: Predicting Structural Measurements from Trajectory Surface Hopping with XMS-CASPT2 Simulations. arXiv February 16, 2024. https://doi.org/10.48550/arXiv.2402.11090.
(55) Kuhlman, T. S.; Sauer, S. P. A.; Sølling, T. I.; Møller, K. B. Symmetry, Vibrational Energy Redistribution and Vibronic Coupling: The Internal Conversion Processes of Cycloketones. *J. Chem. Phys.* **2012**, *137* (22), 22A522. https://doi.org/10.1063/1.4742313.
(56) Janoš, J.; Slavíček, P. What Controls the Quality of Photodynamical Simulations? Electronic Structure Versus Nonadiabatic Algorithm. *J. Chem. Theory Comput.* **2023**, *19* (22), 8273–8284. https://doi.org/10.1021/acs.jctc.3c00908.
(57) Barbatti, M.; Ruckenbauer, M.; Plasser, F.; Pittner, J.; Granucci, G.; Persico, M.; Lischka, H. Newton-X: A Surface-Hopping Program for Nonadiabatic Molecular Dynamics. *Wiley Interdiscip. Rev. Comput. Mol. Sci.* **2014**, *4* (1), 26–33. https://doi.org/10.1002/wcms.1158.
(58) Barbatti, M.; Granucci, G.; Persico, M.; Ruckenbauer, M.; Vazdar, M.; Eckert-Maksić, M.; Lischka, H. The On-the-Fly Surface-Hopping Program System Newton-X: Application to Ab Initio Simulation of the Nonadiabatic Photodynamics of Benchmark Systems. *J. Photochem. Photobiol. Chem.* **2007**, *190* (2–3), 228–240. https://doi.org/10.1016/j.jphotochem.2006.12.008.
(59) Barbatti, M.; Bondanza, M.; Crespo-Otero, R.; Demoulin, B.; Dral, P. O.; Granucci, G.; Kossoski, F.; Lischka, H.; Mennucci, B.; Mukherjee, S.; Pederzoli, M.; Persico, M.; Pinheiro Jr, M.; Pittner, J.; Plasser, F.; Sangiogo Gil, E.; Stojanovic, L. Newton-X Platform: New Software Developments for Surface Hopping and Nuclear Ensembles. *J. Chem. Theory Comput.* **2022**, *18* (11), 6851–6865. https://doi.org/10.1021/acs.jctc.2c00804.
(60) Ben-Nun, M.; Quenneville, J.; Martínez, T. J. Ab Initio Multiple Spawning: Photochemistry from First Principles Quantum Molecular Dynamics. *J. Phys. Chem. A* **2000**, *104* (22), 5172–5175. https://doi.org/10.1021/jp994174i.
(61) Brumer, P.; Shapiro, M. Molecular Response in One-Photon Absorption via Natural Thermal Light vs. Pulsed Laser Excitation. *Proc. Natl. Acad. Sci.* **2012**, *109* (48), 19575–19578. https://doi.org/10.1073/pnas.1211209109.
(62) Jablonski, A. Efficiency of Anti-Stokes Fluorescence in Dyes. *Nature* **1933**, *131* (3319), 839–840. https://doi.org/10.1038/131839b0.
(63) Garavelli, M. Computational Organic Photochemistry: Strategy, Achievements and Perspectives. *Theor. Chem. Acc.* **2006**, *116* (1), 87–105. https://doi.org/10.1007/s00214-005-0030-z.
(64) Toldo, J. M.; Casal, M. T. do; Ventura, E.; Monte, S. A. do; Barbatti, M. Surface Hopping Modeling of Charge and Energy Transfer in Active Environments. *Phys. Chem. Chem. Phys.* **2023**, *25* (12), 8293–8316. https://doi.org/10.1039/D3CP00247K.
(65) Bozzi, A. S.; Rocha, W. R. Calculation of Excited State Internal Conversion Rate Constant Using the One-Effective Mode Marcus-Jortner-Levich Theory. *J. Chem. Theory Comput.* **2023**, *19* (8), 2316–2326. https://doi.org/10.1021/acs.jctc.2c01288.
(66) Marian, C. M. Spin–Orbit Coupling and Intersystem Crossing in Molecules. *WIREs Comput. Mol. Sci.* **2012**, *2* (2), 187–203. https://doi.org/10.1002/wcms.83.
(67) Mukherjee, S.; Fedorov, D. A.; Varganov, S. A. Modeling Spin-Crossover Dynamics. *Annu. Rev. Phys. Chem.* **2021**, *72* (Volume 72, 2021), 515–540. https://doi.org/10.1146/annurev-physchem-101419-012625.

(68) Klessinger, M.; Michl, J. *Excited States and Photochemistry of Organic Molecules*; VCH Publishers, Inc., 1995.
(69) Pérez-Escribano, M.; Jankowska, J.; Granucci, G.; Escudero, D. The Radiative Surface Hopping (RSH) Algorithm: Capturing Fluorescence Events in Molecular Systems within a Semi-Classical Non-Adiabatic Molecular Dynamics Framework. *J. Chem. Phys.* **2023**, *158* (12), 124104. https://doi.org/10.1063/5.0139516.
(70) Mukherjee, S.; Pinheiro, M.; Demoulin, B.; Barbatti, M. Simulations of Molecular Photodynamics in Long Timescales. *Philos. Trans. R. Soc. Math. Phys. Eng. Sci.* **2022**, *380* (2223), 20200382. https://doi.org/10.1098/rsta.2020.0382.
(71) Domcke, W.; Yarkony, D. R.; Köppel, H. *Conical Intersections: Electronic Structure, Dynamics & Spectroscopy*; World Scientific Publishing Co. Pte. Ltd.: Singapore, 2004.
(72) Baer, M. *Beyond Born-Oppenheimer: Conical Intersections and Electronic Nonadiabatic Coupling Terms*; John Wiley & Sons, Inc.: Hoboken, NJ, USA, 2006. https://doi.org/10.1002/0471780081.
(73) Nelson, T. R.; White, A. J.; Bjorgaard, J. A.; Sifain, A. E.; Zhang, Y.; Nebgen, B.; Fernandez-Alberti, S.; Mozyrsky, D.; Roitberg, A. E.; Tretiak, S. Non-Adiabatic Excited-State Molecular Dynamics: Theory and Applications for Modeling Photophysics in Extended Molecular Materials. *Chem. Rev.* **2020**, *120* (4), 2215–2287. https://doi.org/10.1021/acs.chemrev.9b00447.
(74) Kapral, R. Surface Hopping from the Perspective of Quantum–Classical Liouville Dynamics. *Chem. Phys.* **2016**, *481*, 77–83. https://doi.org/10.1016/j.chemphys.2016.05.016.
(75) Martens, C. C. Nonadiabatic Dynamics in the Semiclassical Liouville Representation: Locality, Transformation Theory, and the Energy Budget. *Chem. Phys.* **2016**, *481*, 60–68. https://doi.org/10.1016/j.chemphys.2016.06.013.
(76) Zhu, C.; Jasper, A. W.; Truhlar, D. G. Non-Born-Oppenheimer Liouville-von Neumann Dynamics. Evolution of a Subsystem Controlled by Linear and Population-Driven Decay of Mixing with Decoherent and Coherent Switching. *J. Chem. Theory Comput.* **2005**, *1* (4), 527–540. https://doi.org/10.1021/ct050021p.
(77) Meyer, H.-D.; Manthe, U.; Cederbaum, L. S. The Multi-Configurational Time-Dependent Hartree Approach. *Chem. Phys. Lett.* **1990**, *165* (1), 73–78. https://doi.org/10.1016/0009-2614(90)87014-I.
(78) *Multidimensional Quantum Dynamics: MCTDH Theory and Applications*; Meyer, H.-D., Gatti, F., Worth, G. A., Eds.; WILEY-VCH: Weinheim, 2009.
(79) Meyer, H. D. Studying Molecular Quantum Dynamics with the Multiconfiguration Time-Dependent Hartree Method. *Wiley Interdiscip. Rev. Comput. Mol. Sci.* **2012**, *2* (2), 351–374. https://doi.org/10.1002/wcms.87.
(80) Beck, M. H.; A. Jäckle; G. A. Worth; H.-D. Meyer. The Multiconfiguration Time-Dependent Hartree (MCTDH) Method: A Highly Efficient Algorithm for Propagating Wavepackets. *Phys. Rep.* **2000**, *324* (1), 1–105. https://doi.org/10.1016/S0370-1573(99)00047-2.
(81) Worth, G. A. Quantum Dynamics Using Pseudo-Particle Trajectories: A New Approach Based on the Multiconfiguration Time-Dependent Hartree Method. *J. Chem. Phys.* **2001**, *114* (4), 1524–1533. https://doi.org/10.1063/1.1336572.
(82) Wang, H. Multilayer Multiconfiguration Time-Dependent Hartree Theory. *J. Phys. Chem. A* **2015**, *119* (29), 7951–7965. https://doi.org/10.1021/acs.jpca.5b03256.
(83) Wang, H.; Thoss, M. Multilayer Formulation of the Multiconfiguration Time-Dependent Hartree Theory. *J. Chem. Phys.* **2003**, *119* (3), 1289–1299. https://doi.org/10.1063/1.1580111.

(84) Worth, G. A.; Burghardt, I. Full Quantum Mechanical Molecular Dynamics Using Gaussian Wavepackets. *Chem. Phys. Lett.* **2003**, *368* (3), 502–508. https://doi.org/10.1016/S0009-2614(02)01920-6.
(85) Worth, G. A.; Robb, M. A.; Burghardt, I. A Novel Algorithm for Non-Adiabatic Direct Dynamics Using Variational Gaussian Wavepackets. *Faraday Discuss.* **2004**, *127*, 307–323. https://doi.org/10.1039/b314253a.
(86) Lasorne, B.; Bearpark, M. J.; Robb, M. A.; Worth, G. A. Direct Quantum Dynamics Using Variational Multi-Configuration Gaussian Wavepackets. *Chem. Phys. Lett.* **2006**, *432* (4–6), 604–609. https://doi.org/10.1016/j.cplett.2006.10.099.
(87) Lasorne, B.; Robb, M. A.; Worth, G. A. Direct Quantum Dynamics Using Variational Multi-Configuration Gaussian Wavepackets. Implementation Details and Test Case. *Phys. Chem. Chem. Phys.* **2007**, *9* (25), 3210–3227. https://doi.org/10.1039/B700297A.
(88) Worth, G. A.; Robb, M. A.; Lasorne, B. Solving the Time-Dependent Schrödinger Equation for Nuclear Motion in One Step: Direct Dynamics of Non-Adiabatic Systems. *Mol. Phys.* **2008**, *106* (16–18), 2077–2091. https://doi.org/10.1080/00268970802172503.
(89) Heller, E. J. Frozen Gaussians: A Very Simple Semiclassical Approximation. *J. Chem. Phys.* **1981**, *75* (6), 2923–2931. https://doi.org/10.1063/1.442382.
(90) Crespo-Otero, R.; Barbatti, M. Recent Advances and Perspectives on Nonadiabatic Mixed Quantum-Classical Dynamics. *Chemical Reviews*, 2018, *118*, 7026–7068. https://doi.org/10.1021/acs.chemrev.7b00577.
(91) Tully, J. C. Molecular Dynamics with Electronic Transitions. *J. Chem. Phys.* **1990**, *93* (2), 1061–1071. https://doi.org/10.1063/1.459170.
(92) Tully, J. C.; Pkeston, R. K. Trajectory Surface Hopping Approach to Nonadiabatic Molecular Collisions: The Reaction of H+ with D2. *J. Chem. Phys.* **1971**, *55* (2), 562–572. https://doi.org/10.1063/1.1675788.
(93) Billing, Gert. D. Classical Path Method in Inelastic and Reactive Scattering. *Int. Rev. Phys. Chem.* **1994**, *13* (2), 309–335. https://doi.org/10.1080/01442359409353298.
(94) Shalashilin, D. V. Quantum Mechanics with the Basis Set Guided by Ehrenfest Trajectories: Theory and Application to Spin-Boson Model. *J. Chem. Phys.* **2009**, *130* (24), 244101. https://doi.org/10.1063/1.3153302.
(95) Shu, Y.; Truhlar, D. G. Generalized Semiclassical Ehrenfest Method: A Route to Wave Function-Free Photochemistry and Nonadiabatic Dynamics with Only Potential Energies and Gradients. *J. Chem. Theory Comput.* **2024**. https://doi.org/10.1021/acs.jctc.4c00424.
(96) Messiah, A. *Quantum Mechanics*; John Wiley & Sons: New York, 1962; Vol. 1.
(97) Tully, J. C. Mixed Quantum–Classical Dynamics. *Faraday Discuss.* **1998**, *110* (0), 407–419. https://doi.org/10.1039/A801824C.
(98) Granucci, G.; Persico, M. Critical Appraisal of the Fewest Switches Algorithm for Surface Hopping. *J. Chem. Phys.* **2007**, *126* (13), 134114. https://doi.org/10.1063/1.2715585.
(99) Subotnik, J. E.; Ouyang, W.; Landry, B. R. Can We Derive Tully's Surface-Hopping Algorithm from the Semiclassical Quantum Liouville Equation? Almost, but Only with Decoherence. *J. Chem. Phys.* **2013**, *139* (21), 214107. https://doi.org/10.1063/1.4829856.

(100) Subotnik, J. E.; Shenvi, N. A New Approach to Decoherence and Momentum Rescaling in the Surface Hopping Algorithm. *J. Chem. Phys.* **2011**, *134* (2). https://doi.org/10.1063/1.3506779.
(101) Curchod, B. F. E.; Martínez, T. J. Ab Initio Nonadiabatic Quantum Molecular Dynamics. *Chem. Rev.* **2018**, *118* (7), 3305–3336. https://doi.org/10.1021/acs.chemrev.7b00423.
(102) Shalashilin, D. V. Nonadiabatic Dynamics with the Help of Multiconfigurational Ehrenfest Method: Improved Theory and Fully Quantum 24D Simulation of Pyrazine. *J. Chem. Phys.* **2010**, *132* (24), 244111. https://doi.org/10.1063/1.3442747.
(103) Shalashilin, D. V. Multiconfigurational Ehrenfest Approach to Quantum Coherent Dynamics in Large Molecular Systems. *Faraday Discuss.* **2011**, *153* (0), 105–116. https://doi.org/10.1039/C1FD00034A.
(104) Makhov, D. V.; Glover, W. J.; Martinez, T. J.; Shalashilin, D. V. Ab Initio Multiple Cloning Algorithm for Quantum Nonadiabatic Molecular Dynamics. *J. Chem. Phys.* **2014**, *141* (5). https://doi.org/10.1063/1.4891530.
(105) Song, H.; Freixas, V. M.; Fernandez-Alberti, S.; White, A. J.; Zhang, Y.; Mukamel, S.; Govind, N.; Tretiak, S. An Ab Initio Multiple Cloning Method for Non-Adiabatic Excited-State Molecular Dynamics in NWChem. *J. Chem. Theory Comput.* **2021**, *17* (6), 3629–3643. https://doi.org/10.1021/acs.jctc.1c00131.
(106) Joubert-Doriol, L.; Izmaylov, A. F. Nonadiabatic Quantum Dynamics with Frozen-Width Gaussians. *J. Phys. Chem. A* **2018**, *122* (29), 6031–6042. https://doi.org/10.1021/acs.jpca.8b03404.
(107) Heller, E. J. *The Semiclassical Way to Dynamics and Spectroscopy*; Princeton University Press: Princeton, 2018.
(108) Izmaylov, A. F.; Joubert-Doriol, L. Quantum Nonadiabatic Cloning of Entangled Coherent States. *J. Phys. Chem. Lett.* **2017**, *8* (8), 1793–1797. https://doi.org/10.1021/acs.jpclett.7b00596.
(109) Shu, Y.; Truhlar, D. G. Decoherence and Its Role in Electronically Nonadiabatic Dynamics. *J. Chem. Theory Comput.* **2023**. https://doi.org/10.1021/acs.jctc.2c00988.
(110) Bittner, E. R.; Rossky, P. J. Quantum Decoherence in Mixed Quantum-classical Systems: Nonadiabatic Processes. *J. Chem. Phys.* **1995**, *103* (18), 8130–8143. https://doi.org/10.1063/1.470177.
(111) Granucci, G.; Persico, M.; Zoccante, A. Including Quantum Decoherence in Surface Hopping. *J. Chem. Phys.* **2010**, *133* (13), 134111. https://doi.org/10.1063/1.3489004.
(112) Zhu, C.; Nangia, S.; Jasper, A. W.; Truhlar, D. G. Coherent Switching with Decay of Mixing: An Improved Treatment of Electronic Coherence for Non-Born–Oppenheimer Trajectories. *J. Chem. Phys.* **2004**, *121* (16), 7658–7670. https://doi.org/10.1063/1.1793991.
(113) Fabiano, E.; Keal, T. W.; Thiel, W. Implementation of Surface Hopping Molecular Dynamics Using Semiempirical Methods. *Chem. Phys.* **2008**, *349* (1), 334–347. https://doi.org/10.1016/j.chemphys.2008.01.044.
(114) Ibele, L. M.; Curchod, B. F. E. A Molecular Perspective on Tully Models for Nonadiabatic Dynamics. *Phys. Chem. Chem. Phys.* **2020**, *22* (27), 15183–15196. https://doi.org/10.1039/D0CP01353F.
(115) Toniolo, A.; Ciminelli, C.; Persico, M.; Martínez, T. J. Simulation of the Photodynamics of Azobenzene on Its First Excited State: Comparison of Full Multiple Spawning and

Surface Hopping Treatments. *J. Chem. Phys.* **2005**, *123* (23), 234308. https://doi.org/10.1063/1.2134705.
(116) Martinez, T. J.; Ben-Nun, M.; Ashkenazi, G. Classical/Quantal Method for Multistate Dynamics: A Computational Study. *J. Chem. Phys.* **1996**, *104* (8), 2847–2856. https://doi.org/10.1063/1.471108.
(117) Martinez, T. J.; Ben-Nun, M.; Levine, R. D. Multi-Electronic-State Molecular Dynamics: A Wave Function Approach with Applications. *J. Phys. Chem.* **1996**, *100* (19), 7884–7895. https://doi.org/10.1021/jp953105a.
(118) Martínez, T. J.; Levine, R. D. Non-Adiabatic Molecular Dynamics: Split-Operator Multiple Spawning with Applications to Photodissociation. *J. Chem. Soc. Faraday Trans.* **1997**, *93* (5), 941–947. https://doi.org/10.1039/A605958I.
(119) Curchod, B. F. E.; Glover, W. J.; Martínez, T. J. SSAIMS—Stochastic-Selection Ab Initio Multiple Spawning for Efficient Nonadiabatic Molecular Dynamics. *J. Phys. Chem. A* **2020**, *124* (30), 6133–6143. https://doi.org/10.1021/acs.jpca.0c04113.
(120) Lassmann, Y.; Curchod, B. F. E. AIMSWISS-Ab Initio Multiple Spawning with Informed Stochastic Selections. *J. Chem. Phys.* **2021**, *154* (21), 211106. https://doi.org/10.1063/5.0052118.
(121) Virshup, A. M.; Levine, B. G.; Martínez, T. J. Steric and Electrostatic Effects on Photoisomerization Dynamics Using QM/MM Ab Initio Multiple Spawning. *Theor. Chem. Acc.* **2014**, *133* (7), 1506. https://doi.org/10.1007/s00214-014-1506-5.
(122) Mignolet, B.; Curchod, B. F. E. A Walk through the Approximations of Ab Initio Multiple Spawning. *J. Chem. Phys.* **2018**, *148* (13). https://doi.org/10.1063/1.5022877.
(123) Thompson, A. L.; Punwong, C.; Martínez, T. J. Optimization of Width Parameters for Quantum Dynamics with Frozen Gaussian Basis Sets. *Chem. Phys.* **2010**, *370* (1–3), 70–77. https://doi.org/10.1016/j.chemphys.2010.03.020.
(124) Born, M.; Huang, K. *Dynamical Theory of Crystal Lattices*, Repr.; The international series of monographs on physics; Clarendon Pr: Oxford, 1954.
(125) Ben-Nun, M.; Martínez, T. J. Nonadiabatic Molecular Dynamics: Validation of the Multiple Spawning Method for a Multidimensional Problem. *J. Chem. Phys.* **1998**, *108* (17), 7244–7257. https://doi.org/10.1063/1.476142.
(126) Fedorov, D. A.; Seritan, S.; Fales, B. S.; Martínez, T. J.; Levine, B. G. PySpawn: Software for Nonadiabatic Quantum Molecular Dynamics. *J. Chem. Theory Comput.* **2020**, *16* (9), 5485–5498. https://doi.org/10.1021/acs.jctc.0c00575.
(127) Ben-Nun, M.; Martínez, T. J. Exploiting Temporal Nonlocality to Remove Scaling Bottlenecks in Nonadiabatic Quantum Dynamics. *J. Chem. Phys.* **1999**, *110* (9), 4134–4140. https://doi.org/10.1063/1.478297.
(128) Toldo, J. M.; Mattos, R. S.; Pinheiro, M.; Mukherjee, S.; Barbatti, M. Recommendations for Velocity Adjustment in Surface Hopping. *J. Chem. Theory Comput.* **2024**, *20* (2), 614–624. https://doi.org/10.1021/acs.jctc.3c01159.
(129) Baer, M. Introduction to the Theory of Electronic Non-Adiabatic Coupling Terms in Molecular Systems. *Phys. Rep.* **2002**, *358* (2), 75–142. https://doi.org/10.1016/S0370-1573(01)00052-7.
(130) Faraji, S.; Matsika, S.; Krylov, A. I. Calculations of Non-Adiabatic Couplings within Equation-of-Motion Coupled-Cluster Framework: Theory, Implementation, and Validation against Multi-Reference Methods. *J. Chem. Phys.* **2018**, *148* (4), 044103. https://doi.org/10.1063/1.5009433.
(131) Subotnik, J. E.; Alguire, E. C.; Ou, Q.; Landry, B. R.; Fatehi, S. The Requisite Electronic Structure Theory To Describe Photoexcited Nonadiabatic Dynamics: Nonadiabatic

Derivative Couplings and Diabatic Electronic Couplings. *Acc. Chem. Res.* **2015**, *48* (5), 1340–1350. https://doi.org/10.1021/acs.accounts.5b00026.
(132) Pittner, J.; Lischka, H.; Barbatti, M. Optimization of Mixed Quantum-Classical Dynamics: Time-Derivative Coupling Terms and Selected Couplings. *Chem. Phys.* **2009**, *356* (1), 147–152. https://doi.org/10.1016/j.chemphys.2008.10.013.
(133) Ryabinkin, I. G.; Nagesh, J.; Izmaylov, A. F. Fast Numerical Evaluation of Time-Derivative Nonadiabatic Couplings for Mixed Quantum–Classical Methods. *J. Phys. Chem. Lett.* **2015**, *6* (21), 4200–4203. https://doi.org/10.1021/acs.jpclett.5b02062.
(134) Meek, G. A.; Levine, B. G. Evaluation of the Time-Derivative Coupling for Accurate Electronic State Transition Probabilities from Numerical Simulations. *J. Phys. Chem. Lett.* **2014**, *5* (13), 2351–2356. https://doi.org/10.1021/jz5009449.
(135) Meek, G. A.; Levine, B. G. Accurate and Efficient Evaluation of Transition Probabilities at Unavoided Crossings in Ab Initio Multiple Spawning. *Chem. Phys.* **2015**, *460*, 117–124. https://doi.org/10.1016/j.chemphys.2015.06.007.
(136) Hammes-Schiffer, S.; Tully, J. C. Proton Transfer in Solution: Molecular Dynamics with Quantum Transitions. *J. Chem. Phys.* **1994**, *101* (6), 4657–4667. https://doi.org/10.1063/1.467455.
(137) Baeck, K. K.; An, H. Practical Approximation of the Non-Adiabatic Coupling Terms for Same-Symmetry Interstate Crossings by Using Adiabatic Potential Energies Only. *J. Chem. Phys.* **2017**, *146* (6), 064107. https://doi.org/10.1063/1.4975323.
(138) T. do Casal, M.; Toldo, J. M.; Pinheiro Jr, M.; Barbatti, M. Fewest Switches Surface Hopping with Baeck-An Couplings. *Open Res. Eur.* **2021**, *1*, 49. https://doi.org/10.12688/openreseurope.13624.1.
(139) Shu, Y.; Zhang, L.; Chen, X.; Sun, S.; Huang, Y.; Truhlar, D. G. Nonadiabatic Dynamics Algorithms with Only Potential Energies and Gradients: Curvature-Driven Coherent Switching with Decay of Mixing and Curvature-Driven Trajectory Surface Hopping. *J. Chem. Theory Comput.* **2022**, *18* (3), 1320–1328. https://doi.org/10.1021/acs.jctc.1c01080.
(140) Saller, M. A. C.; Habershon, S. Quantum Dynamics with Short-Time Trajectories and Minimal Adaptive Basis Sets. *J. Chem. Theory Comput.* **2017**, *13* (7), 3085–3096. https://doi.org/10.1021/acs.jctc.7b00021.
(141) Shalashilin, D. V.; Child, M. S. Basis Set Sampling in the Method of Coupled Coherent States: Coherent State Swarms, Trains, and Pancakes. *J. Chem. Phys.* **2008**, *128* (5), 1–7. https://doi.org/10.1063/1.2828509.
(142) Kwon, H.-Y.; Morrow, Z.; Kelley, C. T.; Jakubikova, E. Interpolation Methods for Molecular Potential Energy Surface Construction. *J. Phys. Chem. A* **2021**, *125* (45), 9725–9735. https://doi.org/10.1021/acs.jpca.1c06812.
(143) Dral, P. O.; Ge, F.; Hou, Y.-F.; Zheng, P.; Chen, Y.; Barbatti, M.; Isayev, O.; Wang, C.; Xue, B.-X.; Pinheiro Jr, M.; Su, Y.; Dai, Y.; Chen, Y.; Zhang, L.; Zhang, S.; Ullah, A.; Zhang, Q.; Ou, Y. MLatom 3: A Platform for Machine Learning-Enhanced Computational Chemistry Simulations and Workflows. *J. Chem. Theory Comput.* **2024**, *20* (3), 1193–1213. https://doi.org/10.1021/acs.jctc.3c01203.
(144) Lee, H.-W. Wigner Trajectories of a Gaussian Wave Packet Perturbed by a Weak Potential. *Found. Phys.* **1992**, *22* (8), 995–1010. https://doi.org/10.1007/BF00733392.
(145) Agostini, F.; Min, S. K.; Abedi, A.; Gross, E. K. U. Quantum-Classical Nonadiabatic Dynamics: Coupled- vs Independent-Trajectory Methods. *J. Chem. Theory Comput.* **2016**, *12* (5), 2127–2143. https://doi.org/10.1021/acs.jctc.5b01180.

(146) Miao, G.; Subotnik, J. Revisiting the Recoherence Problem in the Fewest Switches Surface Hopping Algorithm. *J. Phys. Chem. A* **2019**, *123* (26), 5428–5435. https://doi.org/10.1021/acs.jpca.9b03188.
(147) Ibele, L. M.; Lassmann, Y.; Martínez, T. J.; Curchod, B. F. E. Comparing (Stochastic-Selection) Ab Initio Multiple Spawning with Trajectory Surface Hopping for the Photodynamics of Cyclopropanone, Fulvene, and Dithiane. *J. Chem. Phys.* **2021**, *154* (10). https://doi.org/10.1063/5.0045572.
(148) Garg, A.; Onuchic, J. N.; Ambegaokar, V. Effect of Friction on Electron Transfer in Biomolecules. *J. Chem. Phys.* **1985**, *83* (9), 4491–4503. https://doi.org/10.1063/1.449017.
(149) Leggett, A. J.; Chakravarty, S.; Dorsey, A. T.; Fisher, M. P. A.; Garg, A.; Zwerger, W. Dynamics of the Dissipative Two-State System. *Rev. Mod. Phys.* **1987**, *59* (1), 1–85. https://doi.org/10.1103/RevModPhys.59.1.
(150) Mac Kernan, D.; Ciccotti, G.; Kapral, R. Surface-Hopping Dynamics of a Spin-Boson System. *J. Chem. Phys.* **2002**, *116* (6), 2346–2353. https://doi.org/10.1063/1.1433502.
(151) Weiss, U. *Quantum Dissipative Systems*, 2nd ed.; Series in Modern Condensed Matter Physics; WORLD SCIENTIFIC, 1999; Vol. 10. https://doi.org/10.1142/4239.
(152) Shenvi, N.; Subotnik, J. E.; Yang, W. Phase-Corrected Surface Hopping: Correcting the Phase Evolution of the Electronic Wavefunction. *J. Chem. Phys.* **2011**, *135* (2), 024101. https://doi.org/10.1063/1.3603447.
(153) Schlosshauer, M. *Decoherence and the Quantum-to-Classical Transition*; Springer, 2007.
(154) Ibele, L.; Memhood, A.; Levine, B. G.; Avagliano, D. Ab Initio Multiple Spawning Nonadiabatic Dynamics with Different CASPT2 Flavors: A Fully Open-Source PySpawn/OpenMolcas Interface. ChemRxiv July 2, 2024. https://doi.org/10.26434/chemrxiv-2024-s8z45.
(155) Habershon, S. Linear Dependence and Energy Conservation in Gaussian Wavepacket Basis Sets. *J. Chem. Phys.* **2012**, *136* (1), 014109. https://doi.org/10.1063/1.3671978.
(156) Asaad, M.; Joubert-Doriol, L.; Izmaylov, A. F. Controlling Energy Conservation in Quantum Dynamics with Independently Moving Basis Functions: Application to Multi-Configuration Ehrenfest. *J. Chem. Phys.* **2022**, *156* (20), 204121. https://doi.org/10.1063/5.0087797.
(157) Wang, L.; Akimov, A.; Prezhdo, O. V. Recent Progress in Surface Hopping: 2011–2015. *J. Phys. Chem. Lett.* **2016**, *7* (11), 2100–2112. https://doi.org/10.1021/acs.jpclett.6b00710.
(158) Mannouch, J. R.; Richardson, J. O. A Mapping Approach to Surface Hopping. *J. Chem. Phys.* **2023**, *158* (10), 104111. https://doi.org/10.1063/5.0139734.
(159) Belyaev, A. K.; Lasser, C.; Trigila, G. Landau–Zener Type Surface Hopping Algorithms. *J. Chem. Phys.* **2014**, *140* (22), 224108. https://doi.org/10.1063/1.4882073.
(160) Suchan, J.; Janoš, J.; Slavíček, P. Pragmatic Approach to Photodynamics: Mixed Landau–Zener Surface Hopping with Intersystem Crossing. *J. Chem. Theory Comput.* **2020**, *16* (9), 5809–5820. https://doi.org/10.1021/acs.jctc.0c00512.
(161) Xie, W.; Sapunar, M.; Došlić, N.; Sala, M.; Domcke, W. Assessing the Performance of Trajectory Surface Hopping Methods: Ultrafast Internal Conversion in Pyrazine. *J. Chem. Phys.* **2019**, *150* (15), 154119. https://doi.org/10.1063/1.5084961.

(162) Yue, L.; Yu, L.; Xu, C.; Lei, Y.; Liu, Y.; Zhu, C. Benchmark Performance of Global Switching versus Local Switching for Trajectory Surface Hopping Molecular Dynamics Simulation: Cis↔Trans Azobenzene Photoisomerization. *ChemPhysChem* **2017**, *18* (10), 1274–1287. https://doi.org/10.1002/cphc.201700049.
(163) Zhang, L.; Pios, S. V.; Martyka, M.; Ge, F.; Hou, Y.-F.; Chen, Y.; Chen, L.; Jankowska, J.; Barbatti, M.; Dral, P. O. MLatom Software Ecosystem for Surface Hopping Dynamics in Python with Quantum Mechanical and Machine Learning Methods. *J. Chem. Theory Comput.* **2024**. https://doi.org/10.1021/acs.jctc.4c00468.
(164) Joubert-Doriol, L. A Variational Approach for Linearly Dependent Moving Bases in Quantum Dynamics: Application to Gaussian Functions. *J. Chem. Theory Comput.* **2022**, *18* (10), 5799–5809. https://doi.org/10.1021/acs.jctc.2c00461.
(165) Tomaz, A. A.; Mattos, R. S.; Barbatti, M. Gravitationally-Induced Wave Function Collapse Time for Molecules. *Phys. Chem. Chem. Phys.* **2024**, *26* (31), 20785–20798. https://doi.org/10.1039/D4CP02364A.
(166) Rahm, M.; Hoffmann, R.; Ashcroft, N. W. Atomic and Ionic Radii of Elements 1 **–96**. *Chem. – Eur. J.* **2016**, *22* (41), 14625–14632. https://doi.org/10.1002/chem.201602949.
(167) Sršeň, Š.; Slavíček, P. Optimal Representation of the Nuclear Ensemble: Application to Electronic Spectroscopy. *J. Chem. Theory Comput.* **2021**, *17* (10), 6395–6404. https://doi.org/10.1021/acs.jctc.1c00749.
(168) Crespo-Otero, R.; Barbatti, M. Spectrum Simulation and Decomposition with Nuclear Ensemble: Formal Derivation and Application to Benzene, Furan and 2-Phenylfuran. *Theor. Chem. Acc.* **2012**, *131* (6), 1237. https://doi.org/10.1007/s00214-012-1237-4.
(169) Case, W. B. Wigner Functions and Weyl Transforms for Pedestrians. *Am. J. Phys.* **2008**, *76* (10), 937–946. https://doi.org/10.1119/1.2957889.
(170) Heil, A.; Marian, C. M. DFT/MRCI Hamiltonian for Odd and Even Numbers of Electrons. *J. Chem. Phys.* **2017**, *147* (19). https://doi.org/10.1063/1.5003246.
(171) Lyskov, I.; Kleinschmidt, M.; Marian, C. M. Redesign of the DFT/MRCI Hamiltonian. *J. Chem. Phys.* **2016**, *144* (3). https://doi.org/10.1063/1.4940036.
(172) Marian, C. M.; Heil, A.; Kleinschmidt, M. The DFT/MRCI Method. *Wiley Interdiscip. Rev. Comput. Mol. Sci.* **2019**, *9* (2), 1–31. https://doi.org/10.1002/wcms.1394.
(173) Dewar, M. J. S.; Thiel, W. *Ground states of molecules. 38. The MNDO method. Approximations and parameters*. ACS Publications. https://doi.org/10.1021/ja00457a004.
(174) Stewart, J. J. P. Optimization of Parameters for Semiempirical Methods IV: Extension of MNDO, AM1, and PM3 to More Main Group Elements. *J. Mol. Model.* **2004**, *10* (2), 155–164. https://doi.org/10.1007/s00894-004-0183-z.
(175) Stewart, J. J. P. Optimization of Parameters for Semiempirical Methods V: Modification of NDDO Approximations and Application to 70 Elements. *J. Mol. Model.* **2007**, *13* (12), 1173–1213. https://doi.org/10.1007/s00894-007-0233-4.
(176) Dral, P. O.; Wu, X.; Spörkel, L.; Koslowski, A.; Weber, W.; Steiger, R.; Scholten, M.; Thiel, W. Semiempirical Quantum-Chemical Orthogonalization-Corrected Methods: Theory, Implementation, and Parameters. *J. Chem. Theory Comput.* **2016**, *12* (3), 1082–1096. https://doi.org/10.1021/acs.jctc.5b01046.
(177) Dewar, M. J. S.; Zoebisch, E. G.; Healy, E. F.; Stewart, J. J. P. Development and Use of Quantum Mechanical Molecular Models. 76. AM1: A New General Purpose Quantum Mechanical Molecular Model. *J. Am. Chem. Soc.* **1985**, *107* (13), 3902–3909. https://doi.org/10.1021/ja00299a024.

(178) Schütt, K. T.; Gastegger, M.; Tkatchenko, A.; Müller, K. R.; Maurer, R. J. Unifying Machine Learning and Quantum Chemistry with a Deep Neural Network for Molecular Wavefunctions. *Nat. Commun.* **2019**, *10* (1), 1–10. https://doi.org/10.1038/s41467-019-12875-2.
(179) Bai, Y.; Vogt-Maranto, L.; Tuckerman, M.; Glover, W. Machine Learning the Hohenberg-Kohn Map to Molecular Excited States. **2022**. https://doi.org/10.26434/chemrxiv-2022-fkcqg.
(180) von Lilienfeld, O. A.; Müller, K. R.; Tkatchenko, A. Exploring Chemical Compound Space with Quantum-Based Machine Learning. *Nat. Rev. Chem.* **2020**. https://doi.org/10.1038/s41570-020-0189-9.
(181) Sun, Q.; Berkelbach, T. C.; Blunt, N. S.; Booth, G. H.; Guo, S.; Li, Z.; Liu, J.; McClain, J.; Sharma, S.; Wouters, S.; Chan, G. K.-L. PySCF: The Python-Based Simulations of Chemistry Framework. *Wiley Interdiscip. Rev. Comput. Mol. Sci.* **2018**, *8*, e1340. https://doi.org/10.1002/wcms.1340.
(182) Li Manni, G.; Fdez. Galván, I.; Alavi, A.; Aleotti, F.; Aquilante, F.; Autschbach, J.; Avagliano, D.; Baiardi, A.; Bao, J. J.; Battaglia, S.; Birnoschi, L.; Blanco-González, A.; Bokarev, S. I.; Broer, R.; Cacciari, R.; Calio, P. B.; Carlson, R. K.; Carvalho Couto, R.; Cerdán, L.; Chibotaru, L. F.; Chilton, N. F.; Church, J. R.; Conti, I.; Coriani, S.; Cuéllar-Zuquin, J.; Daoud, R. E.; Dattani, N.; Decleva, P.; De Graaf, C.; Delcey, M. G.; De Vico, L.; Dobrautz, W.; Dong, S. S.; Feng, R.; Ferré, N.; Filatov(Gulak), M.; Gagliardi, L.; Garavelli, M.; González, L.; Guan, Y.; Guo, M.; Hennefarth, M. R.; Hermes, M. R.; Hoyer, C. E.; Huix-Rotllant, M.; Jaiswal, V. K.; Kaiser, A.; Kaliakin, D. S.; Khamesian, M.; King, D. S.; Kochetov, V.; Krośnicki, M.; Kumaar, A. A.; Larsson, E. D.; Lehtola, S.; Lepetit, M.-B.; Lischka, H.; López Ríos, P.; Lundberg, M.; Ma, D.; Mai, S.; Marquetand, P.; Merritt, I. C. D.; Montorsi, F.; Mörchen, M.; Nenov, A.; Nguyen, V. H. A.; Nishimoto, Y.; Oakley, M. S.; Olivucci, M.; Oppel, M.; Padula, D.; Pandharkar, R.; Phung, Q. M.; Plasser, F.; Raggi, G.; Rebolini, E.; Reiher, M.; Rivalta, I.; Roca-Sanjuán, D.; Romig, T.; Safari, A. A.; Sánchez-Mansilla, A.; Sand, A. M.; Schapiro, I.; Scott, T. R.; Segarra-Martí, J.; Segatta, F.; Sergentu, D.-C.; Sharma, P.; Shepard, R.; Shu, Y.; Staab, J. K.; Straatsma, T. P.; Sørensen, L. K.; Tenorio, B. N. C.; Truhlar, D. G.; Ungur, L.; Vacher, M.; Veryazov, V.; Voß, T. A.; Weser, O.; Wu, D.; Yang, X.; Yarkony, D.; Zhou, C.; Zobel, J. P.; Lindh, R. The OpenMolcas *Web*: A Community-Driven Approach to Advancing Computational Chemistry. *J. Chem. Theory Comput.* **2023**, *19* (20), 6933–6991. https://doi.org/10.1021/acs.jctc.3c00182.
(183) Fdez. Galván, I.; Vacher, M.; Alavi, A.; Angeli, C.; Aquilante, F.; Autschbach, J.; Bao, J. J.; Bokarev, S. I.; Bogdanov, N. A.; Carlson, R. K.; Chibotaru, L. F.; Creutzberg, J.; Dattani, N.; Delcey, M. G.; Dong, S. S.; Dreuw, A.; Freitag, L.; Frutos, L. M.; Gagliardi, L.; Gendron, F.; Giussani, A.; González, L.; Grell, G.; Guo, M.; Hoyer, C. E.; Johansson, M.; Keller, S.; Knecht, S.; Kovačević, G.; Källman, E.; Li Manni, G.; Lundberg, M.; Ma, Y.; Mai, S.; Malhado, J. P.; Malmqvist, P. Å.; Marquetand, P.; Mewes, S. A.; Norell, J.; Olivucci, M.; Oppel, M.; Phung, Q. M.; Pierloot, K.; Plasser, F.; Reiher, M.; Sand, A. M.; Schapiro, I.; Sharma, P.; Stein, C. J.; Sørensen, L. K.; Truhlar, D. G.; Ugandi, M.; Ungur, L.; Valentini, A.; Vancoillie, S.; Veryazov, V.; Weser, O.; Wesołowski, T. A.; Widmark, P. O.; Wouters, S.; Zech, A.; Zobel, J. P.; Lindh, R. OpenMolcas: From Source Code to Insight. *J. Chem. Theory Comput.* **2019**, *15* (11), 5925–5964. https://doi.org/10.1021/acs.jctc.9b00532.
(184) Aquilante, F.; Autschbach, J.; Baiardi, A.; Battaglia, S.; Borin, V. A.; Chibotaru, L. F.; Conti, I.; De Vico, L.; Delcey, M.; Fdez. Galván, I.; Ferré, N.; Freitag, L.; Garavelli, M.; Gong, X.; Knecht, S.; Larsson, E. D.; Lindh, R.; Lundberg, M.; Malmqvist, P. Å.; Nenov,

A.; Norell, J.; Odelius, M.; Olivucci, M.; Pedersen, T. B.; Pedraza-González, L.; Phung, Q. M.; Pierloot, K.; Reiher, M.; Schapiro, I.; Segarra-Martí, J.; Segatta, F.; Seijo, L.; Sen, S.; Sergentu, D.-C.; Stein, C. J.; Ungur, L.; Vacher, M.; Valentini, A.; Veryazov, V. Modern Quantum Chemistry with [Open]Molcas. *J. Chem. Phys.* **2020**, *152* (21), 214117. https://doi.org/10.1063/5.0004835.

(185) Lischka, H.; Müller, T.; Szalay, P. G.; Shavitt, I.; Pitzer, R. M.; Shepard, R. Columbus—a Program System for Advanced Multireference Theory Calculations. *WIREs Comput. Mol. Sci.* **2011**, *1* (2), 191–199. https://doi.org/10.1002/wcms.25.

(186) Lischka, H.; Shepard, R.; Müller, T.; Szalay, P. G.; Pitzer, R. M.; Aquino, A. J. A.; Araújo do Nascimento, M. M.; Barbatti, M.; Belcher, L. T.; Blaudeau, J.-P.; Borges, I., Jr.; Brozell, S. R.; Carter, E. A.; Das, A.; Gidofalvi, G.; González, L.; Hase, W. L.; Kedziora, G.; Kertesz, M.; Kossoski, F.; Machado, F. B. C.; Matsika, S.; do Monte, S. A.; Nachtigallová, D.; Nieman, R.; Oppel, M.; Parish, C. A.; Plasser, F.; Spada, R. F. K.; Stahlberg, E. A.; Ventura, E.; Yarkony, D. R.; Zhang, Z. The Generality of the GUGA MRCI Approach in COLUMBUS for Treating Complex Quantum Chemistry. *J. Chem. Phys.* **2020**, *152* (13), 134110. https://doi.org/10.1063/1.5144267.

(187) Lischka, H.; Shepard, R.; Shavitt, I.; Pitzer, R. M.; Müller, Th.; Szalay, P. G.; Brozell, S. R.; Kedziora, G.; Stahlberg, E. A.; Harrison, R. J.; Nieplocha, J.; Minkoff, M.; Barbatti, M.; M. Schuurmann, D. R. Y., Y. Guan; Matsika, S.; Plasser, F.; E. V. Beck, J.-P. B.; M. Ruckenbauer, J. J. S., B. Sellner; Spada, R. F. K.; Das, A.; Belcher, L. T.; Nieman, R. COLUMBUS, an Ab Initio Electronic Structure Program, Release 7.2, 2022.

(188) Neese, F. The ORCA Program System. *WIREs Comput. Mol. Sci.* **2012**, *2* (1), 73–78. https://doi.org/10.1002/wcms.81.

(189) Neese, F. Software Update: The ORCA Program System—Version 5.0. *WIREs Comput. Mol. Sci.* **2022**, *12* (5), e1606. https://doi.org/10.1002/wcms.1606.

(190) Frisch, M. J.; Trucks, G. W.; Schlegel, H. B.; Scuseria, G. E.; Robb, M. A.; Cheeseman, J. R.; Scalmani, G.; Barone, V.; Petersson, G. A.; Nakatsuji, H.; Li, X.; Caricato, M.; Marenich, A. V.; Bloino, J.; Janesko, B. G.; Gomperts, R.; Mennucci, B.; Hratchian, H. P.; Ortiz, J. V.; Izmaylov, A. F.; Sonnenberg, J. L.; Williams-Young, D.; Ding, F.; Lipparini, F.; Egidi, F.; Goings, J.; Peng, B.; Petrone, A.; Henderson, T.; Ranasinghe, D.; Zakrzewski, V. G.; Gao, J.; Rega, N.; Zheng, G.; Liang, W.; Hada, M.; Ehara, M.; Toyota, K.; Fukuda, R.; Hasegawa, J.; Ishida, M.; Nakajima, T.; Honda, Y.; Kitao, O.; Nakai, H.; Vreven, T.; Throssell, K.; Montgomery, J. A., Jr.; Peralta, J. E.; Ogliaro, F.; Bearpark, M. J.; Heyd, J. J.; Brothers, E. N.; Kudin, K. N.; Staroverov, V. N.; Keith, T. A.; Kobayashi, R.; Normand, J.; Raghavachari, K.; Rendell, A. P.; Burant, J. C.; Iyengar, S. S.; Tomasi, J.; Cossi, M.; Millam, J. M.; Klene, M.; Adamo, C.; Cammi, R.; Ochterski, J. W.; Martin, R. L.; Morokuma, K.; Farkas, O.; Foresman, J. B.; Fox, D. J. Gaussian˜16 Revision C.01, 2016.

(191) Henderson, T. M.; Izmaylov, A. F.; Scalmani, G.; Scuseria, G. E. Can Short-Range Hybrids Describe Long-Range-Dependent Properties? *J. Chem. Phys.* **2009**, *131* (4), 044108. https://doi.org/10.1063/1.3185673.

(192) Chai, J. D.; Head-Gordon, M. Long-Range Corrected Hybrid Density Functionals with Damped Atom-Atom Dispersion Corrections. *Phys. Chem. Chem. Phys.* **2008**, *10* (44), 6615–6620. https://doi.org/10.1039/b810189b.

(193) Helmich-Paris, B.; De Souza, B.; Neese, F.; Izsák, R. An Improved Chain of Spheres for Exchange Algorithm. *J. Chem. Phys.* **2021**, *155* (10), 104109. https://doi.org/10.1063/5.0058766.

(194) Curchod, B. F. E.; Sisto, A.; Martínez, T. J. Ab Initio Multiple Spawning Photochemical Dynamics of DMABN Using GPUs. *J. Phys. Chem. A* **2017**, *121* (1), 265–276. https://doi.org/10.1021/acs.jpca.6b09962.
(195) Yu, J. K.; Bannwarth, C.; Hohenstein, E. G.; Martínez, T. J. Ab Initio Nonadiabatic Molecular Dynamics with Hole–Hole Tamm–Dancoff Approximated Density Functional Theory. *J. Chem. Theory Comput.* **2020**, *16* (9), 5499–5511. https://doi.org/10.1021/acs.jctc.0c00644.
(196) Ufimtsev, I. S.; Martinez, T. J. Quantum Chemistry on Graphical Processing Units. 3. Analytical Energy Gradients, Geometry Optimization, and First Principles Molecular Dynamics. *J. Chem. Theory Comput.* **2009**, *5* (10), 2619–2628. https://doi.org/10.1021/ct9003004.
(197) Ufimtsev, I. S.; Martínez, T. J. Quantum Chemistry on Graphical Processing Units. 1. Strategies for Two-Electron Integral Evaluation. *J. Chem. Theory Comput.* **2008**, *4* (2), 222–231. https://doi.org/10.1021/ct700268q.
(198) Ufimtsev, I. S.; Martinez, T. J. Quantum Chemistry on Graphical Processing Units. 2. Direct Self-Consistent-Field Implementation. *J. Chem. Theory Comput.* **2009**, *5* (4), 1004–1015. https://doi.org/10.1021/ct800526s.
(199) Isborn, C. M.; Luehr, N.; Ufimtsev, I. S.; Martínez, T. J. Excited-State Electronic Structure with Configuration Interaction Singles and Tamm–Dancoff Time-Dependent Density Functional Theory on Graphical Processing Units. *J. Chem. Theory Comput.* **2011**, *7* (6), 1814–1823. https://doi.org/10.1021/ct200030k.
(200) Slavíček, P.; Martínez, T. J. Ab Initio Floating Occupation Molecular Orbital-Complete Active Space Configuration Interaction: An Efficient Approximation to CASSCF. *J. Chem. Phys.* **2010**, *132* (23), 234102. https://doi.org/10.1063/1.3436501.
(201) Yanai, T.; Tew, D. P.; Handy, N. C. A New Hybrid Exchange-Correlation Functional Using the Coulomb-Attenuating Method (CAM-B3LYP). *Chem. Phys. Lett.* **2004**, *393* (1–3), 51–57. https://doi.org/10.1016/j.cplett.2004.06.011.
(202) Dral, P. O.; Wu, X.; Thiel, W. Semiempirical Quantum-Chemical Methods with Orthogonalization and Dispersion Corrections. *J. Chem. Theory Comput.* **2019**, *15* (3), 1743–1760. https://doi.org/10.1021/acs.jctc.8b01265.
(203) Ben-Nun, M.; Martínez, T. J. A Continuous Spawning Method for Nonadiabatic Dynamics and Validation for the Zero-Temperature Spin-Boson Problem. *Isr. J. Chem.* **2007**, *47* (1), 75–88. https://doi.org/10.1560/IJC.47.1.75.
(204) Diósi, L. Models for Universal Reduction of Macroscopic Quantum Fluctuations. *Phys. Rev. A* **1989**, *40* (3), 1165–1174. https://doi.org/10.1103/PhysRevA.40.1165.
(205) Penrose, R. On Gravity's Role in Quantum State Reduction. *Gen. Relativ. Gravit.* **1996**, *28* (5), 581–600. https://doi.org/10.1007/BF02105068.
(206) Penrose, R. On the Gravitization of Quantum Mechanics 1: Quantum State Reduction. *Found. Phys.* **2014**, *44* (5), 557–575. https://doi.org/10.1007/s10701-013-9770-0.
(207) Diósi, L. On the Conjectured Gravity-Related Collapse Rate $E\Delta/\hbar$ of Massive Quantum Superpositions. *AVS Quantum Sci.* **2022**, *4* (1), 015605. https://doi.org/10.1116/5.0077919.
(208) Donadi, S.; Bassi, A. Seven Nonstandard Models Coupling Quantum Matter and Gravity. *AVS Quantum Sci.* **2022**, *4* (2), 025601. https://doi.org/10.1116/5.0089318.
(209) Bircher, M. P.; Liberatore, E.; Browning, N. J.; Brickel, S.; Hofmann, C.; Patoz, A.; Unke, O. T.; Zimmermann, T.; Chergui, M.; Hamm, P.; Keller, U.; Meuwly, M.; Woerner, H.-

J.; Vaníček, J.; Rothlisberger, U. Nonadiabatic Effects in Electronic and Nuclear Dynamics. *Struct. Dyn.* **2017**, *4* (6), 061510. https://doi.org/10.1063/1.4996816.

ANNEXES

A. Equations-of-motion of the nuclear coefficients

Using the Born-Huang expansion of the total wavefunction is

$$\Psi(\mathbf{r},\mathbf{R},t)=\sum_{J}^{\infty}\Omega_J(\mathbf{R},t)\phi_J(\mathbf{r};\mathbf{R}) \tag{39}$$

where the nuclear wavepacket of each electronic state can be represented as

$$\begin{aligned}\Omega_J(\mathbf{R},t)&=\sum_{j}^{N_J}C_j^J(t)\chi_j^J(\mathbf{R})\\ \chi_j^J(\mathbf{R})&=\prod_{\rho=1}^{3N}\left(\frac{2\omega_\rho}{\pi}\right)^{1/4}exp[-\omega_\rho(R_\rho-\bar{R}_{j\rho}^J(t))^2+i\bar{P}_{j\rho}^J(t)(R_\rho-\bar{R}_{j\rho}^J(t))+i\gamma_j(t)]\end{aligned} \tag{40}$$

and applying it in the usual time-dependent Schrödinger equation

$$i\frac{\partial\Psi(\mathbf{r},\mathbf{R},t))}{\partial t}=\hat{H}(\mathbf{r},\mathbf{R})\Psi(\mathbf{r},\mathbf{R},t) \tag{41}$$

one can start the process of finding the equation for the time derivative of the coefficients $C_j{}^J(t)$. In these equations, **r** and **R** represent the electronic and nuclear coordinates, respectively. Initially, the substitution leads to

$$i\frac{\partial}{\partial t}\sum_{J}^{\infty}\sum_{j}^{N_J}C_j^J\chi_j^J\phi_J=\hat{H}\sum_{J}^{\infty}\sum_{j}^{N_J}C_j^J\chi_j^J\phi_J \tag{42}$$

The chain rule can open the right side of the equation

$$\frac{\partial}{\partial t}\sum_{J}^{\infty}\sum_{j}^{N_J}C_j^J\chi_j^J\phi_J=\sum_{J}^{\infty}\sum_{j}^{N_J}\dot{C}_j^J\chi_j^J\phi_J+C_j^J\dot{\chi}_j^J\phi_J \tag{43}$$

and then projected over the basis of the wavefunction

$$\begin{aligned}\left\langle\chi_i^I\phi_I\left|\frac{\partial}{\partial t}\right|\Psi\right\rangle_{\mathbf{r},\mathbf{R}}&=\sum_{J}^{\infty}\sum_{j}^{N_J}\left\langle\chi_i^I\phi_I\left|\dot{C}_j^J\right|\chi_j^J\phi_J\right\rangle_{\mathbf{r},\mathbf{R}}+C_j^J\left\langle\chi_i^I\phi_I\left|\dot{\chi}_j^J\phi_J\right.\right\rangle_{\mathbf{r},\mathbf{R}}\\&=\sum_{J}^{\infty}\sum_{j}^{N_J}\dot{C}_j^JS_{ij}\delta_{IJ}+C_j^J\dot{S}_{ij}\delta_{IJ}\end{aligned} \tag{44}$$

The coefficients do not depend on the position coordinates, so they do not participate in the integration, which is performed over the variables indicated in the bracket indexes. The product of the basis function leads to the overlap matrix elements since the nuclear wave packets are not orthogonal in general, times the electronic overlap matrix elements, which are orthonormal by construction. It also leads to the time derivative of the overlap matrix elements $\dot{S}_{ij}$.

The right side of Eq. (42) can go through the same projection over the basis functions, leading to one term of the kinetic operator and another term of the electronic operator

$$\begin{aligned}\left\langle \chi_i^I \phi_I \left| \hat{H} \right| \Psi \right\rangle_{\mathbf{r},\mathbf{R}} &= \left\langle \chi_i^I \phi_I \left| (\hat{T}_n + \hat{H}_{el}) \right| \sum_J^{\infty} \sum_j^{N_J} C_j^J \chi_j^J \phi_J \right\rangle_{\mathbf{r},\mathbf{R}} \\ &= \sum_J^{\infty} \sum_j^{N_J} C_j^J \left\langle \chi_i^I \phi_I \left| \hat{T}_n \right| \chi_j^J \phi_J \right\rangle_{\mathbf{r},\mathbf{R}} + C_j^J \left\langle \chi_i^I \phi_I \left| \hat{H}_{el} \right| \chi_j^J \phi_J \right\rangle_{\mathbf{r},\mathbf{R}}\end{aligned} \tag{45}$$

The kinetic operator can be opened, leading to the appearance of the nonadiabatic elements:

$$\begin{aligned}\left\langle \chi_i^I \phi_I \left| \hat{T}_n \right| \chi_j^J \phi_J \right\rangle_{\mathbf{r},\mathbf{R}} &= -\frac{1}{2M} \langle \chi_i^I \phi_I \mid \nabla_{\mathbf{R}}^2 \mid \chi_j^J \phi_J \rangle_{\mathbf{r},\mathbf{R}} \\ &= \langle \chi_i^I \mid \hat{T}_n \mid \chi_j^J \rangle_{\mathbf{r},\mathbf{R}} \delta_{IJ} - \frac{1}{M} \langle \chi_i^I \mid \mathbf{d}_{IJ} \cdot \nabla_{\mathbf{R}} \mid \chi_j^J \rangle_{\mathbf{R}} - \frac{1}{2M} \langle \chi_i^I \mid D_{IJ} \mid \chi_j^J \rangle_{\mathbf{R}}\end{aligned} \tag{46}$$

The first term of the expansion is simply the kinetic energy operator acting solely on the nuclear wave packet. The second term is a vector containing the first derivative of the electronic functions, referred to as the derivative coupling $\mathbf{d}_{IJ} = \langle \phi_I \mid \nabla_{\mathbf{R}} \mid \phi_J \rangle_{\mathbf{r}}$.[209] The third term is the scalar kinetic coupling, which is usually neglected $D_{IJ} = \langle \phi_I \mid \nabla_R^2 \phi_J \rangle_r \approx 0$.[209]

The electronic Hamiltonian does not depend on the nuclear coordinates and will only affect the electronic functions. Those are their eigenfunctions, so it is clear that

$$\left\langle \chi_i^I \phi_I \left| \hat{H}_{el} \right| \chi_j^J \phi_J \right\rangle_{r,R} = \epsilon_J S_{ij} \delta_{IJ} \tag{47}$$

where ϵ_J is the electronic eigenvalue. Applying those relations back into the TDSE, one can obtain the equation of motion for the coefficients in matrix notation

$$\dot{\mathbf{C}} = -iS^{-1}(T - \tau + V - i\dot{S}) \cdot \mathbf{C} \tag{48}$$

where

$$
\begin{aligned}
S_{ij} &= \langle \chi_i^I \mid \chi_j^J \rangle_{\mathbf{R}} \delta_{IJ} \\
\dot{S}_{ij} &= \langle \chi_i^I \mid \dot{\chi}_j^J \rangle_{\mathbf{R}} \delta_{IJ} \\
T_{ij} &= \langle \chi_i^I \mid \hat{T}_n \mid \chi_j^J \rangle_{\mathbf{r},\mathbf{R}} \delta_{IJ} \\
V_{ij} &= \left\langle \chi_i^I \phi_I \left| \hat{H}_{el} \right| \chi_j^J \phi_J \right\rangle_{\mathbf{r},\mathbf{R}} \\
\tau_{ij} &= \frac{1}{M} \langle \chi_i^I \mid \mathbf{d}_{IJ} \cdot \nabla_{\mathbf{R}} \mid \chi_j^J \rangle_{\mathbf{R}}
\end{aligned}
\tag{49}
$$

The analytical formula for the matrix elements is not derived here, but their final form is presented under the approximation of constant amplitudes ω_ρ. For the overlap matrix, we have

$$
\begin{aligned}
S_{ij} = \prod_{\rho}^{3N} \exp\left(\frac{-\omega_\rho (\bar{R}_{i\rho}^I - \bar{R}_{j\rho}^J)^2}{2} - \frac{(\bar{P}_{i\rho}^I - \bar{P}_{j\rho}^J)^2}{8\omega_\rho} \right) \times \\
\exp\left(i \left[\frac{\bar{R}_{i\rho}^I + \bar{R}_{j\rho}^J}{2} \left(\bar{P}_{j\rho}^J - \bar{P}_{i\rho}^I \right) + \bar{R}_{i\rho}^I \bar{P}_{i\rho}^I - \bar{R}_{j\rho}^J \bar{P}_{j\rho}^J \right] \right) \times \exp\left(i \left(\gamma_j - \gamma_i \right) \right) \delta_{IJ}
\end{aligned}
\tag{50}
$$

The atom width ω_ρ is defined at the beginning of the propagation and is kept the same, the centroid position for each Gaussian $\bar{\mathbf{R}}$ and the centroid momenta $\bar{\mathbf{P}}$ are obtained from the classical trajectories. In the subsequent matrix elements, the overlap can be reused, and only a multiplicative factor for each matrix element must be computed. For the time derivative overlap, we have

$$
\dot{S}_{ij} = \sum_{\rho}^{3N} \left[\left(\omega_\rho \left(\bar{R}_{i\rho}^I - \bar{R}_{j\rho}^J \right) - i \frac{\bar{P}_{i\rho}^I + \bar{P}_{j\rho}^J}{2} \right) \bar{v}_{j\rho} + \left(\frac{\bar{P}_{i\rho}^I - \bar{P}_{j\rho}^J}{4\omega_\rho} + i \frac{\bar{R}_{i\rho}^I - \bar{R}_{j\rho}^J}{2} \right) \bar{f}_{j\rho} + i\dot{\gamma}_j \right] S_{ij} \tag{51}
$$

As it involves the time derivative of the Gaussian j, it will also take as input the classical velocity $\bar{\mathbf{v}}$, force $\bar{\mathbf{f}}$ for this trajectory and the time derivative of the phase $\dot{\gamma}$, which is given in the main text. For the kinetic energy matrix, we have

$$
T_{ij} = \sum_{\rho}^{3N} \frac{1}{2M_\rho} \left[\left(\frac{\left(\bar{P}_{i\rho}^I + \bar{P}_{j\rho}^J \right)^2}{4} + \omega_\rho - \omega_\rho^2 \left(\bar{R}_{j\rho}^J - \bar{R}_{i\rho}^I \right)^2 \right) - i\omega_\rho \left(\bar{R}_{j\rho}^J - \bar{R}_{i\rho}^I \right) \left(\bar{P}_{i\rho}^I + \bar{P}_{j\rho}^J \right) \right] S_{ij} \tag{52}
$$

In the following matrices, the value of the potential energy and nonadiabatic coupling at the centroid position for each pair of Gaussians is required to compute the matrix elements.[118] Instead of the centroid value, the equations presented here use the BAT approximation,[104] discussed in the main text. The potential energy is

$$V_{ij} \approx \left[E_I(\mathbf{R}_i) + E_J(\mathbf{R}_j) + \sum_{\rho}^{3N} \left(\frac{\partial E_I(\bar{R}_{i\rho}^I)}{\partial R_\rho} + \frac{\partial E_J(\bar{R}_{j\rho}^J)}{\partial R_\rho} \right) \left(\frac{\bar{R}_{i\rho}^I + \bar{R}_{j\rho}^J}{2} + i \frac{\bar{P}_{j\rho}^J - \bar{P}_{i\rho}^I}{4\omega_\rho} \right) \right.$$
$$\left. - \bar{R}_{i\rho}^I \frac{\partial E_I(\bar{R}_{i\rho}^I)}{\partial R_\rho} - \bar{R}_{j\rho}^J \frac{\partial E_J(\bar{R}_{j\rho}^J)}{\partial R_\rho} \right] \frac{S_{ij}}{2}, \tag{53}$$

taking only the real value of the element V_{ij} . And finally, the nonadiabatic coupling terms, also using the BAT approximation

$$\tau_{ij} = \sum_{\rho}^{3N} \left[\frac{1}{2M_\rho} \left(d_{i\rho}^{IJ} + d_{j\rho}^{IJ} \right) \left(\omega_\rho \left(\bar{R}_{j\rho}^J - \bar{R}_{i\rho}^I \right) + i \frac{\bar{P}_{i\rho}^I + \bar{P}_{j\rho}^J}{2} \right) \right] S_{ij} \tag{54}$$

In this case, the overlap matrix element doesn't contain the δ_{IJ} term since it uses the overlap of trajectories in different electronic states.

B. BAT vs. SPA approximations

The bra-ket averaged Taylor expansion (BAT) approximation[104] has been developed to reduce the computational cost of electronic structure calculation during a multiple spawning simulation. This strategy allows QDCT to propagate the nuclear coefficients without the need for extra single-point calculations at the centroid points between trajectories. The quality of QDCT will then depend on the quality of the BAT approximation. In the systems used in this work, the population was computed for the same set of initial 500 conditions using the usual saddle-point approximation (SPA) approach, and the BAT and the populations were compared. It can be seen that in most cases, they agree well, except for the second Tully model, where there is more variation of the nonadiabatic coupling, and the population converges to a different value, although the difference is small.

In a higher-dimensional case, the population transfer will not be very influential far from the maximum coupling point. Due to the dimensionality, the overlap that controls the transfer falls very quickly away from the spawning point, and the BAT approximation is used mostly between similar trajectories. In Figure 31 we can see that the comparison between AIMS simulations in the 12-dimensional case is good in the limiting points, the beginning of the propagation, and after most of the transfer is completed. They return the same qualitative behavior and would agree on the estimated lifetime of the excited state, but there is a small deviation in the intermediary region.

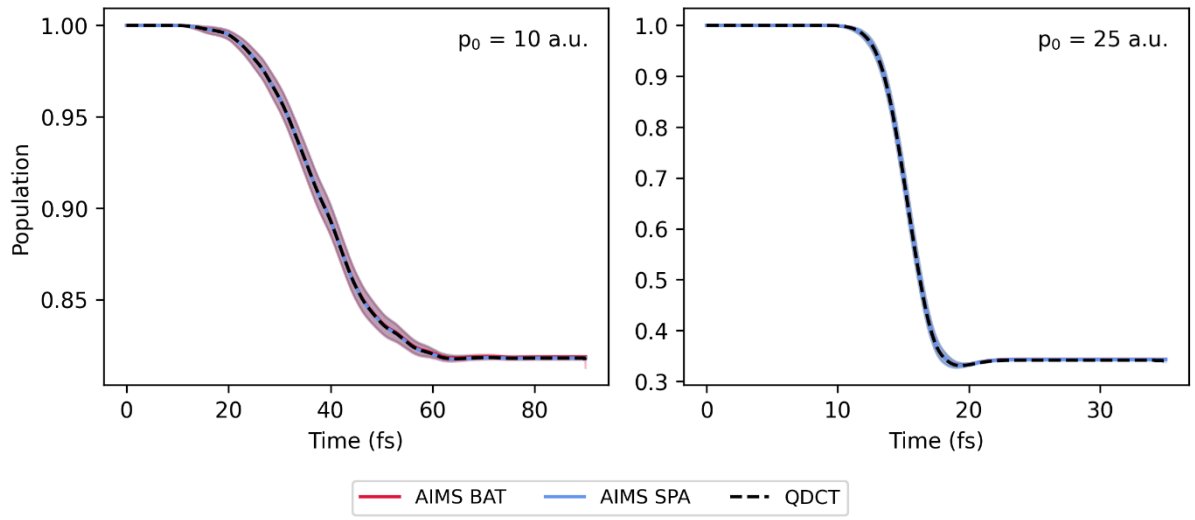

Figure 28 Lower state population for the simple avoided crossing Tully model. The initial condition was sampled around the momenta of 10 a.u. and 25 a.u. The shaded area in all curves represents a confidence interval of 95%.

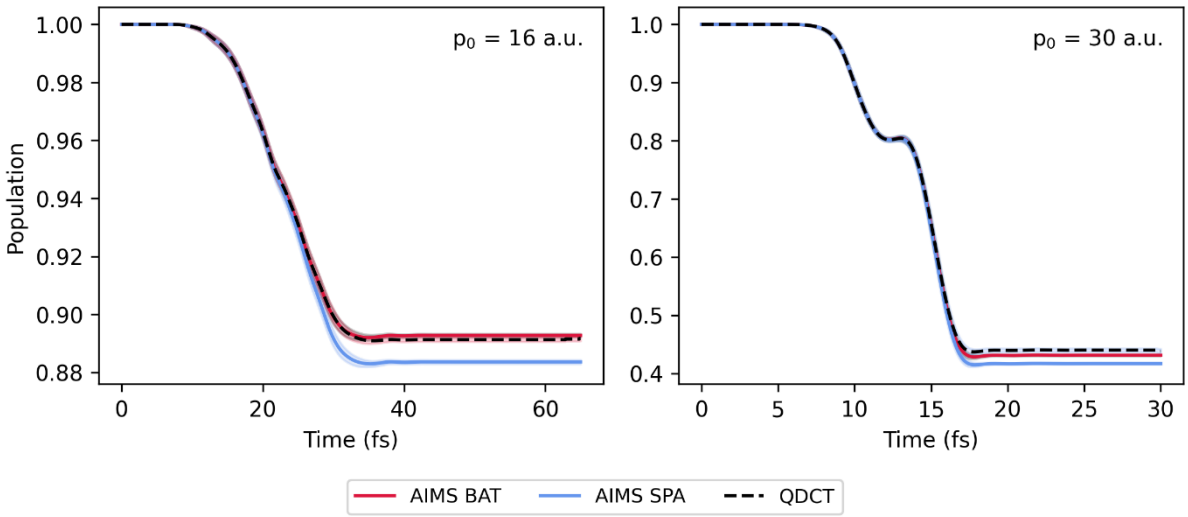

Figure 29 Lower state population for the dual avoided crossing Tully. The initial condition was sampled around the momenta of 16 a.u. and 30 a.u. The shaded area in all curves represents a confidence interval of 95%.

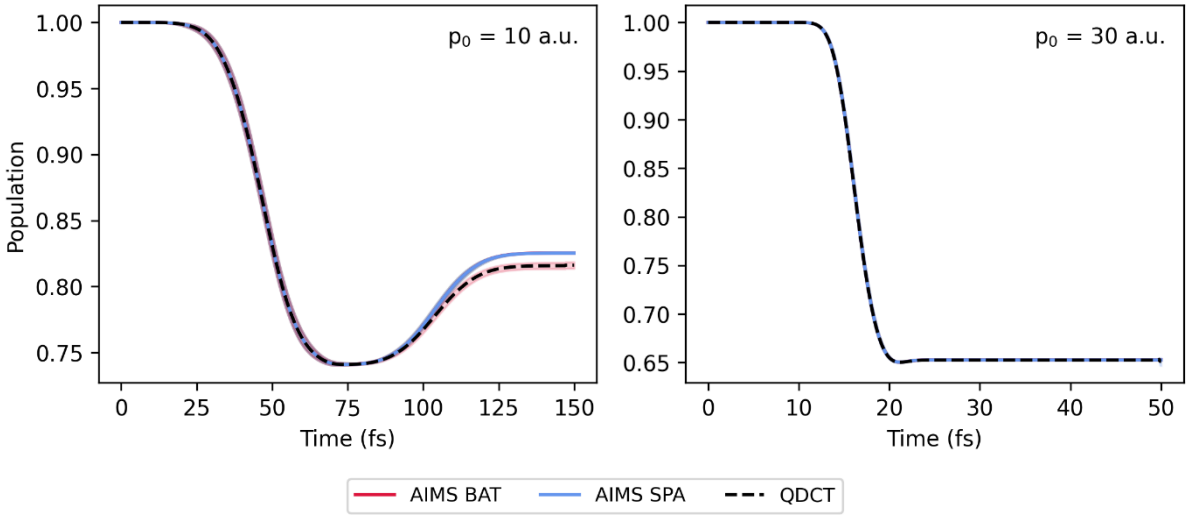

Figure 30 Lower state population for the simple avoided crossing Tully model. The initial condition was sampled around the momenta of 10 a.u. and 30 a.u. The shaded area in all curves represents a confidence interval of 95%.

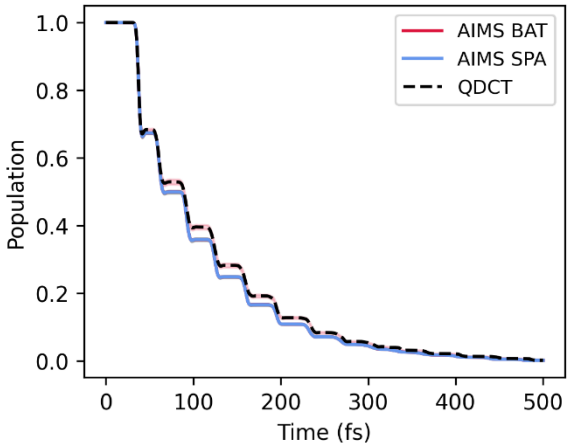

Figure 31 Upper state population for the SBH model using 500 trajectories. The shaded area in all curves represents a confidence interval of 95%.

C. Analytical Models

The Tully models used to test the QDCT method are the same as initially presented in Tully's paper.[91]

a. Tully 1: Simple avoided crossing

In the simple avoided crossing, the electronic energies are symmetric, and the off-diagonal elements are the same, as given in

$$\begin{aligned} V_{AA}(x) &= \begin{Bmatrix} A(1-\exp(-Bx)), x>0 \\ -A(1-\exp(Bx)), x<0 \end{Bmatrix} \\ V_{BB}(x) &= -V_{AA} \\ V_{AB}(x) &= V_{BA}(x) = C\exp(-Dx^2) \end{aligned} \tag{55}$$

The parameters used are:

$$\begin{aligned} A &= 0.01 \\ B &= 1.6 \\ C &= 0.005 \\ D &= 1.0 \end{aligned} \tag{56}$$

b. Tully 2: Dual avoided crossing

In this model, the potential energies are two wells, one over the other, with the minimum at the $x = 0$.

$$\begin{aligned} V_{AA}(x) &= 0 \\ V_{BB}(x) &= -A\exp(-Bx^2) + E_0 \\ V_{AB}(x) &= V_{BA}(x) = C\exp(-Dx^2) \end{aligned} \tag{57}$$

For this model, the parameters are:

$$\begin{aligned} A &= 0.1 \\ B &= 0.28 \\ C &= 0.015 \\ D &= 0.06 \\ E_0 &= 0.05 \end{aligned} \tag{58}$$

c. Tully 3: Extended coupling with reflection

For the extended coupling model, the energies start degenerated and are split later.

$$V_{AA}(x) = A$$
$$V_{BB}(x) = -A \quad (59)$$
$$V_{AB}(x) = V_{BA}(x) = \begin{Bmatrix} B\exp(Cx), x < 0 \\ B(2 - \exp(-Cx), x > 0 \end{Bmatrix}$$

With the parameters:

$$A = 6E - 4$$
$$B = 0.1 \quad (60)$$
$$C = 0.9$$

d.Spin-Boson Hamiltonian

The Spin-Boson Hamiltonian[148–151] is a two-level system (H_S) with a harmonic bath (H_B), and they are linearly coupled (H_{SB}). The system's dimensionality is defined by the number of oscillators in the bath (N), and each of them is defined by their masses (M_ρ) and frequencies (ω_ρ). The diabatic Hamiltonian for this model can be computed with the following equations

$$H = H_S + H_B + H_{SB}$$
$$H_S = \sigma_z \epsilon_0 - \sigma_x \nu_0$$
$$H_B = I_2 \frac{1}{2} \sum_{\rho=1}^{N} \frac{P_\rho^2}{M_\rho} + M_\rho \omega_\rho^2 R_\rho^2 \quad (61)$$
$$H_{SB} = \sigma_z \sum_{\rho=1}^{N} g_\rho R_\rho$$

where R_ρ and P_ρ are the system's positions and momenta. The energy bias (ϵ_0) and the electronic inter-state coupling (ν_0) can be tuned for the system. σ_z and σ_x are the Pauli matrices and I_2 is the identity matrix of size 2.

The coupling constants (g_ρ) between the system and bath are determined by the spectral density

$$J(\omega) = \frac{\pi}{2} \sum_{\rho=1}^{N} \frac{g_\rho^2}{M_\rho \omega_\rho} \delta(\omega - \omega_\rho) \quad (62)$$

Here, we have used the Debye spectral density with the reorganization energy E_R and characteristic frequency ω_c

$$J_D(\omega) = \frac{E_R}{2} \frac{\omega \omega_c}{\omega^2 + \omega_c^2} \quad (63)$$

The coupling coefficient and vibrational frequency for each oscillator in the bath can be computed following

$$\omega_\rho = \tan\left(\frac{\rho}{N}\tan^{-1}\left(\frac{\omega_{max}}{\omega_c}\right)\right)\omega_c$$
$$g_\rho = \left[\frac{M_\rho E_R}{\pi N}\tan^{-1}\left(\frac{\omega_{max}}{\omega_c}\right)\right]^{1/2}\omega_\rho \quad (64)$$

In the adiabatic representation, for both the FSSH and AIMS calculations, the energies can be computed as

$$E_i = \frac{1}{2}\sum_{\rho=1}^{N} M_\rho \omega_\rho^2 R_\rho^2 + (-1)^i\left(\eta^2 + \nu_0^2\right)^{1/2}$$
$$\eta = \left(\sum_{\rho=1}^{N} g_\rho R_\rho + \epsilon_0\right) \quad (65)$$

The energy gradients are given by

$$\frac{\partial E_i}{\partial R_k} = M_k\omega_k^2 R_k^2 + (-1)^i g_k\left(\frac{\eta}{\left[\eta^2+\nu_0^2\right]^{1/2}}\right) \quad (66)$$

And the nonadiabatic couplings are

$$d_{01}^k = -d_{10}^k = -\frac{1}{2}g_k\left(\frac{\nu_0}{\left[\eta^2+\nu_0^2\right]}\right) \quad (67)$$

For those systems, the characteristic frequency (ω_c) is obtained from the max frequency (ω_{max}):

$$\omega_c = \frac{\omega_{max}}{3} \quad (68)$$

The parameters used for all SBH in this paper are as follows, changing only N that gives the dimensionality of the system.

$M_\rho = 1822.888515 m_e$
$\epsilon_0 = 0.006 au$
$\nu_0 = 0.005 au$
$\omega_{max} = 400 cm^{-1}$
$E_R = 0.2$

D. Confidence Interval Study

In the main text, we saw that across all the models, the average population of surface hopping showed a broader confidence interval when the decoherence correction was applied. We chose to use the first Tully model with high momentum, where the average population of both FSSH simulations was similar (Figure 32), to compare the confidence intervals.

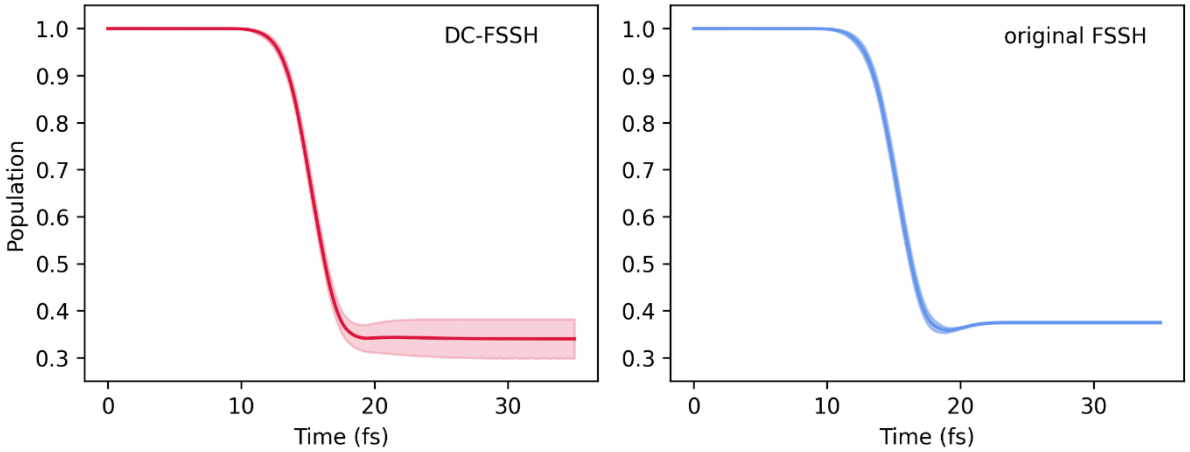

Figure 32 Simple avoided crossing model from Tully, starting with 25 a.u. as initial momentum. Computed with decoherence corrected FSSH (left) and original FSSH (right).

The decoherence correction applied in this work was presented by Granucci and Persico[98] and modifies the coefficient by assuming an exponential decay of the population of the states not filled following the equations

$$C'_J = C_J \exp(-\Delta t / \tau), \qquad \forall\ J \neq I$$

$$C'_I = C_I \left[\frac{1 - \sum_{J \neq I} |C'_J|^2}{|C_I|^2} \right]^{1/2} \tag{69}$$

The coefficients C follow the current electronic state of the trajectory (I) or all others (J). Δt is the size of the timestep used in the propagation. In this case, the decoherence time is computed based on the relation between the potential energy difference (ΔE) and the kinetic energy (K) of the system:

$$\tau = \frac{\hbar}{|\Delta E|}\left(1 + \frac{\alpha}{K}\right) \tag{70}$$

With only α as a free parameter, that is usually set to 0.1 E_h.[98,112] The application of the decoherence correction in the coefficients tempers with the propagation stipulated by the Schrödinger equation and forces the population to tend to the current electronic state of the trajectory, as can be seen by the individual populations of each trajectory in Figure 33. It comes

naturally then that computing an intermediate value for the population (say 0.4) from an average of zeros and ones will lead to a larger confidence interval.

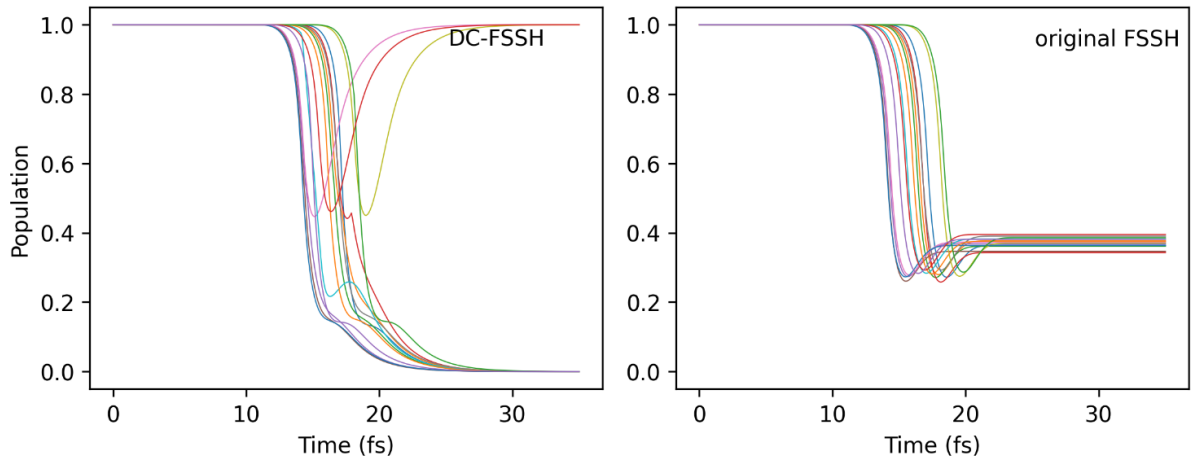

Figure 33 Single trajectory electronic population of the first 15 trajectories for Tully 1 with initial momentum 25 a.u.

If we vary this free parameter so that the time τ increases, we can gradually approach the behavior of FSSH without correction, as shown in Figure 34. Here, we compare the maximum error along the simulation, meaning the largest width of the confidence interval found in the simulation, and the last error as we increase α. The error is defined as the difference between the highest point in the confidence interval and the smallest one.

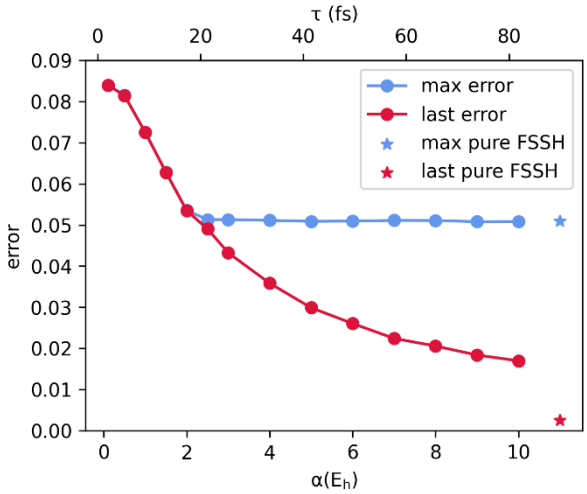

Figure 34 Largest confidence interval width and last width of a varying value of the parameter α in Hartree and the corresponding times τ in fs. The stars denote the similar values for the simulation without decoherence correction.

The maximum error reaches a plateau at $\alpha = 2.5$. This is also present in the FSSH without decoherence after the large population transfer, at about 17 fs (Figure 32). After this time, in the original FSSH, the confidence interval decreased, and the error was almost zero at the end of the simulation. We can see from Figure 34 that this is also the trend in DC-FSSH as α

increases. As the value of α is increased, the coefficient decays slower towards the binary values, and the split between populations is reduced (Figure 35), leading to a smaller confidence interval.

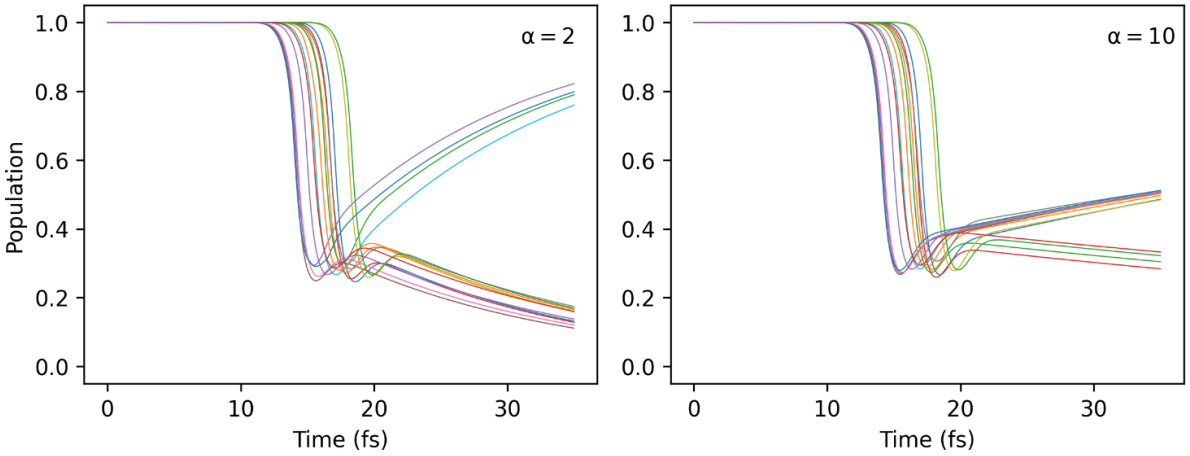

Figure 35 Single trajectory electronic population of the first 15 trajectories for Tully 1 with initial momentum 25 a.u as the free parameter alpha is increased.

E. Overlap vs. Dimensionality

It is common knowledge within multiple spawning that with increased dimensionality, the eventual overlap between pairs of trajectories becomes exceedingly rare. This expectation is the foundation for multiple approximations: independent first-generation, [60,122] stochastic selection,[119] and bracket-Taylor approximation. [104] Here, we give an example of how this overlap decreases as the system's dimension is systematically increased.

In Figure 36, we show the maximum overlap for each pair of trajectories for the dimensions from 1 to 12. Each matrix element S_{ij} contains the maximum overlap between trajectories i and j along all timesteps of the simulation. The diagonal terms contain the overlap with a trajectory with itself, so it is always unity. In the unidimensional case, there is a high amount of trajectories with a reasonable overlap that can be used for trajectory substitution in QDCT. As the dimensionality increases, the overlap falls quite fast. At $N = 3$, there are fewer overlaps, which would make it difficult to make a simple substitution at the trajectory spawning. For larger dimensions, it is evident that without the help of interpolated trajectories, the QDCT strategy would not be viable. In Figure 37, the maximum overlap at each different SBH dimension is shown. This exemplifies that in a real system, one can consider that the trajectories are non-interacting unless they are created explicitly with this purpose.

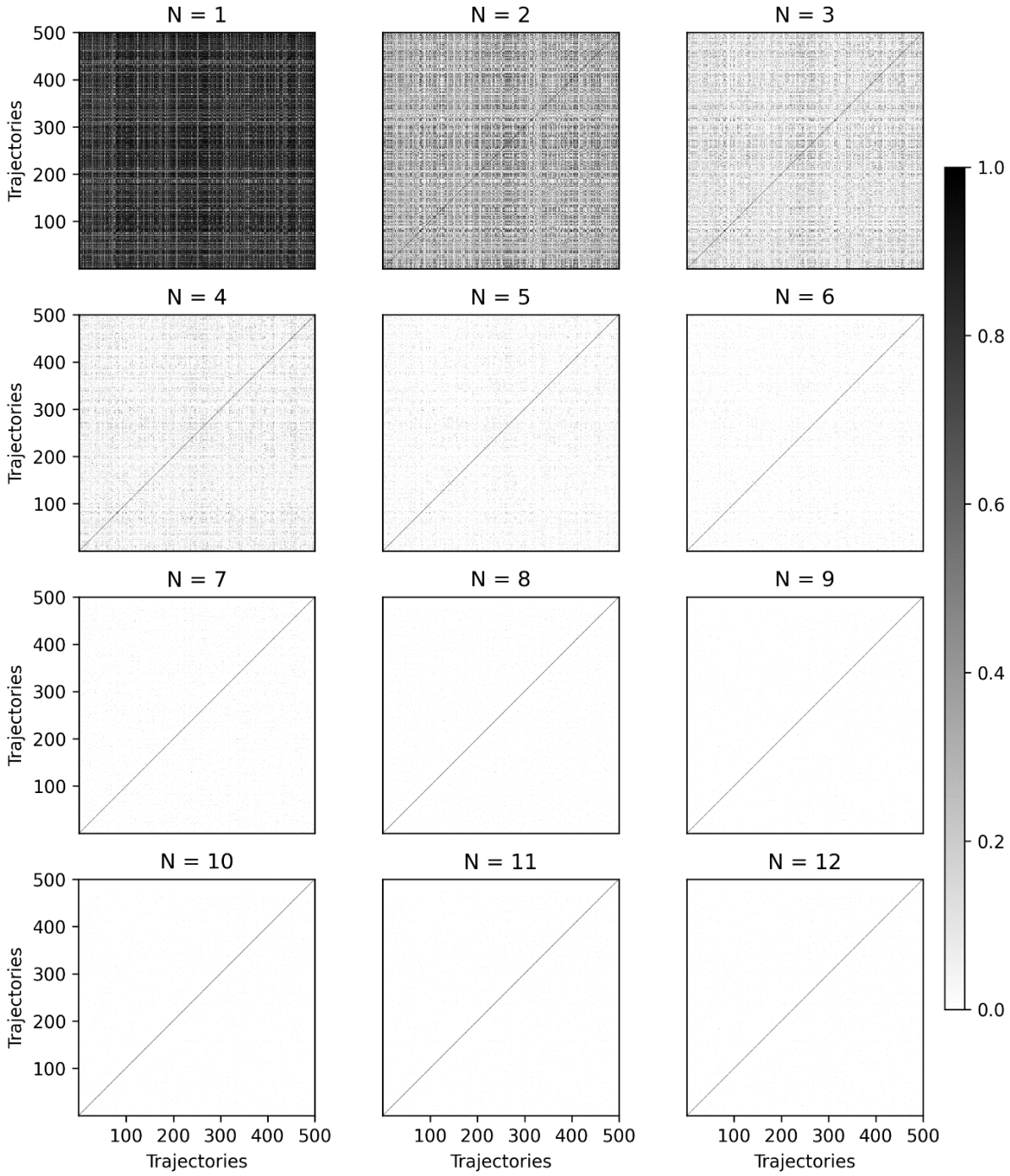

Figure 36 For each overlap matrix, the elements S_{ij} contain the maximum absolute overlap between trajectories i and j for all timesteps of the SBH model in different dimensions.

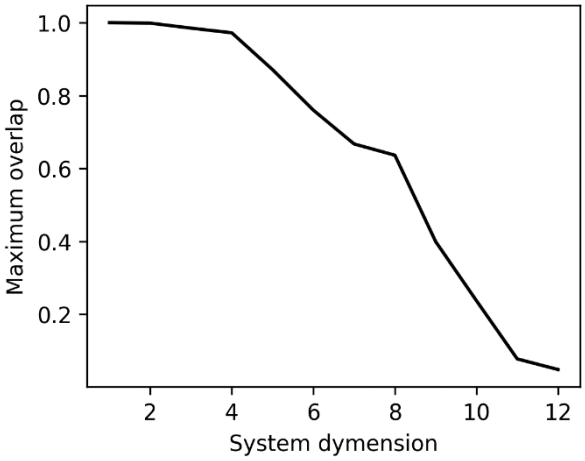

Figure 37 Maximum overlap between all the pairs of trajectories for all timesteps with increasing system dimensionality. This doesn’t consider the overlap of a trajectory with itself.